UNIVERSITEIT VAN PRETORIA
UNIVERSITY OF PRETORIA
YUNIBESITHI YA PRETORIA

The characterization of bulk as-grown and annealed ZnO by the Hall effect

GÜNTHER HORST KASSIER

Submitted in partial fulfillment of the requirements for the degree

MAGISTER SCIENTIAE

In the Faculty of Natural & Agricultural Science
University of Pretoria
Pretoria

Supervisor: Professor M. Hayes
Co-Supervisor: Professor F.D. Auret

October 2006

UNIVERSITEIT VAN PRETORIA
UNIVERSITY OF PRETORIA
YUNIBESITHI YA PRETORIA

The characterization of bulk as-grown and annealed ZnO by the Hall effect

By Günther Horst Kassier

Supervisor: Prof. M. Hayes
Co-Supervisor: Prof. F.D. Auret

SUMMARY

A fully automated Temperature Dependent Hall (TDH) measurement setup has been assembled for the purposes of this study. This TDH setup is capable of measuring samples in the 20 K to 370 K temperature range. Sample sizes of up to 20 mm × 20 mm can be accommodated by the custom designed and manufactured sample holder. Samples with a resistance in the 1 Ω to 250 MΩ range can be measured with this setup provided that the mobility of the sample is greater than 1 cm^2/Vs. The computer program controlling the automated measurement process was written in LabView^{TM} version 6.1.

Single crystal Zinc Oxide (ZnO) was the material under investigation in this study. Bulk ZnO samples grown by three different methods, namely pressurized melt growth, seeded chemical vapor transport (SCVT) growth and hydrothermal growth, were measured in the 20 K to 370 K range. The effect of annealing in argon atmosphere in the 550 ºC to 930 ºC range was investigated on all three ZnO types. In addition, hydrogen-implanted layers on semi-insulating hydrothermally grown ZnO were studied. These samples were annealed in the 200 ºC to 400 ºC range and Hall measurements in the 20 K to 330 K range were performed.

Programs were written to fit, wherever possible, the obtained temperature dependent carrier concentration and mobility profiles to suitable theoretical models. The carrier concentration data was fitted to a multi-donor single acceptor charge balance equation for the purpose of extracting donor concentrations and activation energies. Before fitting, the data was corrected for the Hall scattering factor and, where necessary, for two-layer effects particularly a degenerate surface

conduction channel that developed through annealing on the SCVT-grown and hydrothermally grown samples. The acceptor concentrations of the samples were obtained by fitting the mobility data to a model based on D.L. Rode’s method of solving the Boltzmann transport equation. Scattering mechanisms included in the model were piezoelectric and deformation potential acoustic modes, polar optic modes and ionized impurity scattering.

It was found that the mobility data did not fit the model very well without assigning questionable values to other parameters, in this case the deformation potential. Plausible values for the acceptor concentration were however obtained. The carrier concentration data fitted the model well, but due to the large number of parameters to be extracted (up to six parameters in the case of three donors) there was often not much certainty in the extracted values.

This study shows that TDH analysis is a valuable tool to assess the quality of semiconductors. Bulk and degenerate surface (or interfacial) conduction are separated with relative ease, and shallow defect concentrations as well as compensation level concentrations could be extracted. The generally observed uncertainty in values obtained in the multi-parameter regression of carrier concentration data indicates that supplementary techniques such as photoluminescence are needed to support results obtained by the TDH technique.

ACKNOWLEDGEMENTS

I would like to thank the following people:

- My supervisor Prof. M. Hayes for his input concerning corrections and layout of this thesis.

- My co-supervisor Prof. F.D. Auret for his help and support in both financial and academic matters. I am particularly grateful for useful discussions and his willingness to support any research project I chose to undertake.

- Walter Meyer for the countless times I received help from him. I would in particular like to thank him for writing a large part of the Hall automation program, thus helping me to get my own programming efforts started.

- The machinists Gerhard Pretorius and Juan Taljaard for their support in all things technical, particularly the machining of the Hall sample holder by Gerhard.

- Hannes de Meyer for his help in designing the Hall sample holder and the making of some of the sketches in this thesis.

- The electronics technician Roelf van Weele for all the help I received from him during the course of this study.

- Dr. Jackie Nel for providing me with an ample supply of ZnO samples.

- My fellow postgraduate students for all their help and support

- The National Research Foundation (NRF) for financial assistance.

- The Carl and Emily Fuchs Institute for Microelectronics (CEFIM) for financial assistance.

- My parents Horst and Marianne Kassier for all their love and support

INDEX

CHAPTER 1

INTRODUCTION

One of the most important properties of a semiconductor material is the nature of its defects. In the great majority of semiconductor applications, the electrical and optical properties of defects are of particular importance. Shallow electrical defects have a strong and direct effect on the carrier concentration while deeper defects can indirectly affect the carrier concentration by acting as charge trapping centres. Defects also enter into the electrical transport properties of a semiconductor through lattice and impurity related scattering mechanisms, thereby having a significant impact on the mobility of carriers in the material. Hall effect measurements are a powerful technique to separate the conduction of a material into carrier concentration and carrier mobility contributions. If in addition the temperature dependence of the carrier concentration is studied, further separation into various donor and acceptor contributions is possible. In particular, one can extract donor (or acceptor) concentrations and activation energies. Similarly, the temperature dependent mobility can be separated into lattice and impurity contributions. If lattice scattering can be quantified through material parameters known from independent measurements, ionized and neutral impurity concentrations may be extracted by fitting Hall mobility data to a scattering model that takes into account the relevant scattering mechanisms. Therefore temperature dependent Hall (TDH) analysis is an excellent technique for determining not only the shallow defect spectrum of a material but also neutral and compensating impurity concentrations.

The analysis possibilities mentioned above are in general only applicable to non-degenerate high quality single crystal semiconductors. New and refined bulk and epitaxial crystal growth methods have fuelled research not only on novel materials but also on a number of semiconductors that have been known for decades. One example of such a material is zinc oxide (ZnO), and this study is devoted to the temperature dependent Hall effect characterization of bulk ZnO. Shallow defects in ZnO have been studied since the 1950's, but the physical origin of the various donors has not yet been established in a satisfactory way. What is known is that bulk weakly compensated material appears to have a main donor with activation energy close to the hydrogenic value of 66 meV in ZnO. In addition, a donor in the 30 meV to 50 meV range is present in some as-grown material. Hydrogen doping experiments in ZnO have yielded donors in this activation energy range, establishing hydrogen as a likely shallow donor candidate also in as-grown ZnO. The results of the present study also link hydrogen to a shallow donor in the expected range, and annealing experiments in this study indicate that hydrogen is present in as-grown bulk ZnO in various concentrations and that out-diffusion of hydrogen takes place at temperatures above 500 ºC. Another interesting aspect of bulk ZnO is the formation of a highly conductive n^+-channel at the surface, and such conductive channels are discussed in chapter 7. TDH analysis allows for separation of non-degenerate and degenerate conduction in a sample, and a two-layer model is derived and used in analysing samples with surface conduction. Contrary to what was found in some reports, the surface conduction observed in this study appears to be stable with respect to both high temperature annealing and the influence of ambient gases, in particular oxygen.

The present dissertation describes and demonstrates the TDH technique using bulk single crystal ZnO as an example. The theory required for the calculation of mobility and carrier concentration from Hall effect measurements is described in chapter 2. In addition, Hall profiling theory is discussed with emphasis on the two-layer model, a technique for separating degenerate and non-degenerate conduction in a sample. Chapter 3 is concerned with providing a theoretical framework for modelling both carrier concentration and mobility in non-degenerate semiconductors. The carrier concentration model described in this chapter is limited to relatively weakly compensated semiconductors with multiple shallow donors. The mobility will be described by a low field transport model using D.L. Rode’s method of solving the Boltzmann transport equation without approximation.

Chapter 4 offers a brief description of ZnO. Some information on physical properties and band structure of ZnO is given, but the main focus of this chapter is the discussion of various shallow donors and acceptors that have been found or are expected to occur in this material. The citations in this chapter include both theoretical and experimental work on shallow defects in ZnO. Hydrogen in ZnO forms an important part of this discussion.

The details of the TDH measurement setup designed and constructed for this study are discussed in chapter 5. Various practical aspects of measurement as well as specifications and limitations of the setup are discussed.

The discussions of chapters 2 through 5 come together in chapters 6 where the implementation of both Temperature dependent Hall measurement and data analysis based on theoretical models is described. The results of the measurement and analysis as applied to different types of as-grown, annealed and implanted bulk ZnO are presented and discussed in chapter 7. Chapter 8 gives a brief review of the findings presented in chapter 7. In addition, conclusions are drawn from the results of this study and further research possibilities are identified.

CHAPTER 2

THE HALL EFFECT AS APPLIED TO SEMICONDUCTOR CHARACTERIZATION

When a conductor is placed in a magnetic field and a current passed through it an electric field will be produced, the direction of which is normal to both the current and magnetic field directions. This phenomenon, discovered by E.T. Hall in 1879, is known as the Hall effect **[1]**. In this chapter, it will be shown how the Hall effect may be used in the characterization of semiconductors. In particular, it is possible to determine carrier type, carrier concentration and carrier mobility by obtaining appropriate voltage and current readings on a sample that is placed in the Hall setup. Without any other information about the sample, the accuracy of this technique is typically better than 20% **[2]**.

2.1 HALL THEORY

Current flow in materials is a statistical effect that occurs when charge carriers drift through a material with an average velocity **v** **[1]**. Since these carriers are charged particles, they experience a Lorentz force when the conductor is placed in a magnetic field. This force is given by **[3]**

$$\mathbf{F}_{\mathrm{L}} = q\,(\mathbf{v} \times \mathbf{B}) \qquad (2.1)$$

where **B** is the applied magnetic field, q the charge of the carriers and **v** the drift velocity of the carriers. It should be noted that q is taken as positive for holes and negative in the case of electrons.

Consider now a conductive material placed in a magnetic field, as shown in figure 2.1 **[4]**. The directions of carrier flow and deflection due to the magnetic field are illustrated for both positively and negatively charged carriers. This Lorentz force-induced deflection leads to a charge imbalance along the y-direction of the sample, thus resulting in an electric field E_y.

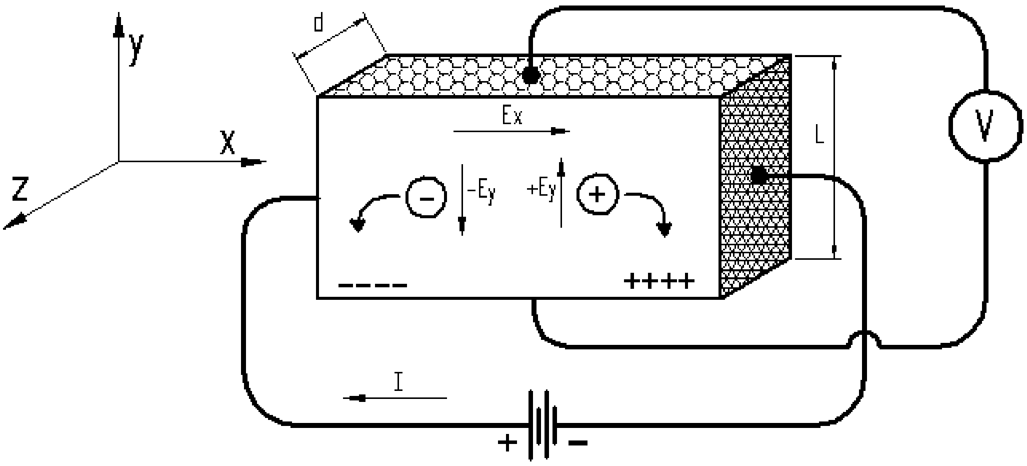

Figure 2.1 Diagram illustrating the Hall effect. The current flows in the x-direction, the Hall field points along the y-direction and the magnetic field in the z-direction (out of the page) [4].

In the steady state, the force due to the electric field $F_E = qE_y$ will balance the Lorentz force F_L acting on the carriers, i.e. $F_L = -F_E$. Therefore one can write

$$q\mathbf{E_y} = -q(\mathbf{v_x} \times \mathbf{B}_z) \tag{2.2}$$

Upon calculating the cross product in equation 2.2, taking into account that $\mathbf{v_x}$, $\mathbf{E_y}$ and $\mathbf{B_z}$ point in the *x*-, *y*-, and *z*-directions respectively, one obtains

$$E_y = v_x B_z \tag{2.3}$$

where v_x, E_y and B_z are the absolute values of $\mathbf{v_x}$, $\mathbf{E_y}$ and $\mathbf{B_z}$ respectively. One can now write v_x in terms of the current density J_x and carrier concentration n:

$$v_x = \frac{J_x}{nq} \tag{2.4}$$

The carrier concentration is by definition a positive quantity and the information about carrier type is contained in q. Combining equations 2.3 and 2.4, the following is obtained:

$$E_y = \frac{J_x B_z}{nq} \tag{2.5}$$

The Hall coefficient R_H is now defined by

$$E_y = R_H J_x B_z \tag{2.6}$$

When one compares equations 2.5 and 2.6, it becomes apparent that

$$R_H = \frac{1}{nq} \tag{2.7}$$

This implies that the sign of R_H is determined by the charge of the dominant carrier type, i.e. it is positive for holes and negative in the case of electrons.

It should be noted that in the derivation of equation 2.5 we neglected any scattering effects that occur in a real sample. Scattering has a randomizing effect on the velocity distribution of the carriers, thus violating the assumption in the derivation of equation 2.7 that all carriers travel with the same velocity **v** [2, 5, 6]. Consequently, equation 2.7 is merely an approximate relationship between the Hall coefficient and the carrier concentration. The degree of accuracy of the approximation depends on factors such as the carrier type, scattering mechanisms and band structure of the material, the strength of the applied magnetic field and temperature. The following equation gives a more exact relationship between the carrier concentration and the Hall coefficient [1, 6]**:**

$$R_H = \frac{r_H}{nq} \tag{2.9}$$

Here, r_H is a dimensionless quantity called the Hall scattering factor. Usually r_H assumes values between 1 and 2 [5]. As the magnetic field increases, the Lorentz force on each carrier will increase and will, at some stage, dominate over the forces on carriers due to the scattering mechanisms in the crystal. As the magnetic field approaches infinity, one would thus expect r_H to converge to unity [1, 6]. In practice, the magnetic field is not so strong that the scattering factor becomes negligible. In fact, r_H has to be measured or calculated for the most accurate results [1]. A more detailed discussion of the Hall scattering factor is given in section 3.2.2, and formulae to calculate r_H will be given.

2.2 CALCULATION OF THE HALL COEFFICIENT

Consider again the sample placed in a magnetic field, as depicted in figure 2.1. Suppose that one measures a current I_x passing through the sample. Since the cross sectional area of the sample on the plane perpendicular to the current direction is given by $A = Ld$, the current density J_x in the sample can be calculated as follows:

$$J_x = \frac{I_x}{Ld} \tag{2.10}$$

One can also write the electric field E_y in terms of the measured Hall voltage and the width of the sample in the y-direction:

$$E_y = \frac{V_H}{L} \tag{2.11}$$

Substitution of equations 2.10 and 2.11 into equation 2.6 yields [1]

$$R_H = \frac{V_H d}{I_x B_z} \tag{2.12}$$

To obtain the correct sign of R_H, one should take I_x as positive if there is an electron current from left to right. Similarly, V_H is positive when a positive potential is measured at the bottom of the sample (refer to figure 2.1).

2.3 PRACTICAL DETERMINATION OF THE HALL COEFFICIENT, CARRIER CONCENTRATION, RESISTIVITY AND MOBILITY

2.3.1 Van Der Pauw Measurements to Determine Resistivity and Carrier Concentration

Equation 1.12 informs us that the Hall coefficient is independent of the width and length of the sample. In fact, as long as the sample is flat, isotropic, homogeneous, of uniform thickness and a singly connected domain (i.e. no holes), the sample can have any shape (see figure 2.2). Van der Pauw proved this result in 1958 when he solved the potential problem for a thin layer of arbitrary shape with four point-like contacts along the periphery **[7]**. The same conditions apply for the determination of resistivity. The requirement of point-like contacts (small contacts relative to the sample dimensions) is critical, but usually not easy to realize. A good “rule of thumb” to adhere to is not to let the contact size exceed 10% of the size of the smallest sample dimension **[1]**.

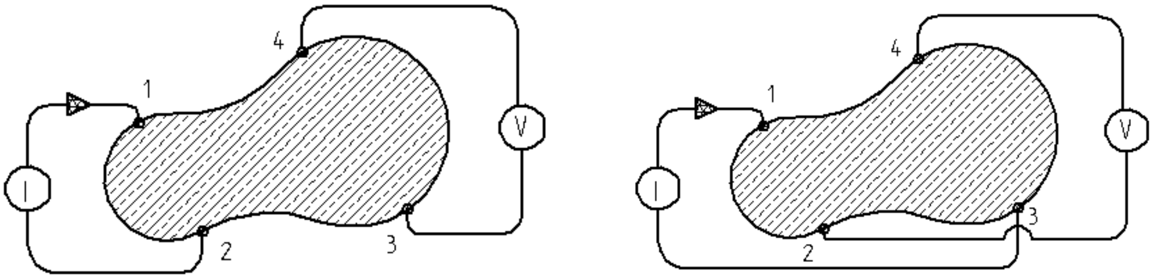

a) b)

Figure 2.2 Contact configuration for a) resistivity measurement and b) Hall measurement. The pictures also illustrate that the sample can have any shape **[1]**.

To see how the Hall coefficient is measured, consider figure 2.2 b). From equation 2.12 it can be seen that R_H is proportional to the quotient V_H/I_x, which has dimensions of resistance. Defining the resistances $R_{ij,kl} \equiv V_{kl}/I_{ij}$ with $V_{kl} = V_k - V_l$ the potential difference between contacts k and l and I_{ij} the current from contact i to contact j, the Hall coefficient is given by the following expression **[1, 5]**:

$$R_H = \frac{d}{B}\left(\frac{R_{31,42} + R_{42,13}}{2}\right) \tag{2.13}$$

By averaging over the two "Hall"-configurations, errors caused by misalignment of the four contacts are eliminated. There are, however, a number of thermomagnetic effects that could falsify measurements if not taken into account. These are the Ettingshausen effect, the Righi-Leduc effect and the Nernst effect [5]. All three effects produce a thermoelectric voltage caused by temperature gradients in the sample. In the case of the Nernst effect, the temperature gradient is caused by magnetic field independent factors such as uneven sample heating (cooling) or the Peltier effect. In the other two effects, the temperature gradient is set up by the different Lorentz-deflection of carriers that have different velocities. Let $R_{ij,kl}^{+}$ denote a Hall resistance measured in a magnetic field pointing in the $(+z)$-direction and $R_{ij,kl}^{-}$ the corresponding resistance with B in the $(-z)$-direction. It can be shown that all effects except the Ettingshausen effect can be eliminated by the following average over current and magnetic field directions [1, 8]:

$$R_H = \left(\frac{d}{8B}\right)\left[R_{31,42}^{+} - R_{13,42}^{+} + R_{42,13}^{+} - R_{24,13}^{+} + R_{13,42}^{-} - R_{31,42}^{-} + R_{24,13}^{-} - R_{42,13}^{-}\right] \tag{2.14}$$

Once the Hall coefficient is known, the carrier concentration n can be calculated through equation 2.9 where r_H is often simply equated to unity. In the case of metals or degenerate semiconductors, this assumption is indeed true [2].

By definition, resistivity ρ is the proportionality constant relating the electric field **E** in a conductor to the current density **J** in the conductor such that $\mathbf{E}=\rho\mathbf{J}$ [3]. The reciprocal of resistivity is called conductivity σ, and thus $\sigma = 1/\rho$. According to van der Pauw's analysis, the resistivity of a sample can be determined via the following formula (see figure 2.2 a)):

$$\rho = \frac{\pi d}{\ln(2)}\left(\frac{R_{21,34} + R_{32,41}}{2}\right) f \tag{2.15}$$

where f is a correction factor depending on the ratio $Q = R_{21,34}/R_{32,41}$. f is determined from the transcendental equation [1, 5]

$$\frac{Q-1}{Q+1}=\frac{f}{\ln(2)}\operatorname{arccos}h\left[\frac{1}{2}\exp\left(\frac{\ln(2)}{f}\right)\right] \tag{2.16}$$

which has to be solved numerically. Analytic approximations to the solution do, however, exist. It is readily seen that as Q approaches unity, so does f. It should be stressed that f is a purely geometric correction factor that has nothing to do with possible resistivity anisotropies in the sample. If such anisotropies exist, the resistivity would in any case become a tensor rather than a scalar quantity. As in the case of Hall measurements it is possible to minimize thermoelectric effects by averaging over all the different contact permutations and current directions **[1]**:

$$\rho=\frac{\pi d}{\ln(2)}\left[\frac{(R_{21,34}-R_{12,34}+R_{32,41}-R_{23,41})f_A}{8}+\frac{(R_{43,12}-R_{34,12}+R_{14,23}-R_{41,23})f_B}{8}\right] \tag{2.17}$$

Here, f_A and f_B are determined from Q_A and Q_B respectively, which in turn are given by

$$Q_A=\frac{R_{21,34}-R_{12,34}}{R_{32,41}-R_{23,41}} \tag{2.18}$$

$$Q_B=\frac{R_{43,12}-R_{34,12}}{R_{14,23}-R_{41,23}} \tag{2.19}$$

2.3.2 Mobility

The drift mobility μ_d is defined as the proportionality constant between the applied electric field on a conductor and the velocity of the carrier as a result of the field **[4, 5]**:

$$\mathbf{v}=\mu_d\mathbf{E} \tag{2.20}$$

Combining equation 2.4 with the definition of conductivity, the following result is obtained:

$$\sigma=\frac{nqv}{E} \tag{2.21}$$

But equation 2.20 informs us that this is equivalent to

$$\sigma = nq\mu_d \tag{2.22}$$

which implies that $[1/(nq)]\sigma = \mu$ and thus $[r_H/(nq)]\sigma = r_H\mu_d$, which yields, by equation 2.9,

$$R_H\sigma = r_H\mu_d \tag{2.23}$$

The Hall mobility μ_H is now defined by **[1]**

$$\mu_H = r_H\mu_d \tag{2.24}$$

If one now combines equations 2.23 and 2.24, one obtains an expression for the Hall mobility in terms of the Hall coefficient and the conductivity of the sample:

$$\mu_H = |R_H|\sigma \tag{2.25}$$

The absolute value of the Hall coefficient is used because mobility is by convention a positive quantity. It should be noted that if the Hall scattering factor is close to unity, the Hall mobility will be approximately equal to the drift mobility.

2.3.3 Practical Sample Shapes

In practical Hall and resistivity measurements, there are a number of different sample shapes in use, all of which have their own advantages and disadvantages (two examples are shown in figure 2.3) **[1, 9]**. In the present study, measurements were done exclusively on square samples with contacts placed at the four corners, as shown in figure 2.3. Although not the optimal choice as far as minimizing errors is concerned, samples of this geometry are generally much easier to make, particularly if more advanced sample processing facilities are not available.

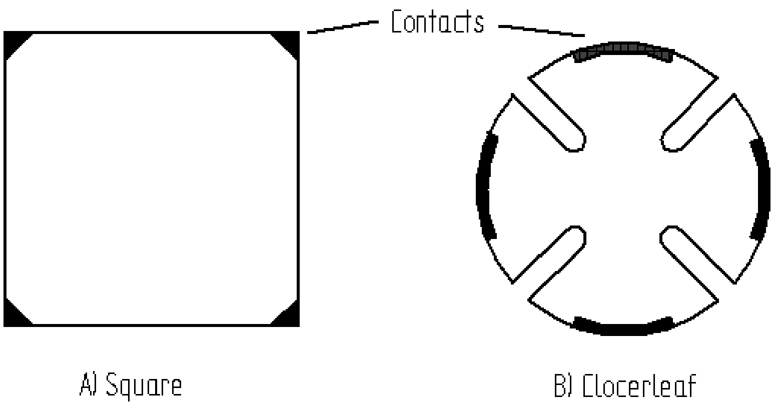

Figure 2.3 Two commonly used Hall sample shapes [1, 9].

One advantage of the cloverleaf pattern over the square is that the contacts can be comparatively larger while still retaining relatively low contact size related errors. If the necessary processing techniques are available and the sample is not too small, sample shape B offers distinct advantages in terms of accuracy.

2.3.4 Mixed Conduction

So far it has been assumed that conduction in a material occurs due to one carrier type only, either electrons or holes. If one considers strongly doped semiconductors in the extrinsic temperature region, this approximation is indeed justifiable, since under such conditions the concentration of one carrier type will outweigh that of the other by several orders of magnitude. If, however, one is working with weakly doped semiconductors at high temperatures or strongly compensated semiconductors, one can no longer assume that only one carrier type is involved in conduction. This holds especially if the mobility of the minority carriers is higher than that of the majority carriers. It can be shown that the Hall coefficient in the case of mixed conduction is given by [4, 5]

$$R_H = \frac{(N_p {\mu_p}^2 - N_e {\mu_e}^2)}{e(N_p \mu_p + N_e \mu_e)^2} \qquad (2.26)$$

From this it is seen that the Hall coefficient depends on the carrier densities as well as the mobilities of both carrier types. It should be noted that the sign of the Hall coefficient need not be equal to the sign of the majority carriers, since the mobility of the minority carriers may be higher than that of the majority carriers. Usually, this is only the case if the majority carriers are holes. If $N_e\mu_e >> N_p\mu_p$ or $N_p\mu_p >> N_e\mu_e$, equation 2.26 reduces to equations 2.7 or 2.8 respectively.

2.4 INHOMOGENEITY

2.4.1 Theoretical Introduction

As already mentioned in section 2.3 of this chapter, the van der Pauw analysis is only valid if the sample under consideration is laterally isotropic and homogeneous. It is, however, possible to analyze a sample that is inhomogeneous in the *z*-direction (depth) only [1]. It is convenient to describe this analysis in terms of aerial (sheet) quantities rather than volume quantities as was done in sections 2.1 through 2.3. Let R_{Hs}, σ_s, n_s and μ_s denote the sheet Hall coefficient, sheet conductivity, sheet Hall carrier concentration and sheet Hall mobility respectively. If one has a homogeneous sample with conductivity σ and thickness d in the *z*-direction, the corresponding sheet conductivity σ_s is given by [9]

$$\sigma_s = \sigma d \tag{2.27}$$

Now suppose that the sample is inhomogeneous in the *z*-direction, i.e. $\sigma = \sigma(z)$ is a non-constant function of z. For sufficiently small segments of thickness Δz_i, equation 2.27 will be valid since $\sigma(z)$ will not vary appreciably over such short distances. The total sheet conductivity of the sample can then be written as the sum of sheet conductivities of the individual segments [6]:

$$\sigma_s = \sum_{i=1}^{N} \sigma_i \Delta z_i = e\sum_{i=1}^{N} \mu_i n_i \Delta z_i \tag{2.28}$$

where the last equality follows from equations 2.9 and 2.25 and e is the elementary charge. In the limiting case of infinitesimally thin segments, equations 2.28 become integrals [1, 2]:

$$\sigma_s = \int_0^d \sigma(z)dz = e\int_0^d n(z)\mu(z)dz \tag{2.29}$$

Apart from σ_s, the aerial quantity $R_{Hs}\sigma_s^2$ is useful in depth inhomogeneity analyses. Equations 2.9 and 2.25 imply that $R_{Hs}\sigma_s^2 = en\mu^2 d$ in the case of homogeneous samples. Applying the same argument that led to equation 2.28, one obtains

$$R_{Hs}\sigma_s^2 = \sum_{i=1}^{N} R_{Hi}\sigma_i^2\Delta z_i = e\sum_{i=1}^{N} n_i\mu_i^2\Delta z_i \tag{2.30}$$

which in the infinitesimal case leads to [1, 2]

$$R_{Hs}\sigma_s^2 = e\int_0^d n(z)\mu^2(z)dz \tag{2.31}$$

Some examples of applying this depth analysis will now be given.

2.4.2 Applications of Depth Analysis

2.4.2.1 Hall Profiling

Sometimes doping profiles in semiconductors are not constant with depth. This is often the case if the dopants were introduced by ion implantation. Since simple Hall measurements offer no intrinsic way of depth discrimination (unlike capacitance-voltage measurements where depth profiles can be readily obtained), a special technique is required to extract depth profiles. This technique, called Hall profiling, will be discussed in this section.

To see how the analysis of section 2.4.1 can be applied in practice, consider the sample shown in figure 2.4. Suppose that resistivity and Hall measurements are done on the sample before the removal of layer j-1, yielding values of $(\sigma_s)_{j-1}$ and $(R_{Hs}\sigma_s^2)_{j-1}$. This layer of thickness Δz_{j-1}

is then removed, whereupon another set of measurements is done on the remaining sample with results $(\sigma_s)_j$ and $(R_{Hs}\sigma_s^2)_j$.

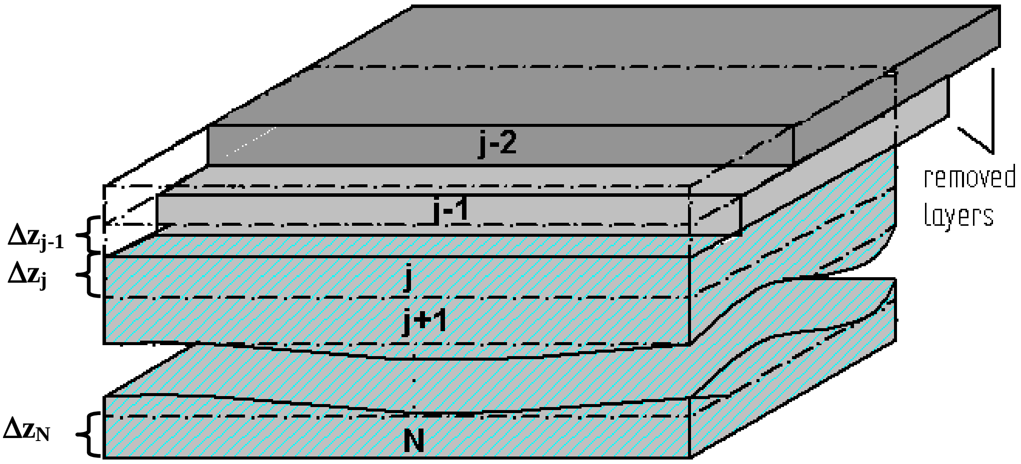

Figure 2.4. Illustration of the process of removing layers of thickness Δz_i from a sample. A Hall measurement is taken before and after each layer removal.

From equations 2.28 and 2.30 it follows that [6]

$$(\sigma_s)_{j-1} - (\sigma_s)_j = e\mu_{j-1} n_{j-1} \Delta z_{j-1} \tag{2.32}$$

and

$$(R_{Hs}\sigma_s^2)_{j-1} - (R_{Hs}\sigma_s^2)_j = e\mu_{j-1}^2 n_{j-1} \Delta z_{j-1} \tag{2.33}$$

provided of course that $\Delta z_{j\text{-}1}$ is sufficiently small so that the layer is homogeneous. These equations can now be solved to yield the carrier density and mobility of layer j-1 [1, 2, 6]:

$$\mu_{j-1} = \frac{(R_{Hs}\sigma_s^2)_{j-1} - (R_{Hs}\sigma_s^2)_j}{(\sigma_s)_{j-1} - (\sigma_s)_j} \tag{2.34}$$

$$n_{j-1} = \frac{((\sigma_s)_{j-1} - (\sigma_s)_j)^2}{\left[(R_{Hs}\sigma_s^2)_{j-1} - (R_{Hs}\sigma_s^2)_j\right] e\Delta z_{j-1}} \tag{2.35}$$

Hall profiling measurements suffer from a number of errors in addition to the ones already discussed in conjunction with standard Hall measurements (see section 2.3.1). Any errors in measuring the thickness Δz_{j-1} of the layer will obviously falsify the obtained mobility and carrier concentration values. In addition, the removal of the layer must be isotropic, i.e. the same thickness of material must be removed on the entire surface. If it is not, the assumptions of the analysis are no longer valid and the results will be in error. Finally, as equations 2.34 and 2.35 suggest, the mobility and carrier concentration values are determined by subtracting large quantities of which the difference can be quite small if Δz_{j-1} is small. This will amplify any existing errors in the measurement, and thus Δz_{j-1} should not be chosen to be too small.

2.4.2.2 Two-Layer Model

When a semiconductor layer is epitaxially grown on a substrate, a certain degree of lattice mismatch at the semiconductor-substrate interface can lead to a high defect concentration, giving rise to a degenerate interface layer. Such interface layers may be observed in ZnO or GaN samples grown epitaxially on sapphire. As will be shown in chapter 6, degenerate layers can also form at the surface of bulk ZnO due to gas adsorption or out-diffusion of impurities from the interior caused by annealing. Due to the high conductivity of this layer, its effect cannot be ignored even if its thickness is small compared to the epitaxial (bulk) layer. This becomes especially true at low temperatures where “freeze-out” occurs in the epitaxial (bulk) layer but not in the degenerate interface or surface layer. In this section it will be shown how to correct variable temperature Hall measurements for the effect of such degenerate layers.

To begin such an analysis, it is important to note that both carrier concentration and mobility are roughly constant with temperature in degenerate semiconductors [1, 2]. In addition, it is assumed that the degenerate interface layer is thin compared to the non-degenerate main layer. At very low temperatures (about 25 K or lower) the non-degenerate carriers in the main layer freeze out, effectively removing it electrically from the two-layer structure. Using the assumption of temperature-independent conductivity of the interface layer, one can simply treat this problem as a “layer removal” experiment as discussed in the previous section (section 2.4.2.1). The measurement before the layer removal corresponds to a measurement at a higher temperature where the main layer contributes significantly to the conduction. Similarly, the measurement after the layer removal corresponds here to a low temperature measurement in which the main layer is practically insulating. Thus identifying the main layer with the *j*-1th layer and the interface layer with the *j*th layer in figure 2.4, the corrected mobility $\mu_{corr}(T)$ and carrier concentration $n_{corr}(T)$ of the main layer as a function of temperature are given, using equations 2.34 and 2.35, by

$$\mu_{corr}(T) = \frac{(R_{Hs}\sigma_s^2)_T - (R_{Hs}\sigma_s^2)_{lowT}}{(\sigma_s)_T - (\sigma_s)_{lowT}} = \frac{(n\mu^2)_T - (n\mu^2)_{lowT}}{(n\mu)_T - (n\mu)_{lowT}} \tag{2.36}$$

$$n_{corr}(T) = \frac{((\sigma_s)_T - (\sigma_s)_{lowT})^2}{\left[(R_{Hs}\sigma_s^2)_T - (R_{Hs}\sigma_s^2)_{lowT}\right]ed} = \frac{((n\mu)_T - (n\mu)_{lowT})^2}{\left[(n\mu^2)_T - (n\mu^2)_{lowT}\right]} \tag{2.37}$$

where the subscripts “*T*” and “*lowT*” mean that the corresponding measurements were taken at some temperature *T* and at very low (freeze-out) temperature respectively. The quantities *n* and μ are the measured (uncorrected) volume carrier concentration and mobility values respectively and the main layer thickness is denoted by *d*. Since the interface or surface layer is very thin, the total layer thickness is practically equal to the main layer thickness.

Errors are introduced into these calculations by the fact that the carrier concentration and mobility of the interface layer is in fact not really constant but vary slightly with temperature. In addition, it may not be possible to cool down the sample to sufficiently low temperatures where the main layer becomes truly insulating. The transition between the main layer and the interface layer may also not be abrupt, violating the assumptions of the argument. It should also be noted that the correction works better for high temperature data points than for values close to freeze-out since in the latter case the corrected value depends more sensitively on the accuracy with which the interface layer mobility and carrier concentration was determined.

2.4.2.3 Rectifying Two-Layer Situation

When a sample consists of two layers with different carrier types, it is particularly easy to separate the layers. As shown in figure 2.5, the interface between the two layers forms a p-n junction, and for any two contacts on the surface of one layer, no current can flow through the other layer. This is due to the fact that the equivalent circuit for this case contains two back-to-back diodes in series with the other layer. As long as contacts are only made to one of the layers, only that layer will affect the measurement.

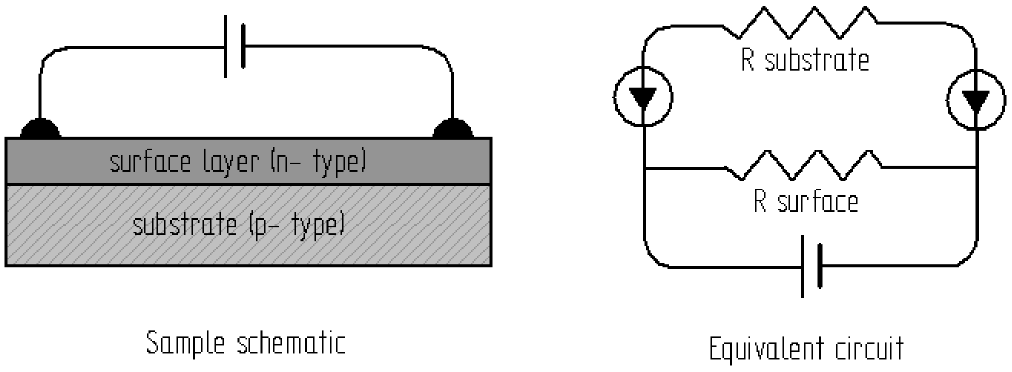

Sample schematic

Equivalent circuit

Figure 2.5 Two-layer sample with different carrier types

References

---

[1] Look D.C., *Methods in Materials Research* 5a.2.1- 5a.2.8 (Wiley, New York, 2000), 15 May 1998

[2] Look D.C., *Electrical Characterisation of GaAs Materials And Devices*, John Wiley & Sons, New York, 1989

[3] Griffiths D.J., *Introduction to Electrodynamics*, 3rd Edition, Prentice-Hall Inc., 1999

[4] Sze S.M., *Physics of Semiconductor Devices 2nd Edition*, John Wiley & Sons, 1981

[5] Seeger K., *Semiconductor Physics*, Springer series in Solid State Sciences, 40. Springer Verlag 1982

[6] Blood P.and Orton J.W., *The Electrical Characterisation Of Semiconductors*, Rep. Prog. Phys., Vol. 41, 1978

[7] van der Pauw L.J., *A Method of measuring specific resistivity and Hall Effect of discs of arbitrary shape*, Philips Res. Repts. 13, 1-9, 1958

[8] Goodman, S.A., *The charaterization of GaAs and AlGAs by the Hall effect*, Magister Scientiae Thesis, 1989

[9] Schroeder, D.K., *Semiconductor Materials and Device Characterization*, John Wiley & Sons, Inc, 1998

CHAPTER 3

SEMICONDUCTOR STATISTICS AND TRANSPORT THEORY

The results of Hall effect measurements relate to semiconductor statistics through the Hall carrier concentration and to transport theory through the extracted Hall mobility. It is therefore necessary to discuss both of these branches of semiconductor theory so that the maximum amount of information may be extracted from Hall measurements.

In this chapter, a relatively simple model for the carrier concentration is derived from general semiconductor statistics theory. This model is valid for compensated semiconductors with multiple shallow defect levels and is applied to ZnO in chapter 7. Semiconductor transport theory is discussed quite generally, and an elegant method by D.L. Rode for solving the Boltzmann transport equation is presented [1]. Details of how this method was implemented in this study are given in chapter 6. Analytic approximations for the temperature dependence of mobility for different scattering mechanisms are given in many books [2, 3]. Although such approximations can be helpful in the qualitative description of mobility trends as a function of certain material parameters, the most accurate and reliable computations must involve exact numerical computations. In the present work no approximations will be presented or implemented. Instead, Rode's method is applied to fitting the Hall mobility data and the results are given in chapter 7.

3.1 BAND STRUCTURE, SEMICONDUCTOR STATISTICS AND CARRIER CONCENTRATION

3.1.1 Band Structure

The energy band structure for diamond-like and spharelite-like crystal structures is known in great detail due to Kane, who made use of the. **k·p** method [1, 2, 3]. Both the carrier concentration and mobility depend on band structure. Fortunately, drift mobility in crystals does not depend sensitively on the finer details of the band structure, so that effects such as band anisotropy and spin-orbit splitting may be neglected [1]. Consequently, Kane's results may also be applied to other crystal structures such a wurtzite. The *E*-*k* relationship can be written in terms of the known parameters E_g (band gap), m (electron mass) and m^* (effective electron mass in the center of the Brilloin zone) **[1]**:

$$E(k) = \frac{\hbar^2 k^2}{2m} + \frac{E_g(\alpha - 1)}{2} \tag{3.1}$$

where

$$\alpha^2(k) = 1 + \frac{2\hbar^2 k^2}{mE_g}\left(\frac{m}{m^*} - 1\right) \tag{3.2}$$

It is also convenient to introduce a parameter d given by

$$d = 1/[1 + (m/m^* - 1)/\alpha] \tag{3.3}$$

d is the relative mass enhancement in a nonparabolic band, similar to the relative effective mass m^*/m in a parabolic band. In fact, d approaches the value m^*/m if k approaches zero or if E_g becomes large. In addition the parameters a and c, corresponding to the normalized coefficients of the s and p-type components of the conduction band wave function respectively, are useful in transport calculations and are given by **[1]**

$$a^2(k) = \frac{1 + \alpha}{2\alpha} \tag{3.4}$$

$$c^2 = 1 - a^2 \tag{3.5}$$

It is also of interest to note that the relationship between crystal momentum **k** and carrier velocity **v** is **[1]**

$$\mathbf{v} = \frac{\hbar \mathbf{k}}{m}\left(1 + \frac{m/m^* - 1}{\alpha}\right) \tag{3.6}$$

3.1.2 Modeling Multi-Donor Compensated Semiconductors

In this section an expression for the electron carrier concentration of a material with multiple shallow donor levels and an acceptor impurity concentration N_A will be given. Many of the results will be stated without rigorous derivation, and the reader is referred to references [1], [4] and [5] for more detail.

Since electrons obey Fermi-Dirac statistics, the probability of occupancy of the energy level E_j at thermal equilibrium n_j / g_j , also called the Fermi- Dirac distribution $f(E_i)$, is given by [4]

$$n_j / g_j = \frac{1}{\exp[(E_j - E_F)/k_B T] + 1} \tag{3.7}$$

where n_j is the number of electrons and g_j the number of available occupancy levels at energy E_j , E_F the Fermi energy, k_B Boltzmann's constant and T the Temperature. It can be shown that the number of states per unit of crystal volume in **k**-space is given by $(1/2\pi)^3$ such that $g(\mathbf{k})d\mathbf{k} = (1/2\pi)^3\, d\mathbf{k}$. Then d$n$, the number of electrons in the differential volume element $g(\mathbf{k})d\mathbf{k}$, can be written as [4]

$$dn = g_D (1/2\pi)^3 \frac{1}{1 + \exp[(E - E_F)/k_B T]} dk \tag{3.8}$$

with g_D the number of electrons per level (usually $g_D = 2$ for spin up and spin down) [5, 6]. In general, an isotropic nonparabolic band can be written in the form [1, 4]

$$\frac{\hbar^2 k^2}{2m^*} = \gamma(E) = E(1 + \alpha E) \tag{3.9}$$

where γ is an arbitrary function of E and the last equality is true for Kane bands as shown by equation 3.1. Substitution of equation 3.9 into equation 3.8, converting from momentum space to energy space and integrating yields, assuming small α [4]

$$\frac{n}{N_C} = \left[F_{1/2}\left(\frac{E_F}{k_B T}\right) + \frac{15}{4}\alpha k_B T F_{3/2}\left(\frac{E_F}{k_B T}\right) \right] \tag{3.10}$$

where $F_{1/2}$ and $F_{3/2}$ are Fermi integrals of order 1/2 and 3/2 respectively and N_C, the effective density of states in the conduction band, is given by [6]

$$N_C = 2\left(\frac{m^* kT}{2\pi\hbar^2}\right)^{3/2} \tag{3.11}$$

Assuming sufficiently small α and T, the second term on the right hand side of equation 3.10 is negligible, and for sufficiently large negative values of E_F/k_BT ($E_F/k_BT < -3$) the first term on the right hand side is approximately equal to $exp(E_F/k_BT)$, whence

$$n = N_C \exp[(E_F)/k_B T] \tag{3.12}$$

and E_F is measured relative to the conduction band minimum. Having thus found a simple expression that can easily be solved for the Fermi level and that can be related to experimental parameters, we turn our attention to finding a model for the carrier concentration in the conduction band.

The situation to be described is depicted in figure 3.1 [7]. There are a number of donor levels D_i with energies E_{D1} through E_{Dk} relative to the conduction band energy E_c. The corresponding donor impurity densities are N_{D1} through N_{Dk} , and it is assumed that the impurities are only singly ionized. Apart from the donor impurities, we assume shallow acceptor impurities of unknown activation energies and total concentration sufficiently small so that the material is n-type.

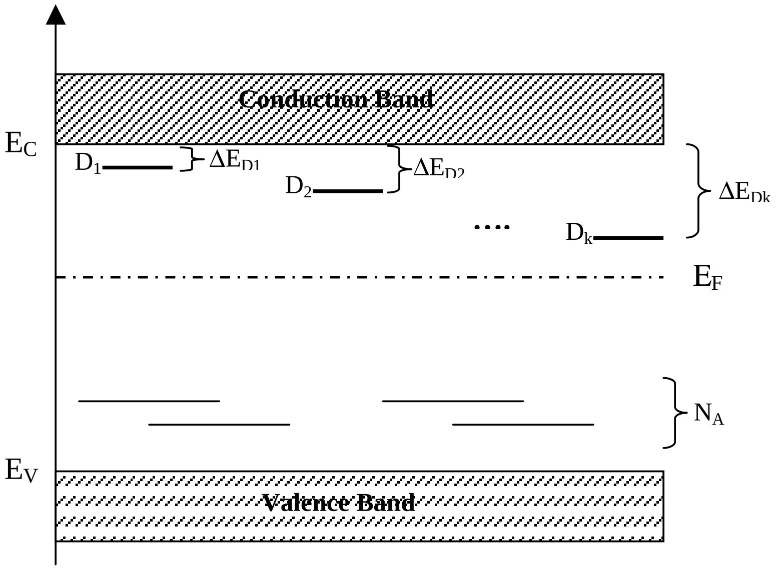

Figure 3.1 Energy levels in a multi- donor compensated semiconductor. The reference level is E_C

In the case of a donor impurity concentration N_D one obtains for the ratio of neutral to total donor sites N_D^0/N_D:

$$N_D{}^0 / N_D = \frac{1}{1/g_D \exp[(-E_F)/k_B T] + 1} \tag{3.13}$$

As always, E_F is measured relative to the conduction band minimum. With $N_D = N_D^0 + N_D^+$ where N_D^+ is the ionised donor concentration the following holds [4]

$$N_D{}^0 / N_D{}^+ = g_D \exp[(E_F - E_D)/k_B T] \tag{3.14}$$

Substituting E_F by equation 3.12, setting the donor ionisation energy $\Delta E_D = E_C - E_D = -E_D$ and using the fact that $N_D^0 = N_D - N_D^+$ one obtains, upon solving for N_D^+

$$N_D{}^+ = \frac{N_D}{\dfrac{g_D n}{N_C} \exp\left(\dfrac{\Delta E_D}{k_B T}\right) + 1} \tag{3.15}$$

The most general charge balance equation is given by

$$p + N_D^{\;+} = n + N_A^{\;-} = n + N_A - N_A^{\;0} \tag{3.16}$$

Assuming n-type conduction (as is the case for the ZnO samples used in the present study) this reduces to

$$N_D^{\;+} \approx n + N_A \tag{3.17}$$

since p is negligible and practically all acceptor sites are filled. In general, ΔE_D is a linear function of temperature, but this dependency will be neglected here. This assumption is probably accurate in the case of shallow donors. equations 3.15 and 3.17 are now applied to the multi-donor situation discussed above, yielding the final result that can be used to model the ZnO carrier concentration data **[5]**

$$n + N_A = \sum_{i=1}^{k} \left[\frac{N_{Di}}{1 + \dfrac{g_{Di} n T^{-3/2}}{N_C(1)} \exp\left(\dfrac{\Delta E_{Di}}{k_B T} \right)} \right] \tag{3.18}$$

$N_C(1)$, the effective density of states at 1 K, is calculated using equation 3.11. Assuming two-level *s*-like donor states, $g_{Di} = 2$. The remaining fitting parameters are thus the donor concentrations N_{Di} and their respective activation energies ΔE_{Di}. In addition, the acceptor concentration N_A is also a fitting parameter.

3.2 TRANSPORT THEORY

3.2.1 Solving the Boltzmann Transport Equation

The nonequilibrium behavior of a collection of particles is described by the Boltzmann transport equation [8]

$$\frac{\partial f_T}{\partial t} = \left(\frac{\partial f_T}{\partial t}\right)_{force} + \left(\frac{\partial f_T}{\partial t}\right)_{diff} + \left(\frac{\partial f_T}{\partial t}\right)_{coll} \tag{3.19}$$

where $f_T = f_T(\mathbf{k}, t)$ is the distribution function of a collection of particles subject to an accelerating force, diffusion effects and collisions. The Boltzmann transport equation thus expresses the rate of change of an arbitrary distribution function as a sum of three contributing terms: The rate of change due to the external driving force $(\partial f_T/\partial t)_{force}$ (e.g. an electric field), the rate due to particle diffusion in the presence of thermal gradients $(\partial f_T/\partial t)_{diff}$ and the rate of change resulting from collisions with other particles $(\partial f_T/\partial t)_{coll}$. Once expressions for these terms have been found one can solve for the total distribution function f_T. To this end, it is convenient to write f_T as a sum of two contributing terms [1, 3, 9]:

$$f_T(\mathbf{k}) = f + xg \tag{3.20}$$

where $f = f(\mathbf{k})$ is the equilibrium part of the distribution, $g = g(\mathbf{k})$ the perturbation part (due to the external field, scattering etc.) and x the cosine of the angle between the driving force $\mathbf{F}_\mathrm{d}$ and $\mathbf{k}$. Equation 3.20 is a first order expansion in the driving force, and is valid for a small driving force only.

For the case of an electron gas in a crystal, f is simply the Fermi- Dirac distribution and $\mathbf{F}_\mathrm{d} = e\mathbf{E}$ where e is the charge of an electron and $\boldsymbol{E}$ the applied electric field. Via the definition of the derivative it can be shown that the force term in equation 3.19 can be written as [1]

$$\left(\frac{\partial f_T}{\partial t}\right)_{Force} = -\mathbf{a}\cdot\frac{\partial f_T}{\partial \mathbf{v}} = -\frac{e}{\hbar}\mathbf{E}\cdot\frac{\partial f_T}{\partial \mathbf{k}} \tag{3.21}$$

where the second equality follows from $\mathbf{a} = e\mathbf{E}/md$ and $\mathbf{v} = \hbar\mathbf{k}/md$ with **a** the acceleration, **v** the velocity and md the effective mass in a Kane Band. To find an expression for the collision term in equation 3.19 one considers the differential scattering rate $s = s(\mathbf{k}, \mathbf{k}')$ for an electron making the transition from **k** to **k**' and the differential scattering rate $s' = s(\mathbf{k}', \mathbf{k})$ for a transition of the electron from **k**' to **k.** The probability of transition from **k** to **k**' is $sf_T(1\text{-}f_T')$ and the corresponding probability for a transition from **k**' to **k** is $s'f_T(1\text{-}f_T)$. Subtraction of the second term from the first and integration over all the **k**' states one obtains the collision term. In the steady state, $\partial f_T/\partial t = 0$, and assuming negligible thermal gradients equation 3.19 becomes [1]

$$\frac{e}{\hbar}\mathbf{E}\cdot\frac{\partial f_T}{\partial \mathbf{k}} = \int [s' f_T'(1-f_T) - sf_T(1-f_T')]d\mathbf{k}' \tag{3.22}$$

Substitution of equation 3.20 into this expression and integration over x yields, after some algebraic manipulation [1],

$$\frac{eE}{\hbar}\frac{\partial f_T}{\partial k} = \int Xg'[s'(1-f) + sf]d\mathbf{k}' - g\int[s(1-f') + s'f']d\mathbf{k}' \tag{3.23}$$

where X is the cosine of the angle between **k** and **k**'. Once the volume integration over **k**' has been performed, equation 3.23 is independent of the angular coordinate X, and becomes a function of k only. In order to simplify this expression further, one distinguishes between elastic and inelastic scattering rates $s = s_{el} + s_{inel}$. Scattering is termed elastic if the energy of a carrier does not change appreciably during a collision with a phonon. This is only the case when the phonon energy is much less than the thermal energy of the carrier. If the phonon energy becomes comparable or even larger than the thermal energy of the carrier, as is the case for polar optic phonons, carrier energy is not conserved during a collision, and inelastic scattering occurs. In terms of s_{el} and s_{inel}, equation 3.23 becomes [1, 3, 9]

$$\begin{aligned} & g\left\{\int [s_{inel}(1-f')+s'_{inel}\; f']d\mathbf{k}' + \int (1-X)s_{el}\,d\mathbf{k}'\right\} \\ & = \int Xg'[s'_{inel}(1-f)+s_{inel}\,f]d\mathbf{k}' - \frac{eE}{\hbar}\frac{\partial f}{\partial k} \end{aligned} \tag{3.24}$$

Physically, the first integral on the left hand side of equation 3.24 represents the rate with which carriers are scattered *out* of the differential volume element d**k**, and one defines the scattering out rate by

$$S_o = \int [s_{inel}(1-f')+s'_{inel}\; f']d\mathbf{k}' \tag{3.25}$$

Similarly, the rate of scattering into the differential volume element d**k,** S_i, is given by the integral on the right hand side of equation 3.24

$$S_i(g') = \int Xg'[s'_{inel}(1-f)+s_{inel}\,f]d\mathbf{k}' \tag{3.26}$$

The second integral on the left hand side is the elastic scattering rate v_{el}:

$$v_{el} = \int (1-X)s_{el}\,d\mathbf{k}' \tag{3.27}$$

Substitution of equations 3.25, 3.26 and 3.27 into equation 3.24 and solving for the perturbation distribution g yields **[1]**

$$g = \frac{S_i(g') - (eE/\hbar)(\partial f/\partial k)}{S_o + v_{el}} \tag{3.28}$$

Since the right hand side of this equation depends on g' due to the $S_i(g')$ term, the equation has to be solved iteratively. This is done in the following way:

Set $g_0 = 0$ and calculate $S_i(0)$, whereupon g_1 is calculated. The value obtained for g_1 is then used to calculate $S_i(g_1)$ which in turn is used to calculate g_2, etc. For $j = 0, 1, 2,\ldots$ the following recursion formula holds **[1]**:

$$g_{j+1} = \frac{S_i(g_j') - (eE/\hbar)(\partial f/\partial k)}{S_o + v_{el}} \tag{3.29}$$

Usually less than 10 iterations are required until a tolerance of 10^{-3} is satisfied **[2]**. Even when $S_i(g)$ is taken as zero and only one iteration is performed, good results are often obtained. This simplification is known as the relaxation approximation. In the relaxation approximation, the momentum relaxation time τ can be thought of as the time constant associated with the decay of the momentum of the carriers to the thermal equilibrium values after any external perturbations are removed. Quantitatively the relaxation time is given simply by the inverse of the scattering rate $(v_{el} + S_o) = 1/\tau$ **[1, 2]**, so that the perturbation distribution g becomes

$$g = -\frac{eE\tau}{\hbar}\frac{\partial f}{\partial k} \tag{3.30}$$

The value of g determined in either the relaxation approximation or the more exact iterative procedure can now be used to evaluate the drift mobility. By definition, mobility is the average carrier drift velocity per unit electric field in the low field limit (see equation 2.20). The mobility is then given by **[1, 2, 3, 9]**:

$$\mu = \frac{\hbar}{2m}\frac{\int_0^\infty k^3 (g/Ed)\,dk}{\int_0^\infty k^2 f\,dk} \tag{3.31}$$

In general, the integrals in this expression must be solved numerically.

3.2.2 Calculating the Hall Scattering Factor

Recall that in section 2.1, the Hall coefficient was derived under the assumption that the carriers in the sample all moved with the same constant velocity. In semiconductors, this assumption is generally invalid. To obtain a more accurate expression for R_H, the details of the perturbed electron momentum distribution must be considered. Assuming that a relaxation time exists, at least to some approximate degree, the equation of motion of a charge carrier of charge q may be written as follows [2, 10]

$$m^* d\mathbf{v}/dt = -q(\mathbf{E} + \mathbf{v}\times\mathbf{B}) - m^*(\mathbf{v} - \mathbf{v}_{\mathbf{eq}})/\tau \qquad (3.32)$$

where m^* is the effective mass, **v** the velocity, $\mathbf{v}_{\mathbf{eq}}$ the equilibrium velocity and τ the relaxation time, which is a function of energy or momentum. It should be noted that equation 3.32 reduces via Newton's second law to equation 2.2 in the steady state ($d\mathbf{v}/dt = 0$) if the velocity is equal to the equilibrium velocity. Here, however, it will be assumed that $\mathbf{v} \neq \mathbf{v}_{\mathbf{eq}}$. Upon solving the system of coupled differential equations (equation 3.32) and averaging over the energy distribution of carriers in a semiconductor using the Fermi- Dirac function one obtains for the current densities j_x and j_y (x and y components of **j**, refer to figure 2.1) [2, 3, 9]

$$j_x = \left\langle \frac{\tau}{1+\omega_c^2\tau^2} \right\rangle E_x - \left\langle \frac{\omega_c\tau^2}{1+\omega_c^2\tau^2} \right\rangle E_y \qquad (3.33)$$

$$j_y = -\left\langle \frac{\omega_c\tau^2}{1+\omega_c^2\tau^2} \right\rangle E_x + \left\langle \frac{\tau}{1+\omega_c^2\tau^2} \right\rangle E_y \qquad (3.34)$$

where $\omega_c = eB/m^*$ is the cyclotronic frequency and E_x and E_y the x and y components of the electric field respectively, as shown in figure 2.1. The brackets denote averaging over energy in the following way [10]:

$$\langle F(E) \rangle = \frac{\int_0^\infty (F(E)E^{3/2}(\partial f/\partial E)dE}{\int_0^\infty E^{3/2}(\partial f/\partial E)dE} \qquad (3.35)$$

The function f in this expression is simply the Fermi-Dirac function and $F(E)$ is an arbitrary function of E, e.g. $\tau(E)$. Now, in the low magnetic field limit, $\omega_c\tau \ll 1$ so that the bracketed expressions in equations 3.33 and 3.34 can be simplified somewhat. Imposing once again the condition that $j_y = 0$ (refer section 2.1) one finds that [10]

$$j_x = \frac{nq^2\langle\tau\rangle}{m^*}E_x \tag{3.36}$$

which through the familiar formula for conductivity mobility μ_c [2]

$$\mu_c = \frac{|q|\langle\tau\rangle}{m^*} \tag{3.37}$$

yields

$$j_x = nq\mu_c E_x \tag{3.38}$$

Now, from equation 2.6 we know that the Hall coefficient is given by $R_H = j_x B/E_y$
So that one obtains, using equations 3.33, 3.34 and 3.36 [2, 3, 10],

$$R_H = \frac{1}{|n|q}\frac{\langle\tau^2\rangle}{\langle\tau\rangle^2} = \frac{r_H}{|n|q} \tag{3.39}$$

The Hall scattering factor is thus given by [5, 10]:

$$r_H = \frac{\langle\tau^2\rangle}{\langle\tau\rangle^2} = \frac{\int_0^\infty (\tau^2 E^{3/2}(\partial f/\partial E)dE}{\int_0^\infty \tau E^{3/2}(\partial f/\partial E)dE}\int_0^\infty E^{3/2}(\partial f/\partial E)dE \tag{3.40}$$

Converting these integrals to *k*-space and recalling that $\tau = 1/(S_o + v_{el})$, one obtains

$$r_H = -3\frac{m}{m^*}\frac{\int_0^{\infty}\frac{k^3}{d}\frac{\partial f}{\partial k}\left[1/(S_o+v_{el})\right]^2 dk}{\left[\int_0^{\infty}\frac{k^3}{d}\frac{\partial f}{\partial k}\left[1/(S_o+v_{el})\right]dk\right]^2}\int_0^{\infty}k^2 f dk \qquad (3.41)$$

Recall that d is given by equation 3.3. The scattering rates S_o and v_{el} are quantified in section 3.2.3. Of course g and f must be written in terms of momentum rather than energy in this expression. Since S_o and v_{el} are given in terms of k rather than E in the next section, equation 3.41 rather than 3.40 will be used to calculate r_H. It should be noted that equation 3.41 gives the Hall scattering factor in the relaxation time approximation, unlike the formula for mobility (equation 3.31), which is exact if g is evaluated via the iterative method given in equation 3.29. More exact calculations of r_H are possible (Monte Carlo methods) [11] but also more complex and computationally expensive. For many practical purposes, including the data fitting in the present study, equation 3.41 is sufficiently accurate.

3.2.3 Qualitative Description of the Scattering Mechanisms in Crystals

In order to understand the temperature dependence of the carrier mobility, one needs to discuss and quantify the various scattering mechanisms that are of importance in a given material. In this section, a general overview of most of the important scattering mechanisms will be given, and the important scattering rates for compound semiconductors, in particular ZnO, will be quantified. The most important scattering mechanisms are given in figure 3.2 [4].

An ideal crystal is a perfectly periodic structure of unit cells without deviation, thermal vibration or impurities. Obviously, most of the imperfections mentioned in figure 3.2 occur in real crystals to a greater or lesser extent. Discontinuities such as edge or screw dislocations are usually formed during crystal growth and act as centers for charge accumulation. The perturbing potential thus created causes carrier scattering. Usually the number of crystal defects in properly grown crystals is low enough so that this type of scattering is dwarfed by other mechanisms and can consequently be neglected [1, 4, Error! Bookmark not defined.].

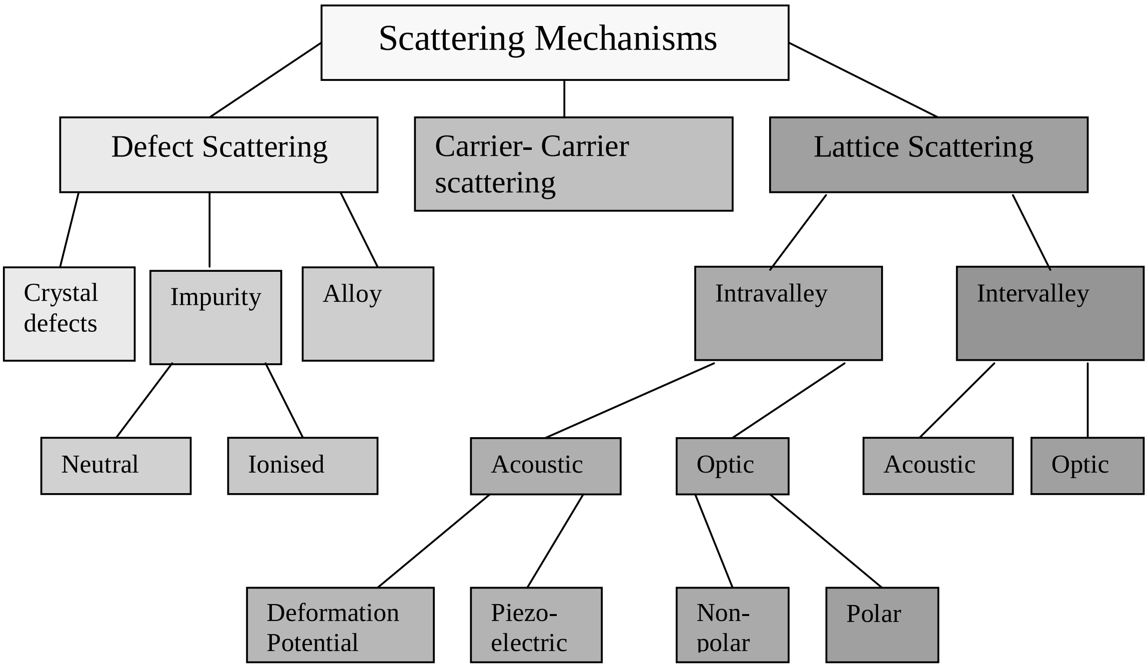

Figure 3.2 The most important scattering mechanisms in semiconductor crystals [4]

If the semiconductor is composed of a mixture of two or more different compounds, no definite crystal structure can form since the compounds will in general have incompatible intrinsic crystal structures. Thus discontinuities will be spread randomly throughout the structure, giving rise to alloy scattering. This type of scattering obviously does not occur in pure compounds.

Usually, impurity atoms are present in the lattice. Their origin may be unintentional as part of the crystal growth process or intentional in the form of doping atoms. Depending on how deep the resulting donor / acceptor levels are located, these dopant sites will become ionized above a certain temperature, normally around liquid helium temperature for shallow doping. Thus, at very low temperatures, most impurity atoms are neutral and neutral impurity scattering occurs. As temperature is increased, the donor / acceptor sites become ionized, leaving charged scattering centers behind. This is one of the dominant scattering mechanisms in doped semiconductors in the 10 K- 300 K region [2, 4]. Above around 100 K, ionized impurity scattering decreases since the scattering probability of charged centers is less in the case of high-energy carriers.

We now turn our attention to scattering due to the lattice. Because of the finite temperature of a crystal, the atoms vibrate around their equilibrium lattice sites. These vibrations cause time-dependent changes in the carrier states. A quantum mechanical treatment requires the introduction of phonons, which are particles with momentum $\hbar\mathbf{k}$ and energy $\hbar\omega$, where $\hbar\mathbf{k}$ is the wave vector, ω the phonon frequency and $\hbar$ Planck's constant divided by 2π. Phonons, like photons, obey Bose-Einstein statistics as well as the laws of conservation of energy and momentum during collisions with other particles such as electrons.

There exist different types of lattice vibrations resulting in phonons of different energies. Neighboring atoms can vibrate either in phase or out of phase. The first case is analogous to the propagation of an acoustic wave, and the phonons associated with such vibrations are called acoustic phonons. The direction of the **k**-vector can be either parallel of perpendicular to the atomic vibrations, corresponding to longitudinal and transverse acoustic phonons respectively. The periodic change in gap energy as a result of these vibrations causes what is known as deformation potential scattering [2, 4].

Another type of acoustic phonon scattering occurs in crystals with molecules that are not totally symmetric. As an acoustic wave propagates through the crystal, the shape of the constituent molecules is distorted, changing the position of polarized atoms. This gives rise to a potential due to the piezoelectric effect, which in turn scatters carriers. Piezoelectric scattering is important in all compound semiconductors, usually at low temperatures [2, 4].

The vibration of neighboring atoms in opposite phase either longitudinally or transversal are known as optical modes of vibration, giving rise to optical phonons which normally have a higher frequency than their acoustic counterparts. Again, two different cases need to be distinguished. Like acoustic vibrations, optic vibrations produce strain in the lattice, thus perturbing the energy levels. Since the strain is usually less than for acoustic vibrations, the significance of this nonpolar optic interaction is of little significance, except in crystal directions where the band energy does not change rapidly with **k**. This occurs in aluminium, gallium and lead compounds. Polar optic scattering is of greater importance, and it occurs due to the change in potential by optic strain induced shift of polarized atoms. This is one of the dominant scattering effects above 80 K [2, 5].

Scattering effects can be classified even further into intravalley and intervalley scattering. In the former, carriers remain within the same valley after scattering, the energy and momentum of the phonon not being sufficient to scatter the carrier to another valley. This type of scattering is usually dominant at and below room temperature in the case of low field transport.

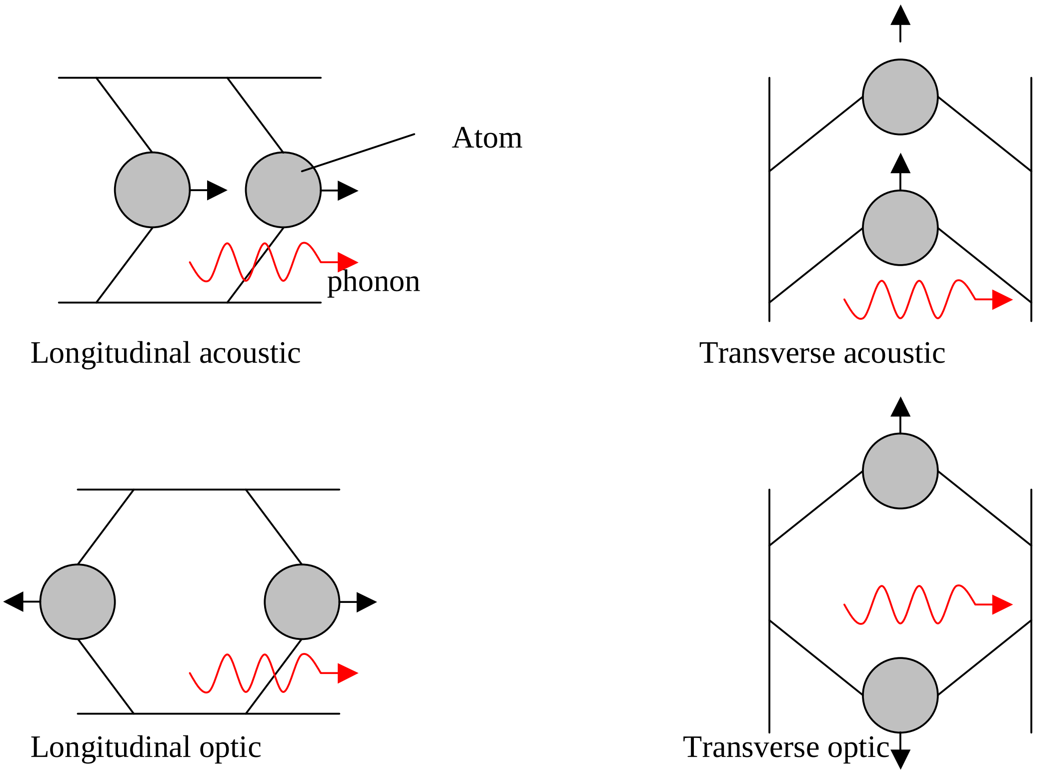

Figure 3.3 Illustration of optic and acoustic lattice vibrations

Intervalley scattering occurs when a carrier interacts with a phonon of large momentum and is thus scattered to a different valley of the same energy. This type of scattering is more likely at high temperatures. To scatter carriers from a low valley to a higher one requires large fields, and this type of intervalley scattering is negligible in low field transport.

Finally, carriers can also interact with each other in what is known as carrier- carrier scattering. Carriers of opposite charge travel in opposite directions, and an encounter would lead to complete annihilation, thus effectively decreasing mobility. Carriers of the same type also interact through coulombic forces, but there is no direct effect on the mobility since they all move in the same direction. Such interactions, however, serve to randomize the motion and have an indirect effect through the other dominant scattering mechanisms. Carrier-carrier scattering can become important when the carrier density exceeds 10^{14} cm^{-3} **[3, 4]**

3.2.4 Calculating the Relevant Scattering Rates

The scattering mechanisms of importance in the present study will now be discussed and quantified, so that the results can be used in the equations of sections 3.2.1 and 3.2.2 to fit the mobility data and calculate the Hall scattering factor. These mechanisms are piezoelectric and deformation potential longitudinal acoustic phonons, polar optic phonons and ionized impurity scattering. The derivation of the scattering rates will not be given in detail here, the focus being the practical implementation of the predicted results. Complete derivations are given in Rode **[1]**, Seeger **[2]** or Nag **[4, 9]**.

3.2.4.1 Ionized Impurity Scattering

In n-type semiconductors below room temperature, ionized scattering centers are mainly due to ionized dopant atoms and holes. The scattering rate to be used here is due to a theory by Dingle **[1]**. In this treatment, it is assumed that the scattering centers and holes are stationary, i.e. that the thermal vibrations of the lattice have no significant impact on the electrostatic potential of the ionized centers. The effect of neutral impurities, the concentration of which is large at low temperatures, is also neglected. It is assumed that the ions are singly charged, and that the surrounding electron gas screens their potential. No screening occurs due to holes, which are assumed to move randomly. Instead of the usual potential proportional to inverse distance, the form of the potential is $\varphi = (q/4\pi\varepsilon_0 r)\exp(-\beta r)$, where q is the charge of a proton, ε_0 the dielectric constant of the material at low frequencies (not to be confused with the dielectric constant of vacuum, which is also sometimes called ε_0), r the distance from the charge and β the inverse screening length given by

$$\beta^2 = (e^2 / \varepsilon_0 k_B T) \int (k/\pi)^2 f(1-f) dk \qquad (3.42)$$

It is assumed that the concentration of ionized impurities is small, so that the distance between ions is much greater than the screening length. Since the ions and holes are heavy compared with electrons, the scattering is elastic, so that the scattering rate $s = s'$. The potentials $\varphi(\mathbf{r}, \mathbf{R})$, where $\mathbf{R}$ is the random position of the ion, are added to yield the total potential $V(\mathbf{r})$, and the square of the matrix element of this potential between $\mathbf{k}$ and $\mathbf{k}'$ is proportional to the scattering rate $s(\mathbf{k}, \mathbf{k}') = s(\mathbf{k}', \mathbf{k})$. The resultant expression is substituted into equation 3.27 and evaluated. The result is [1]

$$v_{ii} = (e^4(n+2N_A)md/(8\pi\varepsilon_0{}^2\hbar^3k^3))\left[D\ln(1+4k^2/\beta^2)-B\right] \tag{3.43}$$

where

$$D = 1+(2\beta^2c^2/k^2)+(3\beta^4c^4/4k^4) \tag{3.44}$$

$$B = \frac{4k^2/\beta^2}{1+4k^2/\beta^2} + 8\frac{\beta^2+2k^2}{\beta^2+4k^2}c^2 + \frac{3\beta^4+6\beta^2k^2-8k^4}{(\beta^2+4k^2)k^2}c^4 \tag{3.45}$$

The ionized impurity scattering rate is proportional to the total ionized impurity concentration, which via equation 3.17 and the assumption that all acceptors are ionized leads to the factor $n + 2N_A$. Since v_{ii} is inversely proportional to k^3, this type of scattering will dominate at low temperatures where k is small. The parameters D and B take care of the non-parabolicity of the band. For large gaps (e.g. 3.4 eV in the case of ZnO), c approaches zero (see equations 3.4 and 3.5) and simpler expressions can be found for D and B. Since v_{ii} is an elastic scattering rate, it is to be added directly to v_{el} in equation 3.28.

3.2.4.2 Piezoelectric Acoustic Modes

Longitudinal acoustic waves induce a strain, the gradient of which is proportional to the resulting piezoelectric potential. The constant of proportionality is related to a dimensionless constant, called the piezoelectric coupling constant P, and the scattering rate is proportional to P^2, and inversely proportional to ε_0 since a large dielectric constant weakens the perturbing piezoelectric field. Since acoustic waves have a long wavelength, piezoelectric scattering is elastic. The scattering rate is [1]

$$v_{pe} = \frac{e^4 k_B T P^2 m d}{6\pi\hbar^3 \varepsilon_0 k}(3-6c^2+4c^4) \tag{3.46}$$

and is to be added to v_{el}. Piezoelectric scattering is significant from 50 K up to room temperature.

3.2.4.3 Deformation Potential Acoustic Modes

In the case of deformation potential scattering, the longitudinal modes are also dominant. This type of scattering is characterized by the deformation potential E_l, which gives the amount of energy in eV by which the gap energy changes per unit strain. The elastic constant c_l, which determines the necessary stress required to induce a certain strain, is also an important parameter in determining deformation potential scattering. The scattering rate is [1]

$$v_{ac} = \frac{e^2 k_B T E_l^{\,2} m d k}{3\pi\hbar^3 c_l}(3-8c^2+6c^4) \tag{3.47}$$

3.2.4.4 Polar Optic Modes

In compound semiconductors, longitudinal optic vibrations induce electric polarization waves with associated phonon energy $k_B T_{po}$, where T_{po} is the Debye temperature. Since T_{po} is typically much larger than room temperature, scattering due to polar optic phonons cannot be regarded as elastic, and their scattering rate cannot be combined directly with the other scattering rates. Instead, scattering out- and scattering in rates have to be calculated. Polar optic scattering is responsible for the fact that g has to be calculated iteratively, as $g(E)$ becomes related to $g(E \pm k_B T_{po})$. Scattering can occur in two ways: phonon emission and absorption. The differential scattering rate is proportional to the polar optic phonon energy

k_BT_{po} and also depends on both the low frequency and high frequency dielectric constants ε_0 and ε_∞. The differential scattering rate due to absorption is also proportional to N_{po}, the average number of phonons contained in a polar optic mode. The corresponding factor for scattering by emission is $N_{po}+1$, since the energized carrier itself also counts as a phonon in this case. Since phonons obey Bose- Einstein statistics, N_{po} is given by

$$N_{po} = \frac{1}{\exp(T_{po}/T)-1} \tag{3.48}$$

The differential scattering rate (given on p 39 in reference [1]) is substituted into equation 3.25, and S_o is found to be

$$S_o = (N_{po}+1-f^-)\lambda_0^- + (N_{po}+f^+)\lambda_0^+ \tag{3.49}$$

Throughout, the superscripted plus and minus signs mean that the relevant quantity should be evaluated at energy $E \pm k_BT_{po}$. Since all the quantities have been given in terms of k, we first have to solve for k^+ and k^-:

$$E + k_BT_{po} = \frac{\hbar^2(k^+)^2}{mE_r} + \frac{E_g(\alpha(k^+)-1)}{2} \tag{3.50}$$

$$E - k_BT_{po} = \frac{\hbar^2(k^-)^2}{mE_r} + \frac{E_g(\alpha(k^-)-1)}{2} \tag{3.51}$$

where equation 3.1 has been used. No analytic solutions exist for these equations, and they have to be solved numerically. For the case of a parabolic band analytic solutions are, however, readily obtained. The other symbols in equation 3.49 are given by

$$\lambda_o^+(k) = \beta^+\left[(A^+)^2 \ln\left|\frac{k^+ + k}{k^+ - k}\right| - A^+c^+c - aa^+cc^+\right] \tag{3.52}$$

$$\beta^{+} = \frac{e^{2} k_{B} T_{po} m d^{+}}{4\pi\hbar^{3} k}\left(\frac{1}{\varepsilon_{\infty}} - \frac{1}{\varepsilon_{0}}\right) \tag{3.53}$$

$$A^{+} = a a^{+} + \frac{(k^{+})^{2} + k^{2}}{2k^{+}k} c c^{+} \tag{3.54}$$

Replacing all superscripted + by -, one obtains the corresponding expressions for λ_0^-. The scattering in rate is given by

$$S_i(g') = (N_{po} + f)\lambda_i^{-} g^{-} + (N_{po} + 1 - f)\lambda_i^{+} g^{+} \tag{3.55}$$

Physically, λ_o^+, λ_o^-, λ_i^+ and λ_i^- are the scattering rates at $E \pm k_B T_{po}$. The in-scattering rates are given by

$$\lambda_i^{+}(k) = \beta^{+}\left[\frac{(k^{+})^{2} + k^{2}}{2k^{+}k}(A^{+})^{2} \ln\left|\frac{k^{+} + k}{k^{+} - k}\right| - (A^{+})^{2} - \frac{c^{2}(c^{+})^{2}}{3}\right] \tag{3.56}$$

where again all + are to be replaced with – for λ_i^-. All results necessary for transport calculations in single crystal ZnO have now been stated, and we proceed to apply these results in chapters 6 and 7.

References

---

[1] Rode D.L., Semiconductors and Semimetals Volume 10, Academic Press 1975.

[2] Seeger K., *Semiconductor Physics*, Springer series in Solid State Sciences, 40. Springer Verlag 1982

[3] Askerov B.M., *Electron Transport Phenomena In Semiconductors*, World Scientific Publishing 1994

[4] Nag B.R., *Electron Transport in Compound Semiconductors*, Springer Series in Solid State Sciences 11. Springer Verlag 1980

[5] Look D.C., *Electrical Characterisation of GaAs Materials And Devices*, John Wiley & Sons, New York, 1989

[6] Sze S.M., *Physics of Semiconductor Devices* 2nd Edition, John Wiley & Sons, 1981

[7] Blood P. and Orton J.W., *The Electrical Characterisation Of Semiconductors*, Rep. Prog. Phys., Vol. 41, 1978

[8] McGrath Encyclopedia of Science and Technology, John Wiley & Sons

[9] Nag B.R., *Theory Of Electrical Transport In Semiconductors*, Pergamon Press 1972

[10] Look D.C., *Methods in Materials Research* 5a.2.1- 5a.2.8 (Wiley, New York, 2000), 15 May 1998

[11] Kinsler P., *The Hall effect and ionized impurity scattering in* $Si_{(1-x)}Ge_x$, Sigeliim preprint, 2003

CHAPTER 4

PROPERTIES OF ZINC OXIDE (ZnO)

Zinc Oxide (ZnO) was one of the first semiconductors to be prepared in rather pure form after silicon and germanium. It was extensively characterized as early as the 1950's and 1960's due to its promising piezoelectric/ acoustoelectric properties [1]. A greater range of applications for ZnO has been hampered by the difficulty of realizing good quality p-type material. In the 1990's a revival of interest in ZnO occurred for diverse reasons. A very commonly cited property is the large exciton binding energy of 60 meV which makes ZnO a promising candidate for semiconductor lasing applications [7]. Optoelectronic devices such as blue and ultra-violet emitters and detectors are further potential applications. In addition, the electrical properties of ZnO have been shown to be strongly affected by certain gases such as hydrogen, ammonia and ethanol, making this material a good candidate for gas sensing applications [2, 3, 4]. Many reports of the realization of p-type material have been published in the last decade, but consistently reproducible and stable p-type ZnO seems to remain elusive. A good understanding of deep and shallow electrical defects in ZnO is still lacking, and the role of highly conductive surface channels has only recently come under the spotlight [5, 6] . A better understanding of these phenomena will lead to more consistent progress in the quest not only for p-type ZnO but also for ZnO devices in general.

The purpose of this chapter is threefold: to provide well established information of structural and electrical properties that are of importance in carrier statistics and transport calculations and to summarize some of the more recent research that is of relevance in the investigation of bulk ZnO via the temperature dependent Hall technique. In addition, the three main methods of commercial bulk ZnO growth will be discussed since this study is to a large extent devoted to the characterization of bulk single-crystal material.

4.1 STRUCTURAL PROPERTIES AND BAND STRUCTURE

4.1.1 Crystal Structure

Zinc Oxide crystallizes in three lattice types: rock salt, zinc blende and wurtzite. Bulk ZnO at ambient pressure is only stable in the wurtzite modification. The zinc blende structure can be achieved through growth on cubic substrates while the rock salt modification exists only at high pressures [7]. Figure 4.1 shows the wurtzite ZnO structure, which may be regarded as two inter-penetrating close packed hexagonal sub-lattices where each sub-lattice consists of one type of atom (zinc and oxygen respectively) [7, 8]. The two sub-lattices are shifted relative to each other by *a* distance *b* along the common *c*-axis ([0 0 0 1] direction). The lattice is symmetric about this axis. ZnO wafers are often cut so that the *c*-axis is perpendicular to the wafer surface, and all samples measured in this study were cut in this way.

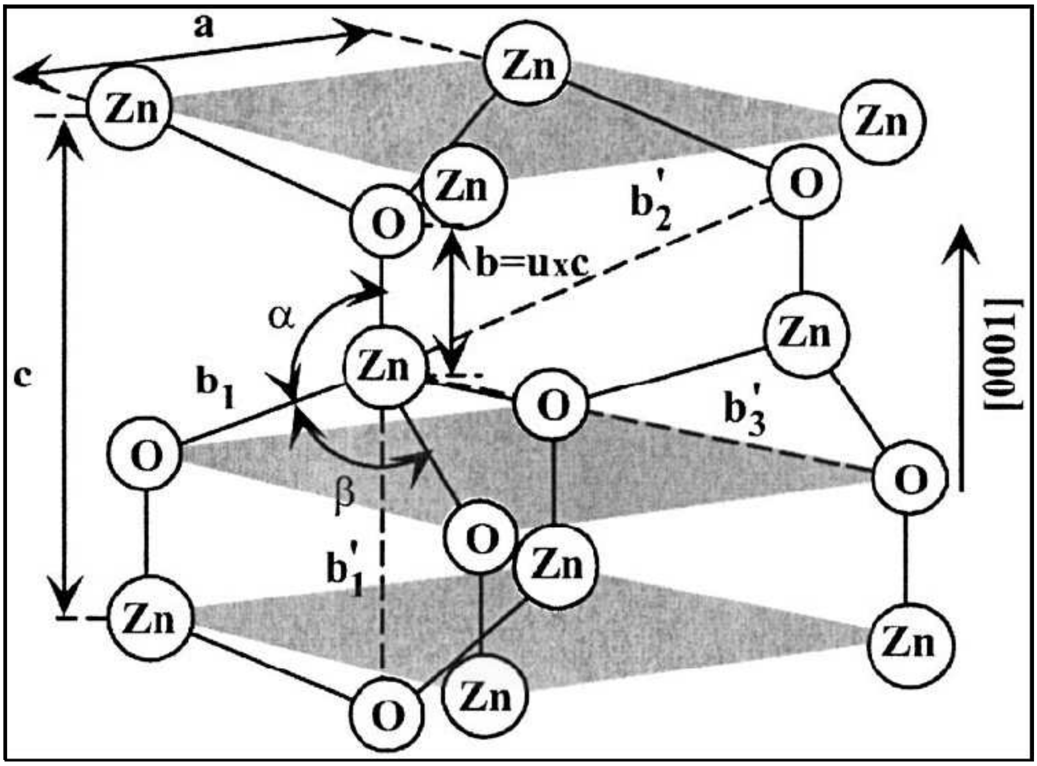

Figure 4.1 Schematic of the structure of the Wurtzite ZnO lattice. The lattice parameters a in the basal plane and c in the basal direction are indicated. The amount by which the two hexagonal close packed lattices are shifted relative to each other is denoted by b [7].

4.1.2 Band Structure

A very important property of any given semiconductor is its band structure, since many important properties such as the bandgap and effective electron and hole masses derive from it [8]. Experimental methods to determine band structure normally involve measurement of UV and X-ray reflection/ absorption/ emission as well as photoelectron spectroscopy (PES) and angular resolved photoelectron spectroscopy (ARPES) [7].

Theoretical calculations of the band structure of wurtzite ZnO have been done with pseudopotential methods, but the agreement with experiment is often only qualitative [7]. An important aspect of the band structure of ZnO is the fact that it has a direct bandgap, which is of importance in laser applications. Recently the band structure of wurtzite ZnO was calculated using an empirical pseudopotential method, as shown in figure 4.2 [9].

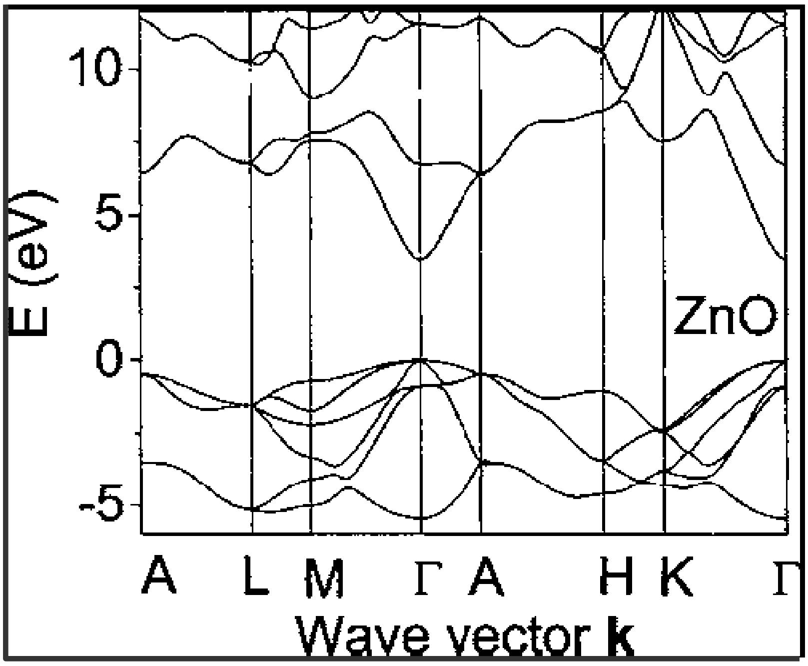

Figure 4.2 Band structure of wurtzite ZnO calculated by an empirical pseudopotential method [9].

4.1.3 Important Material Parameters

As discussed in chapter 3, there are a number of material parameters relating to both band structure and electrical as well as mechanical properties of the lattice which affect the electrical transport of carriers in a material. The material parameters of ZnO used for carrier concentration and mobility data modeling in this study are given in table 4.1. which was taken from Rode [1]. Band structure related parameters are the polaron or density of states effective mass m* and the effective mass energy gap E_g. Lattice-related parameters are the high and low frequency dielectric constants ε_0 and ε_∞, the polar-phonon Debye temperature T_{po}, the longitudinal elastic constant c_l, the intravalley deformation potential E_l and the piezoelectric coupling constant P.

Table 4.1 Important material constants of wurtzite ZnO

Polaron Effective Mass, m*/m	0.318	Polar phonon Debye Temperature T_{po} (K)	837
Effective Mass Energy gap, E_g (eV)	3.43	Longitudinal elastic constant c_l (10^{10} N/m^2)	20.47
Low frequency dielectric constant $\varepsilon_0/\varepsilon$	8.12	Deformation potential E_l (eV)	3.8
High frequency dielectric constant $\varepsilon_\infty/\varepsilon$	3.72	Piezoelectric coupling constant $P_\perp / P_\parallel$	0.21/ 0.36

Some of these parameter values vary slightly depending on the method of determination and temperature [1, 7]. The values quoted in table 4.1 are determined at room temperature (300 K). The piezoelectric coupling constant varies considerably with crystallographic direction. In this study $P\perp$ i.e the value in the plane perpendicular to the *c*-axis was used since this was the plane of current flow in all sample considered. As will be discussed in chapter 7, deformation potential values significantly different from the value cited here were used for transport calculations.

4.2 ELECTRICALLY ACTIVE DEFECTS

4.2.1 Origin of Defects

Two of the main characterization techniques used in conjunction with shallow electrical defects in semiconductor materials are photoluminescence and temperature dependent Hall effect measurements [6, 7, 10].

A host of different shallow donor activation energies in nominally undoped ZnO have been obtained since the inception of electrical research on this material in the 1950's [2, 6, 10, 11] . The wide spectrum of results can be explained by the large number of types of lattice defects and impurities that occur in high purity commercially grown bulk ZnO. Figure 4.3 summarizes the main defect types that can occur in single crystal ZnO, although certainly not all of them are shallow defects [12].

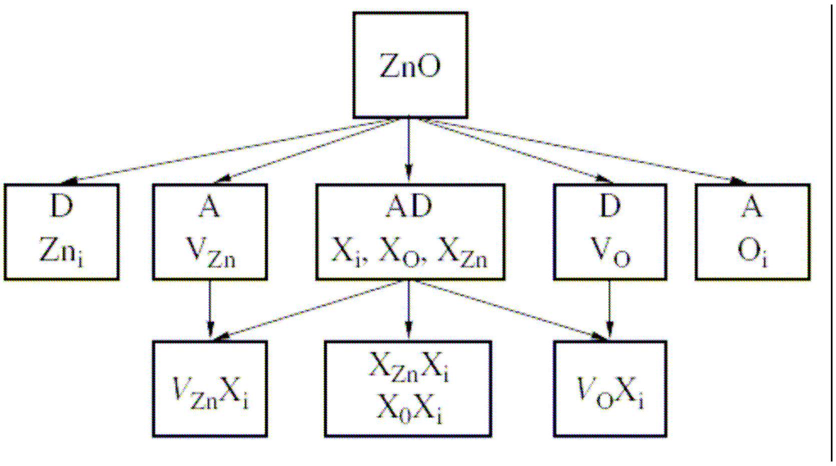

Figure 4.3 Summary of the defect types that may occur in ZnO [12].

Zn_i and V_{Zn} are the zinc interstitial and zinc vacancy respectively while O_i and V_O denote the oxygen interstitial and vacancy respectively. Impurity atoms X can occur either as interstitials X_i or substitutionals X_{Zn} and X_O on zinc and oxygen sites respectively. D and A denote that the relevant impurity is expected to be a donor or acceptor respectively. X does not have to be a foreign atom. A Zn-on-O antisite can for example also occur.

4.2.2 Donors

Of the defects mentioned in figure 4.3, the zinc interstitial Zn_i and the oxygen vacancy V_O have both been associated with donors in the literature, but according to theoretical and electron paramagnetic resonance studies V_O is most likely a deep donor that is unlikely to play an important role in the conduction of low resistivity ZnO [13, 14]. Photoluminescence and temperature dependent Hall studies of electron irradiated ZnO have shown that Zn_i is the most likely candidate for a purely lattice-related shallow donor, and an activation energy of 30-40 meV was obtained for this donor [15]. A donor of 31 meV was however also obtained in unirradiated seeded chemical vapor transport (SCVT)-grown ZnO, but the low concentration obtained puts doubt on the accuracy of the extracted activation energy [10]. In reference [10] this 31 meV donor is in fact not associated with Zn_i, but rather it is speculated that it could be associated with hydrogen. Instead, it is argued that the deeper main donor of activation energy 61 meV also found in this study could possibly be due to native defects, and a result of 51 meV from photoluminescence measurements is cited in this regard [10, 16].

In more recent times, impurities are considered as a likelier candidate for the main donor in nominally undoped ZnO. It is well known that group III elements (Al, Ga, In) on Zn sites act as shallow donors in ZnO. In particular Al_{Zn}, that is aluminium on a zinc site, is a good candidate for the deeper donor [13]. Since Al is a known contaminant in all commercial ZnO growth processes and since it has three valence electrons rather than two in the case of Zn, it seems reasonable to postulate the presence of a hydrogenic donor due to Al with activation energy 66 meV [10]. Evidence of such a donor has also been found in references [6], [10], and [11].

Hydrogen has been mentioned as a shallow donor candidate, and much research has recently and in the past been done on hydrogen in ZnO [17, 18, 19, 20, 21]. Donors with activation energies ranging from 30 meV to more than 50 meV have been associated with proposed interstitial hydrogen and hydrogen-related complexes. A recent study identifies a 39 meV donor in as-grown SCVT ZnO as the main donor, and it is shown that this donor disappears with annealing [11]. Electron paramagnetic resonance experiments combined with annealing supported the postulate that the donor is related to hydrogen. Photoluminescence results in this work did, however, also yield 55 and 59 meV donors that were not confirmed by the Hall measurements.

4.2.3 Acceptors

Acceptors in ZnO can also arise from both lattice defects and impurity atoms. The oxygen interstitial O_i and zinc vacancy V_{Zn} are both thought to be acceptors in ZnO [12]. Positron annihilation spectroscopy measurements indicate that V_{Zn} is the dominant acceptor in intrinsic ZnO [22].

Impurities responsible for shallow acceptor levels in ZnO are group I elements (Li, Na and K) and some monovalent transition elements such as Cu and Ag. These elements are of course only donors if they substitute Zn in the lattice. If they occur on interstitial sites they can actually act as donors [23]. Hydrothermal ZnO often contains significant amounts of group I contamination, and hence it can be semi-insulating. ZnO doped intentionally with Li and Cu has also been investigated [5, 12]. In addition, Group V elements (N, P, As) on oxygen sites are found to act as deep acceptors. Unfortunately for p-conduction these elements have a tendency towards antisite formation, i.e. they can substitute not only oxygen but also zinc atoms, in which case they become donors [23]. Nitrogen appears to be the best group V candidate for p-type doping purposes.

4.3 BULK CRYSTAL GROWTH

A major driving force for the renewed interest in ZnO has been the high quality bulk material that has become available in the last decade [7, 13, 24]. Bulk ZnO is of importance both directly in device applications and as a substrate in gallium nitride epitaxy and homoepitaxial applications [7]. High quality commercial bulk ZnO crystals are grown by three different methods: seeded chemical vapor transport (SCVT), melt growth and hydrothermal growth. These processes will be described briefly in this section.

4.3.1 Seeded Chemical Vapor Transport

The principle of chemical vapor transport growth of ZnO is not new [25]. Recent advances in the method have led to commercial growth of very high quality material [10, 26]. Eagle-Picher Inc. is a company that produces ZnO by the SCVT method. The growth process is as follows [7, 10]: Pure ZnO powder formed by the reaction of zinc with oxygen is placed at one end of a nearly closed horizontal tube. The temperature at this side is held at about 1150 ºC. Although ZnO is ordinarily not volatile at this temperature, H_2 is introduced at this end of the tube to act as a carrier gas. The mechanism is the reaction $ZnO(s) + H_2(g) \rightarrow Zn(g) + H_2O(g)$ which in the forward direction produces water vapor and zinc metal (which is gaseous above 1000 ºC). The zinc and water vapor are carried by the hydrogen to the other end of the tube where the temperature is slightly lower, about 1100 ºC. Here the reverse reaction takes place, and single crystal ZnO forms assisted by a ZnO seed crystal. It is also necessary to add a small amount of water to the reaction to avoid excess zinc in the ZnO crystal. Growth times of 150-175 hours produce crystals of 5 centimeters in diameter and one centimeter thickness. The room temperature and peak mobility of the material are comparable to the best ever achieved for ZnO.

4.3.2 Melt Growth

Melt growth is a relatively new method of growing very large size (up to several kilograms) ingots of high quality single crystal ZnO [27]. The following patented process is implemented by Cermet Inc. in Atlanta, Georgia [7, 27]: Pure ZnO powder is placed in a water-cooled crucible fitted with an RF induction heating coil. The crucible/ induction coil arrangement is located inside a pressure vessel fitted with an inlet pipe for pure oxygen gas. The coil is powered by an RF alternating current source whereby Joule heating of the ZnO powder occurs due to induced eddy currents. The heat thus generated is sufficient to produce temperatures of about 1900 ºC, the melting point of ZnO. Since the ZnO would become depleted of oxygen due to the higher partial pressure of O over Zn at these temperatures it is necessary to supply an overpressure of oxygen in the pressure vessel. Since the crucible is cooled, a thin layer of solid polycrystalline ZnO forms between the melt and the crucible walls, which eliminates containment problems. The melt is thus effectively embedded in a layer that has the same composition as itself, eliminating crucible-induced impurities. The single crystal ingot is drawn by slowly lowering the crucible away from a crystal pulling arrangement. The quality of the material is comparable to that of SCVT-grown material.

4.3.3 Hydrothermal Growth

The hydrothermal growth of ZnO has been known and implemented for a long time. High quality material can also be grown through this process, but relatively high contamination with alkali and other metals is inevitable. Sometimes the concentration of Li and K is high enough to produce semi-insulating material [12]. In this growth system, a Platinum crucible is filled with a mixture of aqueous solutions of KOH and LiOH. Pure sintered rods of ZnO are placed in the solution at the bottom of the crucible while platinum wires with seed crystals are submerged into the solution from the top. The entire crucible is then hermetically sealed by welding and placed in an autoclave. The autoclave is placed in a two-zone furnace so that the bottom of the crucible is slightly hotter than the top (the temperature difference is about 10 ºC, and the process temperature is 300 ºC to 400 ºC). This temperature difference drives a slow erosion of the sintered ZnO at the bottom of the crucible and crystal growth at the top. The growth rate is somewhat anisotropic, but relatively large crystals of 5 cm diameter and more than 1 cm thickness can be achieved [7].

References

---

[1] Rode D.L., Semiconductors and Semimetals Volume 10, Academic Press (1975).

[2] Thomas D.G., Lander J.J., *Hydrogen as a donor in ZnO*, Journal of Chemical Physics 25, 1136 (1956)

[3] Nantu H, Minami T., Takata S., *Zinc Oxide thin film gas sensors with high sensitivity and excellent selectivity*, Journal of Applied Physics 60, 482 (1986)

[4] Wan Q., Li Q.H., Chen Y.J., Wang T.H., *Fabrication and ethanol sensing characteristics of ZnO nanowire gas sensors*, Applied Physics Letters 84, 3654 (2004)

[5] Schmidt O., Geis A., Kiesel P., Van de Walle G., Johnson N.M., Bakin A., Waag A., Döhler G.H., *Analysis of a conducting channel at the native Zinc Oxide surface*, Superlattices and Microstructures 39, 8 (2006)

[6] Look D.C., Mosbacker H.L., Strzhemechny Y.M., Brillson L.J., *Effects of surface conduction on Hall effect measurements in ZnO*, Superlattices and Microstructures 38, 406 (2005)

[7] Ü özgür et al, *A comprehensive review of ZnO materials and devices*, Journal of Applied Physics 98, 41301 (2005)

[8] Sze S.M., *Physics of Semiconductor Devices 2nd Edition*, John Wiley & Sons (1981)

[9] Fan W. J., Xia J. B., Agus P. A.,Tan S. T., Yu S. F., and Sun X. W., *Band parameters of wurtzite ZnO and ZnO/ MgZnO quantum wells*, Journal of Applied Physics 99, 13702 (2006)

[10] Look D.C., Reynolds D.C., Sizelove J.R., Jones R.L., Litton C.W., Cantwell G., Harsch W.C.,*Electrical properties of bulk ZnO*, Solid State Communications 105, 399 (1998)

---

[11] Look D.C., Jones R. L., Sizelove J.R., Garces N.Y., Giles N.C., *The path to ZnO devices: donor and acceptor dynamics*, phys. stat. sol. (a) 195, 171 (2003)

[12] Shaldin Y.V. and Varchulska J., *Effect of Heat Treatment on the Magnetic Properties of Hydrothermally Grown ZnO Crystals,* Inorganic Materials 39, 1052 (2003)

[13] Look D.C., Claflin B., Alivov Ya.I., Park S.J., *The future of ZnO light emitters*, phys. stat. sol. (a) 201, 2203 (2004)

[14] Kasai P.H., Electron spin resonance studies of donors and acceptors in ZnO, Physical Review 130, 989 (1963)

[15] Look D.C., Reynolds D.C., Hemsky J.W., Jones R.L., Sizelove J.R., Production and annealing of electron irradiation damage in ZnO, Applied Physics Letters 75, 811 (1999)

[16] Reynolds D.C., Collins T.C., Excited terminal states of a bound exciton- donor complex in ZnO, Physical Review 185, 1099 (1969)

[17] Gil J.M., Alberto H.V., Vila˜o R.C., Duarte P.J., Ayres de Campos N., Shallow donor muonium states in II-VI semiconductor compounds, Physical Review B 64, 75205 (2001)

[18] Van de Walle C.G., Hydrogen as a cause of doping in Zinc Oxide, Physical Review Letters, 85 1012 (2000)

[19] Seung Yeop Myong, Koeng Su Lim, *Highly stable and textured hydrogenated ZnO thin films***,** Applied Physics Letters 82, 3026 (2003)

[20] Monakhov E.V., Christensen J.S., Maknys K., Svensson B.G., Kuznetsov A.Yu., *Hydrogen implantation into ZnO for* n^+*- layer formation*, Applied Physics Letters 87, 191910 (2005)

[21] Hutson A.R., *Hall effect studies of doped Zinc Oxide single crystals*, Physical Review 108, 222 (1957)

---

[22] Tuomisto F., Vacancy defects in semiconductor materials for opto and spin electronics, Dissertation for doctor of science (2005)

[23] Park C.H., Zhang S.B., Wei Su-Huai, *Origin of p-type doping difficulty in ZnO: The impurity perspective*, Physical Review B 66, 073202 (2002)

[24] Look D.C., *Recent advances in ZnO materials and devices*, Materials Science and Engineering B80, 383 (2001)

[25] Shiloh M., Gutman J., Growth of ZnO single crystals by chemical vapour transport, Journal of Crystal Growth 11, 105 (1971)

[26] Albrecht J.D., Ruden P.P., Limpijumnong S., Lambrecht W.R.L., High field electron transport properties of ZnO, Journal of Applied Physics 86, 6864 (1999)

[27] Reynolds D.C., Litton C.W., Look D.C., Hoelscher C.E., Claflin B., Collins T.C., Nause J., Nemeth B., *High quality melt- grown ZnO single crystals*, Journal of Applied Physics 95, 4802 (2003)

CHAPTER 5

DISCUSSION OF A FULLY AUTOMATED TEMPERATURE DEPENDENT HALL SETUP

Resistivity, carrier concentration and carrier mobility are among the most important properties of semiconductor materials as far as device applications are concerned. Even if these quantities are only measured at a single temperature (e.g. room temperature), much information about the electrical properties of a material can be inferred. It is, however, only in temperature dependent Hall (TDH) measurement of these quantities that material parameters such as shallow donor (or acceptor) concentrations along with their activation energies can be determined by fitting the temperature dependent carrier concentration data [1, 2].

In addition, compensating impurity concentrations may be determined by fitting temperature dependent mobility data to a suitable theoretical model such as the one described in chapter 3. It was shown in chapter 2 that Hall effect measurements can separate conductivity into carrier density and carrier mobility contributions. The measured quantities are, however, not equal to the actual carrier density and drift mobility but differ from these by a factor known as the Hall scattering factor. This factor can, at least approximately, be calculated using equation 3.41. Thus it is clear that TDH measurements can be successfully used to determine the material parameters mentioned.

This chapter is devoted to the discussion of the TDH setup that was assembled for the purpose of the present study. Since TDH measurements require a large number of current and voltage measurements taken at various contact configurations, magnetic field directions and temperatures, it is important, if not essential, that such a process be fully automatic. Details of the specifications of all measurement equipment as well as their computer interfacing and interconnection will be given. In addition the capabilities and limitations of the setup will be discussed.

5.1 DESCRIPTION OF THE SETUP AND ITS COMPONENTS

5.1.1 Overview of the Setup

This section is devoted to a description of the TDH setup used in this study. More detailed information on the individual components and of the setup and practical aspects of measurement will be discussed. The TDH setup was designed and constructed around a few key components that were available. The center piece of any Hall measurement setup is of course a suitable magnet, and our Lab had obtained an old unit made by Oxford Instruments Ltd.

An HP 6030A System power supply was chosen as a current source for this magnet. To obtain a magnetic field of 0.6 Tesla, a current of less than 8 A at a voltage of about 70 V is sufficient, which is well within the capabilities of this power supply. Since the HP 6030A can only apply a voltage in one direction, an inverting switch unit is needed so that the magnetic field can be inverted. A suitable unit was already available prior to commencement of this study, but it had to be modified to enable computer interfacing and improve safety. The safety issue is important since a magnet of this size can store a large amount of energy which will be released as a high voltage, high current arc if for some reason the circuit is suddenly opened while current is flowing through the magnet coils.

To achieve the low temperatures needed for TDH measurements a cryostat by Air Products, powered by a He cycle compressor, was employed. The tip of the cryostat shaft was fitted with a Gold / Chrome (0.07% Fe) thermocouple which in turn was connected to a LakeShore 332 temperature controller. A heating element at the tip of the shaft powered by the temperature controller provides the means for stabilizing the temperature at any setpoint in the 20 K to 370 K range. The cryostat is enclosed with a shroud and a Varian forepump is used to obtain a vacuum. A Leybold-Heraeus Thermovac TM 230 can be connected to the shroud to monitor the vacuum, and values of less than 10^{-3} mbar can be achieved, depending on temperature.

A specialized sample holder was fabricated to enable quick and convenient sample loading. This sample holder can be attached to and removed from the tip of the cryostat shaft and was fitted with an attachment that enables the clipping on of a silicon diode temperature sensor. The additional sensor provides more accurate temperature sensing near the sample than could be provided by the Au/Cr thermocouple, and was also connected to the Lakeshore 332 temperature controller. Electrical contact of the sample to the measurement devices was achieved through a plug on the sample holder.

Two instruments were used to achieve the electrical measurements on the sample: A HP 3245A universal current source and a Agilent 34970A data acquisition unit. The former supplies the current necessary for Hall measurements while the latter is responsible for both creating the contact configurations and measuring the voltage.

All instruments except the magnet switch unit are controlled directly via a GPIB interface. The magnet switch is controlled via a digital output from the data acquisition unit. Automation through the GPIB is controlled by a program written in LabView^{TM}.

5.1.2 Schematics and Circuit Diagrams

5.1.2.1 TDH Setup Schematics and Measurement Circuit

The TDH setup described in section 5.1.1 is represented schematically in figure 5.1. More detailed information on the circuit diagram of the measurement circuit is given in figure 5.2. This diagram shows a schematic representation of the switch matrix in the Agilent 34970A Data Acquisition Unit and how it connects the HP 3245A Current Source and the internal Voltmeter of the Agilent 34970A to the sample contacts. All interconnections between devices as well as between devices and the sample are achieved through the core wire of coaxial cable with the outer sheath being earthed. It can be seen that every contact on the sample can be connected to every Voltmeter or Current source output by activating an appropriate combination of switches in the matrix. Thus all switch configurations needed for Hall measurements that were discussed in chapter 2 can be realized with this setup.

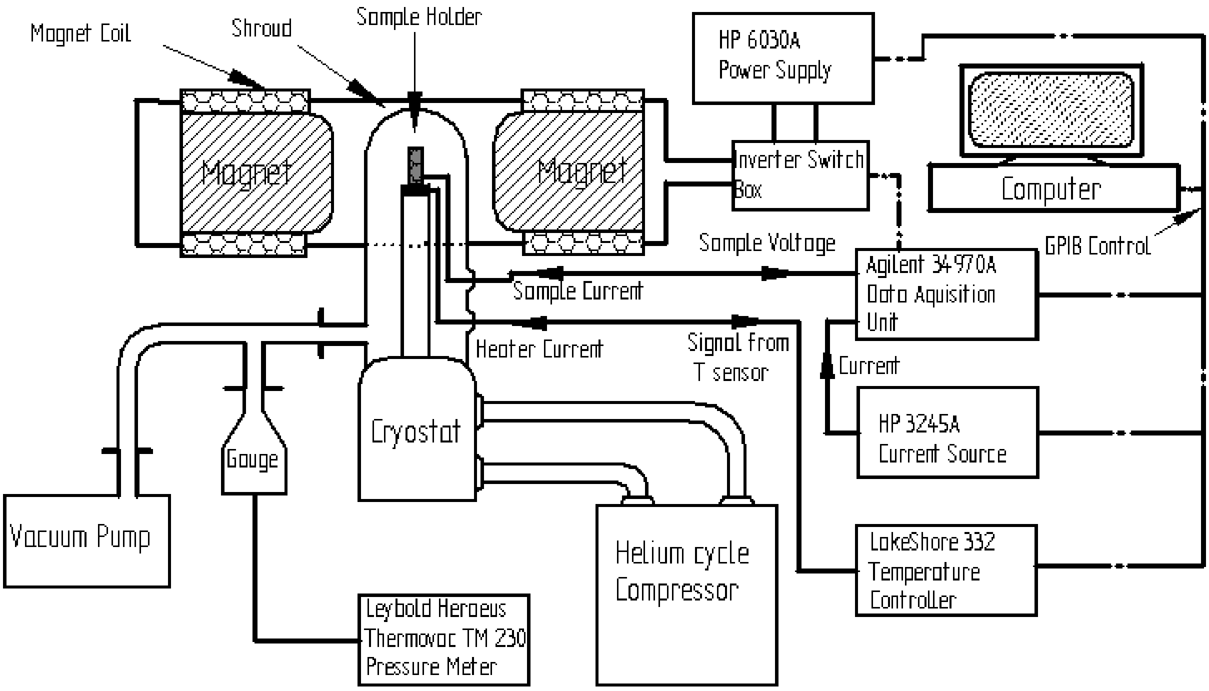

Figure 5.1 Schematic Representation of the Temperature Dependent Hall setup.

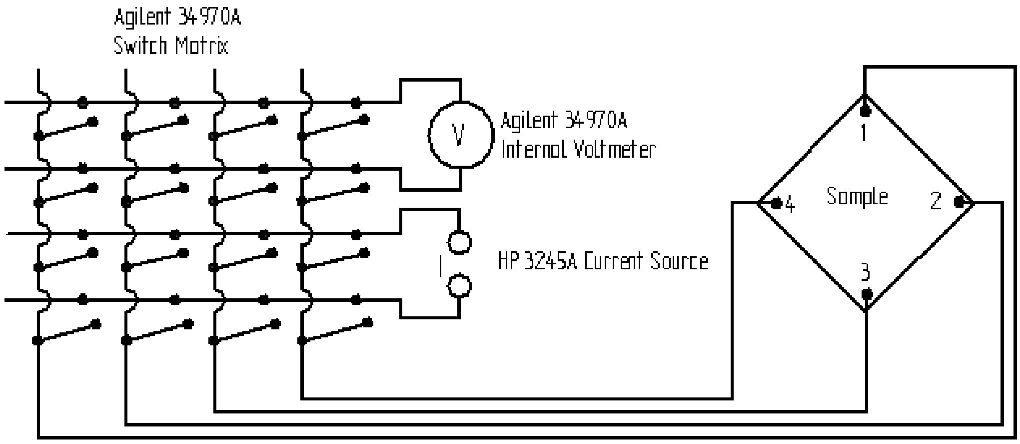

Figure 5.2 Circuit diagram of the measurement part of the TDH setup.

5.1.2.2 Magnet Power Supply Circuit

As already mentioned in section 5.1.1 the HP 6030A power supply can only supply current in one direction. This necessitates the inclusion of a switch unit to invert the polarity. figure 5.3 shows a simplified version of the magnet circuit diagram, including some of the interior workings of the switch box. The current inversion is accomplished by a pair of double latching relays controlled by a computer interfaceable digital circuit.

Protective features include a diode to ensure correct polarity as well as a flyback diode to protect the power supply. Two gas arrestors with a voltage and current rating of 160V and 8A respectively limit damage to the magnet relays and the magnet coils in case of faulty switching of the relays. Good isolation of the digital control circuit from the power circuit is ensured by a pair of solid state relays between these circuits. Feedback from the power circuit to the control circuit (labeled as “safety voltage sensing” in the diagram) prevents any switching action if current is still flowing in the power circuit.

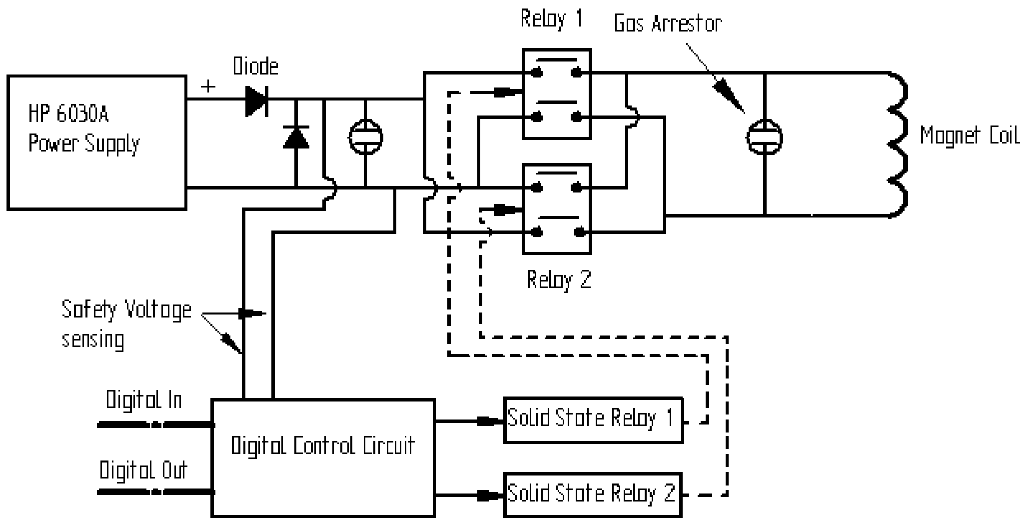

Figure 5.3 Circuit for controlling the magnet current

The control circuit also provides digital output so that the state of the switch unit can be read by the computer program controlling the measurement. Although the switch unit can be controlled directly via the parallel port of a computer, it was decided that the digital output of the Agilent 34970A be used instead so that the system is controlled entirely through GPIB.

5.1.3 Description and Specifications of the Other Components

5.1.3.1 Helium Compressor and Cryostat

A closed helium cycle compressor by APD Cryogenics, model HC-2, was used to power an Air Products displacer-type cryostat. This cryostat caters for the possible mounting of an inner shroud that acts as a shield from radiation due to the outer shroud. Since the custom built sample holder is too large to fit inside inner shrouds available in our lab, another way had to be found to shield the centre shaft. It was found that wrapping the sample holder and part of the cryostat centre shaft in aluminium foil provides sufficient thermal shielding to allow temperatures of about 20 K to be achieved.

5.1.3.2 Vacuum System

The vacuum system of the present TDH setup is quite simple. Its key components are a Varian SD-90 piston pump connected to the cryostat, the shroud that encloses the vacuum chamber and the vacuum monitoring system comprising a Leybold Heraeus (LH) pressure sensor connected to a LH Thermovac TM 230 pressure meter. The shroud fits on the cryostat via a double O-ring seal. When the cryostat is not active, a vacuum of about 10^{-2} mbar is achieved. This value drops to below 10^{-3} mbar at temperatures below about 50 K due to gas freeze-out. It is mainly thanks to this cryogenic pumping effect that a more sophisticated vacuum system is not required in this setup.

5.1.3.3 Hall Magnet and Power Supply

Manufactured by Oxford Instruments Ltd., the trolley mounted magnet features retractable magnet poles and water-cooled magnet coils. The maximum allowable continuous current with water-cooling is rated at 12.5 A, and at 7 A without cooling. Depending on pole separation and the type of poles used, continuous magnetic field strengths of up to 2.6 Tesla can be achieved. In the present setup, 10 cm diameter plane tip poles were used at a separation of 4.4 cm so that the cryostat shroud fits between the poles.

The HP 6030A System Power Supply is used to energize the magnet coils. It is rated at 1000 Watts, and the maximum voltage and current are 200 VDC and 17 A respectively. In the setup used in this study, the power supply is used well below its maximum output: 7.29 A at 70 V so that a magnetic field of 0.600 Tesla is achieved. These values are also below the maximum continuous ratings of the magnet coils, provided that the water cooling is active. The magnetic field strength was measured using a F.W. Bell Model 4048 Gauss/Tesla Meter.

5.1.3.4 Sample Holder

Most Hall measurement setups make use of a system by which four thin wires are soldered directly to the sample. To reduce time and effort expended by sample mounting, a slightly different approach was taken in this study by designing and fabricating a sample holder with four probes, as shown in figure 5.4. The core part of this sample holder, which will be referred to as the table, was machined from a solid beryllium-copper rod. A threaded rod on one side of the table allows for attachment to the cryostat shaft. Four cylindrical pin holders also machined from beryllium-copper mounted on grooves on the table support the four probe pins and allow their positioning. Non-magnetic stainless steel screws at the top of each probe holder allow the needles to be lifted and dropped. The pins are counter-balanced by small springs inside the pin holders. The pin holders are electrically isolated from the table through Teflon washers and shrink sleeving around the attachment screws. It should be noted that it is in general still necessary to fabricate ohmic contacts on the sample rather than simply dropping the probe needles directly onto the material. The ohmic contacts usually consist of soldered-on indium dots on which the needles can be placed.

A spring-loaded attachment at the rear side of the sample surface allows for secure fitting of the temperature sensor (not shown in figure 5.4). A plug on the opposite side of the threaded rod allows for electrical connection of the probes. The probe side of the sample surface can be enclosed by a little shroud made from thin copper sheeting to provide both mechanical and thermal shielding.

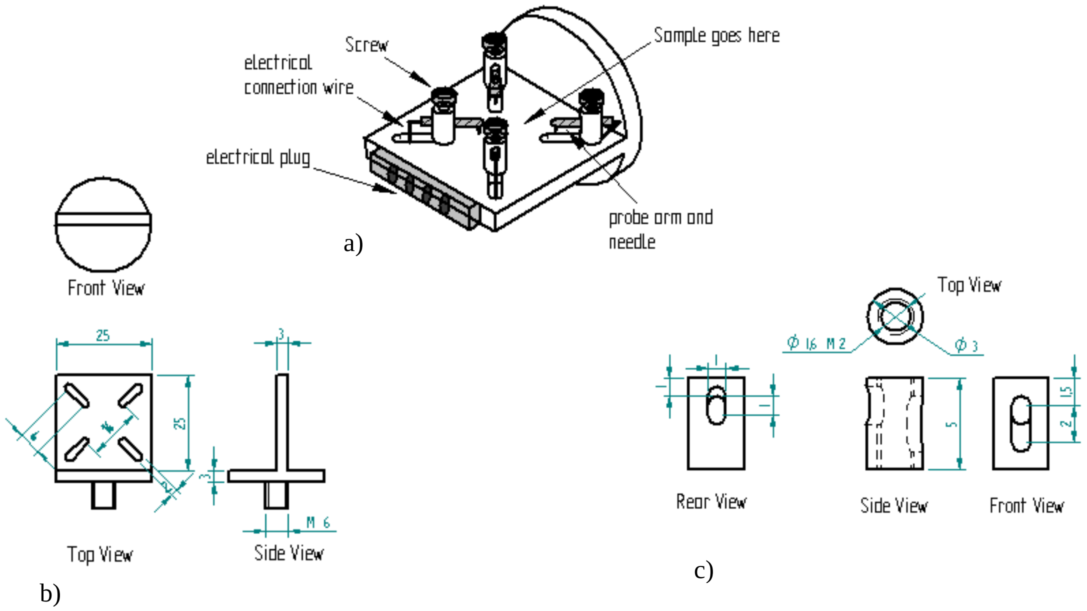

Figure 5.4 Sample holder plans and assembly; a) entire assembly, b) design of the sample table, c) pin holder design

5.1.3.5 Temperature Controller and Temperature Sensors

The LakeShore 332 temperature controller employed in the current setup has two temperature sensor inputs, one for a thermocouple and one for a diode sensor. In the present application both were used. A standard Chromel versus AuFe thermocouple with 0.07% Fe was used for the temperature control circuit. This thermocouple was embedded in indium metal at the tip of the cryostat shaft where the sample holder attachment point is also found. Since the heating element is embedded in the same piece of indium as the thermocouple, very fast and stable temperature control is achieved. The LakeShore 332 temperature controller employs a standard PID (Proportional-Integral-Derivative) control algorithm, and in the present system the P and I values were set quite high (300 and 200 respectively) due to the relatively fast feedback. The D value was set to zero.

Since the temperature at the point of the thermocouple is likely to be somewhat different than the sample temperature and since thermocouples are intrinsically quite inaccurate, it was decided that a dual sensor approach be adopted. A LakeShore DT-470-SD-13 silicon diode sensor was therefore included in the setup. It is mounted on the rear side of the sample holder table, just below the expected sample position, and is therefore more likely to give an accurate temperature value. In addition, diode sensors are more accurate and reliable than thermocouples. This sensor is useful in the 1.4 K to 500 K range, and an accuracy of better than 1 K is specified.

The LakeShore 332 Temperature controller has three power settings: High (50 Watts), Medium (5 Watts) and Low (0.5 Watts). In the present system the High setting is used for temperatures above 40 K while the Medium setting is employed at lower temperatures.

5.1.3.6 Voltmeter

Like most precision voltmeters, the Agilent 34970A's internal voltmeter outputs voltage values averaged over an integer number of power line cycles (PLC's). This considerably reduces noise originating from the 50 Hz mains power cycle.

Table 5.1 Maximum voltage resolution as a function of integration time

Integration Time	Resolution (V/ Range)
1 PLC (0.02 seconds)	0.000003
2 PLC (0.04 seconds)	0.0000022
10 PLC (0.2 seconds)	0.000001
20 PLC (0.4 seconds)	0.0000008
100 PLC (2 seconds)	0.0000003
200 PLC (4 seconds)	0.00000022

The Agilent 34970A allows the user to pre-select both range and resolution of the voltage to be measured. It was found that in so doing more reliable results could be obtained than by letting the voltmeter auto-select the range. There are five voltage ranges available for pre-selection (the values indicate the relevant maximum of the ranges): 100 mV, 1 V, 10 V, 100 V, 300 V. Only the lowest three ranges support a high input impedance of 10 GΩ, while the two highest ranges can only be measured with an input impedance of 10 MΩ. Table 5.1 gives the voltage resolution per unit range (in Volts) as a function of the number of power line cycles used for averaging. In the program written for this study the range and resolution are entered by the user at the start of a TDH measurement.

5.1.3.7 Sample Current Source

The HP 3245A Universal Source can supply both precision voltage and precision current. Only the DC current function was used in this study. There are a number of limitations of this unit that need to be taken into account when using it. The maximum voltage output when applying a specific current is 15 V. If an attempt is made to apply a current requiring a higher voltage, the unit will fail to apply that current without warning the user. Therefore it is important to check the applied voltage when using this device manually or through a computer program.

The current resolution depends on the range. Table 5.2 gives the error in the applied current for a few ranges in high-resolution mode according to specifications.

Table 5.2 Error in the current output of the HP 3245A according to specifications.

Range (A)	± Error
0.00000	3.3 nA
0.00005	5.9 nA
0.0005	46 nA
0.01	0.96 µA
0.1	23.5 µA

It is seen that, if an error of 10% is still acceptable, no current of less than 59 nA should be applied in a measurement. Samples with a resistance of greater than 15 V/5.9×10^{-8} A = 250 MΩ between any set of sample contacts are thus excluded from accurate measurement due to the limitations of this power supply. It is however easy to exchange the current source with a high sensitivity ammeter and voltage source such as the HP 4140B pA meter. This device can measure currents of less than 10^{-12} A and can, in addition, supply voltages of up to 100 V. The highest resistance that could in principle be accurately measured with such a setup is thus 10^{14} Ω. That is not to say of course that Hall measurements can be done on samples of such high resistances since limitations of the voltage measurement capability of the system would almost certainly prevent this. The input impedance of the Agilent 34970A voltmeter, for example, is rated at 10 GΩ, enforcing an upper bound on measurable resistances. One can, however, measure samples of resistances somewhat higher than 250 MΩ using this setup (up to more than 1 GΩ with the present voltmeter). Since only one sample in this study was measured using the HP 4140B voltage source and pA meter, it will not be discussed in detail here.

5.2 DESCRIPTION OF THE AUTOMATED MEASUREMENT PROCESS

5.2.1 Automation Platform

As was already mentioned, it is highly desirable to fully automate a TDH measurement process. Since all the instruments mentioned in section 5.2 have GPIB interfaces, computer control can be achieved readily if a suitable measurement and automation platform is available. The user-friendly and versatile measurement and automation package LabView^{TM} Version 6.1 was used to write programs for TDH automation in this study. The aspect of instrument control in LabView is made even easier by a comprehensive instrument driver library on the National Instruments website www.ni.com. This library contains drivers for virtually every GPIB instrument, and thus it is usually not necessary to write low-level programs to communicate with instruments.

It is important that any experience of good measurement practice, such as that of the author of this thesis, be incorporated into such a program wherever possible. In this section the TDH measurement process will be discussed in some detail, and descriptions as well as flowcharts of the program operation will be supplied.

5.2.2 Practical Considerations of the TDH Measurements

5.2.2.1 Voltmeter/ Switch Unit Control

To enable accurate measurement it is important to configure the Agilent 34970A Voltmeter/ Switch unit in an appropriate way. The first step in this process is to configure this device in "Monitor" mode (rather than "Scan" mode) to enable more precise control over the time intervals between matrix switching and voltage measurement. It is also important to set both range and resolution of the voltmeter to desirable values. From the discussion in section 5.2 it becomes apparent that only the 100 mV, 1 V and 10 V ranges are sensible choices. In the present study the 1 V range was used more than the others. Care must be taken that the selected voltage range is not exceeded.

The choice of voltage resolution is a balancing act between two factors: on the one hand as high as possible a resolution is desired, but on the other hand this requires longer integration times (see Table 5.1). Too long an integration time is often not desirable since this may increase thermomagnetic errors, as discussed in section 2.3.1. In the measurements for the present study, an integration time of 100 PLC was most often used.

Another issue that needs to be considered is the fact that the sample voltage may take some time to stabilize after the switch unit closes the current path. This is especially true for highly resistive samples. The TDH measurement program therefore includes a feature that allows a manually entered delay to occur between applying the current to the sample and measuring the voltage. A delay time of about 5 seconds was usually used.

Thermomagnetic and thermoelectric errors will also increase when the electrical power through the sample, calculated by the product of applied voltage and applied current, is too high. While a high enough voltage is needed for good measurability, too high a voltage could cause undue sample heating. A good rule of thumb is to not allow the electrical power applied to the sample to be much greater than 1 mW, but on the other hand it should also not be too small.

5.2.2.2 Sample Current Control

The choice of excitation current to the sample is of course linked to the desired voltage range. Thus the applied current should be small enough so that the chosen voltage range is not exceeded. Another reason for keeping the current small is again the factor of sample heating, as discussed in the previous section. On the other hand a sufficiently high excitation current is required to produce a measurable Hall voltage. Depending on sample resistance, currents in the entire output range (10^{-8} A to 10^{-1} A) of the Current Source have been used in this study.

TDH measurements pose additional challenges as far as current choice is concerned since the resistance of the sample can change by several orders of magnitude in the 20 K to 370 K range. It is thus necessary to change the applied current and/ or measurement range with temperature. In the present study the voltage range always remained fixed while the current was changed. This can be done either by pre-selecting current values for each temperature or by including a routine in the program that measures the sample resistance at each temperature and adjusts the current value so that no voltage is outside the specified range. Both methods were tried during the course of this study, but the simpler pre-selection method eventually prevailed. The disadvantage of pre-selection is that the sample has to be tested manually at a few sample temperatures in the desired range before a temperature scan is initiated. A subroutine was written to interpolate the sample points so that correct currents may be applied at any temperature in the range. Since many of the samples measured in this study had roughly the same electrical resistance as a function of temperature, this procedure of taking sample points before a measurement was not necessary for each individual case. It is in any case often advantageous to get a “feel” for the temperature behavior of the sample before an automated measurement is undertaken.

5.2.2.3 Temperature Control

Due to fast temperature feedback in the present system, parameters such as heater range and PID control parameters are not critical (see section 5.1.3.5.). One issue that needs consideration is the time the system has to wait for the temperature to stabilize. Since the sample is thermally not as tightly coupled to the system as the temperature sensors, it makes sense to introduce a large delay time to elapse after temperature convergence until measurements are taken. It was found that a delay time of 10 to 15 minutes is sufficient, depending amongst others on the temperature range.

5.2.2.4 Magnetic Field Control

Due to the large inductive reactance of the magnet, it is not a good idea to instantly command the HP 6030A Power Supply to apply the desired current, as this would put undue strain on this device. Therefore a routine was written to ramp up the current in increments of 0.01 A until the setpoint of 7.29 A is reached. The ramping procedure takes about 10 seconds. The changing magnetic field as the magnet current is ramped up or down induces an electric field that destabilizes the thermocouple reading momentarily. This leads to small but noticeable destabilizing effect on the temperature reading. For this reason it is advisable to include a delay time between the moment at which the magnetic field stabilizes and the moment at which measurements commence. Usually a delay of about one to two minutes was used for the purposes of this study.

5.2.3 Sequence of Program Operation

Before running the program, input parameters have to be given. These include the temperature range and increment, sample point currents at different temperatures, voltmeter range and resolution, delay settings and sample details such as thickness, sample description and the path for saving the data. Once the inputs have been made the program can be started, and the following sequence is executed:

1) *Configure Temperature controller to desired settings (including PID parameter settings etc.)*
2) *Set next temperature value*
3) *Read temperature continually until the value is within 0.5 K of the setpoint*
4) *Wait for specified time*
5) *Configure Voltmeter / Switch unit to desired settings (including range and resolution of the voltmeter)*
6) *Configure Current source to desired settings*
7) *Perform the 8 resistivity measurements by applying the desired current and setting the matrix switch to the appropriate configurations (see chapter 2).*
8) *Calculate resistivity and add to output data array*
9) *Configure magnet power supply*
10) *Check magnet switch status and switch to desired direction.*
11) *Ramp up current to desired value*
12) *Wait for specified time*
13) *Perform the 4 Hall measurements by applying the desired current and setting the matrix switch to the appropriate configurations (see chapter 2).*
14) *Ramp down magnet*
15) *Go to step 10 and repeat for the other switch direction*
16) *Calculate mobility and carrier density and add to output data array*
17) *If current temperature setpoint is the final one, save data. Else go back to step 1 and repeat with the next setpoint.*

The data is continually updated on the screen through plots and tables, so that it can be viewed throughout the measurement process.

References

[1] Look, D.C., *Electrical Characterisation of GaAs Materials And Devices*, John Wiley & Sons, New York, 1989

[2] D.C. Look, *Methods in Materials Research* 5a.2.1- 5a.2.8 Wiley, New York, 15 May 1998

CHAPTER 6

EXPERIMENTAL PROCEDURE AND DATA ANALYSIS

The foundation required for performing TDH measurement and analysis has been laid in chapters 2, 3 and 5. In chapter 2, basic Hall theory was discussed and it was shown how the quantities of interest, namely carrier concentration, mobility and resistivity, may be obtained from a series of current and voltage measurements. Chapter 3 was devoted to providing a theoretical framework for describing the temperature dependence of carrier concentration and carrier mobility, in particular adaptations of the theory that can be applied to ZnO. The properties and growth methods of this material were described in chapter 4 with emphasis on shallow electrical defects. In chapter 5 the implementation of the temperature dependent Hall (TDH) setup used in this study was described in some detail.

The present chapter is devoted to the description of the TDH measurement and data analysis process performed for different types of bulk ZnO. On the experimental side, bulk ZnO samples grown by different methods are compared. In addition, annealing studies were done by measuring samples subjected to annealing temperatures in the 200 ºC to 950 ºC range in an argon atmosphere. Proton irradiated as-manufactured and annealed layers on semi-insulating (SI) ZnO were also investigated with the TDH technique. Details of sample sizes, geometries, cleaning procedures, sample mounting in the Hall setup and annealing conditions will be given. The process of analyzing the Hall data will also be described in some detail in this chapter. Schematic descriptions of the computerized numerical routines used to fit the mobility and carrier concentration data will be given and the entire process of extracting defect concentrations and activation energies will be outlined. Difficulties in obtaining a good fit and extracting parameter values will be highlighted and methods will be presented to overcome these difficulties.

6.1 EXPERIMENTAL DETAIL

6.1.1 Sample Preparation

It is usually not difficult to prepare samples for Hall measurement. No special cleaning procedure is required prior to fabricating the four contacts. All ZnO samples measured in this study were square or near-square rectangular in shape. These geometries were achieved by cleaving the original wafers using a diamond tip scribe. Sample sizes ranged from 3×3 mm^2 to 6×6 mm^2.

Ohmic contacts to the samples were fabricated in the following way: A soldering iron was fitted with a custom machined pure nickel tip, and a soldering iron temperature of approximately 250 ºC was set. A special Indium-Tin alloy was smeared onto a glass microscope slide with the hot soldering iron. This measure improves the bonding of the solder to the semiconductor material, probably due to the sodium content of the glass acting as a flux. Contacts of as small a size as possible were then made by smearing small amounts of solder onto the four corners of the sample under a microscope. Once the contacts were made, the sample was placed on the sample holder table (see section 5.2.3.4) and the four probe needles were securely dropped on each contact. After attachment of the protective cover, the sample holder was mounted in the Hall setup and was wrapped in a piece of aluminium foil for thermal isolation. After placement of the shroud, and activation of the vacuum system and Helium compressor, the sample was ready for variable temperature Hall measurement. Before commencement of a measurement the contacts were individually checked with a computer program designed for this purpose. A manual scan through the temperature range was done for some samples in order to find suitable excitation current values for the program to apply. With some exceptions, the samples were measured in the 20 K to 330 K range.

6.1.2 Sample Annealing

Samples of all different types of ZnO studied were annealed at various temperatures in an Argon atmosphere. A Lindberg Hevi-Duty tube furnace was used for all annealing experiments. Samples of melt-grown ZnO, of which an abundant supply was available, were annealed at temperatures in the 550 ºC to 950 ºC. Hydrothermally grown semi-insulating ZnO samples were also annealed up to 950 ºC. Only one sample of seeded chemical vapor transport (SCVT) grown ZnO was available, and it was annealed at temperatures from 550 ºC to 950 ºC. Samples with the implanted hydrogen layer were annealed in the temperature range 200 ºC to 400 ºC.

6.1.3 Sample Cleaning

In some cases the same sample was alternately annealed and measured for different annealing temperatures. This requires complete removal of the contacts used for the previous measurement as the Indium may diffuse into the sample at high temperatures, changing its electrical properties. After thoroughly scratching off the contacts with a scalpel, the following cleaning procedure was employed:

1) 5 minute rinse in acetone (analytic grade) in an ultrasonic bath
2) 5 minute rinse in methanol (analytic grade) in ultrasonic bath
3) drying of the sample with pure N_2 flow

After this procedure the sample is ready for another annealing cycle.

6.2 DATA ANALYSIS

6.2.1 Data Inspection and Two-Layer Correction

Once the experimental TDH data has been obtained there are a number of deductions that can be made immediately by inspection. In particular, it is usually possible to tell whether the semiconductor sample is degenerate, non-degenerate or a combination of these (e.g. a degenerate surface or interface layer on a non-degenerate bulk sample). Typical mobility and carrier concentration profiles of these three cases are given in figure 6.1. Roughly constant mobility and (high) carrier density temperature profiles suggest that degenerate material is present, while a carrier density profile that decreases monotonically in a pseudo-exponential fashion with reciprocal temperature indicates the presence of non-degenerate material. An initial drop in the *n* versus 1/*T* plot followed by an apparent increase and eventual flattening out of the graph for high 1/*T* (low *T*) suggests that two different layers are present, one of which is degenerate. In such a case it is worthwhile to attempt a two-layer correction of the data before doing a theoretical fit. Such a correction can only be done accurately if both the mobility and carrier concentration data flatten out asymptotically at low temperatures (see section 2.4.2.2). Even if the data is not observed to flatten out, it can sometimes be useful to estimate the asymptotic conversion value to allow some correction. The two-layer correction procedure is also described in references [1] and [2].

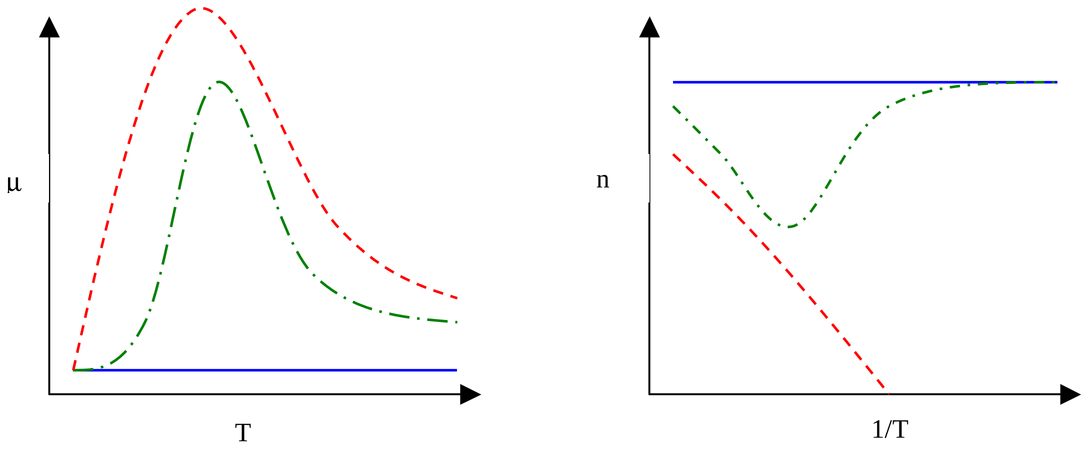

Hall mobility versus temperature

Hall carrier concentration versus reciprocal temperature

Figure 6.1 Idealized Hall mobility and carrier concentration profiles for purely non-degenerate conduction (red dashed line), degenerate conduction (solid blue line) and combined two-layer conduction (green alternate dash-dot line) in ZnO.

6.2.2 Data Fitting Algorithms

6.2.2.1 Software and Regression Routines

In choosing a platform for writing programs for the regression of Hall mobility and carrier concentration data, essentially two aspects were considered: simplicity and efficiency. The computational package MATLAB was chosen for the computations and regressions performed in this study. A compromise between ease of use (simplicity) and computation time (efficiency) is reached through the use of this package. MATLAB has several built-in nonlinear regression functions that can be used to fit nonlinear functions. Due to ease of use and robustness, it was decided that a built-in implementation of the Nelder-Mead simplex algorithm, named “fminsearch”, be used for fitting both carrier density and mobility data. This algorithm is an unconstrained local minimizer of a given multi-parameter input function with respect to a set of starting values. Functions to calculate the error in the least squares sense between the Hall data and the predicted values were written so that the minimizing routine *fminsearch* could be used. More details of application to carrier density and mobility data are given in the following sections.

At a lower level, numerical solving and integration routines had to be used. The built-in function *fzero* was used for purposes of numerical equation solving while a simple program based on Simpson’s rule was written to handle all integrations. This program is non-adaptive and non-recursive, i.e. the integration region is divided evenly into sections the number of which is pre-determined by the user. Although such a routine is robust and fast, it does not have a means of checking whether the result of the integration is accurate. It is therefore crucial that the user provide correct integration limits and a sufficiently large number of sub-intervals. Throughout the course of this study, very little change of these values was required, since the same material was used throughout (Zinc Oxide). It is, however, advisable to check for integration accuracy if the mobility data of a different material is to be fitted as this may change the required integration limits and number of sub-intervals.

Nonlinear regression of Hall data as implemented in this study is a computationally expensive process. This is particularly true in the case of mobility data fitting, but even the regression of a set of carrier concentration data can take several minutes. It is therefore important to find as many computational shortcuts as possible. One way of considerably reducing evaluation time in MATLAB is through a process called vectorization. Vectorization is basically the evaluation of a function by supplying it with an entire array at a time instead of looping the calculation of the function with single number input at a time. Not all types of functions allow for vectorization, however. The built-in numerical solver *fzero* in MATLAB, for instance, only accepts single number input. The mobility and Hall scattering factor evaluation routines written for this study allow for vectorization with respect to the temperature parameter, despite the fact that the *fzero* function is used in these programs. The reason for this is that temperature does not enter into any numerical solving components of the programs. Roughly speaking, vectorization shortens the total computation time by a factor *n*, where *n* is the number of data points used in the regression, since the most time consuming numerical solving routines are only executed once for each set of temperature data instead of re-executing them for each value of temperature. In the present study *n* was usually about 40 to 50. Good coding can thus make the difference between minutes and hours of computation time. The following sections give more detail on the regression method and procedure.

6.2.2.2 Details of Mobility Data Regression

The mobility regression program consists of a number of nested loops. Calculations are based on the results of section 3.2. At the lowest level, the perturbation distribution *g* is evaluated both in the relaxation time approximation and exactly using Rode's iterative technique, as described in section 3.2. Results of the exact *g* computations (equation 3.29) are used by the numerical integration program to evaluate the mobility. The Hall scattering factor is then calculated via equation 3.41 in a separate integration using the relaxation time perturbation distribution (see section 3.2.2 and equation 3.30). The theoretical Hall mobility $\mu_H=\mu_d\times r_H$ with μ_d the theoretical drift mobility calculated using equation 3.31 and r_H, the Hall scattering factor, is then calculated for the purposes of fitting the experimental data. In the present implementation the limits of all integrations were 0 to 1.2×10^9 m^{-1} in *k*-space, and the number of subintervals was 50.

A program that evaluates the least squares difference between the mobility data and the predicted value was fed into the Nelder-Mead simplex algorithm. Unfortunately it turns out that a simple least squares optimization using the acceptor concentration N_A and the deformation potential E_l as fitting parameters often does not yield a satisfactory result. What is meant by "not satisfactory" is that the "best" fit in the purely least squares sense often does not fit the data well in the low temperature regime, the predicted mobility actually being lower than the experimental data in this temperature region. Such a fit, using the example of Hall mobility data from a sample of seeded chemical vapor transport (SCVT) grown ZnO, is shown in figure 6.2 a). There are two reasons why the fit shown in figure 6.2 a) may be deemed less than satisfactory:

1) The low temperature data is more sensitive to the acceptor concentration N_A than the high temperature data. Since N_A is the main parameter of interest, it is more important to get a good low temperature fit. This is not the case in figure 6.2 a).

2) It is more likely that the experimental Hall mobility is *lower* than the predicted mobility rather than being significantly higher (in the low temperature region) as shown in figure 6.2 a). The reason for this is that a real crystal is likely to have additional scattering mechanisms not included in the present model.

To overcome these problems while still retaining a consistent data analysis scheme one may decide on a "modified" least squares fit, the result of which is shown in figure 6.2 b). Instead of simply using the square of the difference between data and fit to calculate the error, two cases are distinguished: 1) If a data point is below (smaller mobility value) the predicted (fit) value, the error e is calculated in the usual way with $e = (\mu_d - \mu_p)^2$ where μ_d is the mobility of the data point and μ_p the predicted mobility. 2) If a data point is above the predicted value, the error e_F is given by $e_F = F\times(\mu_d - \mu_p)^2$ where $F > 1$, i.e. a certain "penalty" is introduced for fitting below the data. Figure 6.2 b) shows such a modified fit with $F = 10$. The fitted mobility at the peak around 100 K is still slightly lower than the data, and the high temperature fit is slightly worse. This fit does, however, seem to represent the overall trend of the data much better and a much more satisfactory low temperature fit is obtained. The "modified" least squares procedure was used to fit all mobility data in the present study (see chapter 7).

Figure 6.3 summarizes the operation of the regression program. In the present implementation the user is given the option of choosing as a fitting parameter either the acceptor concentration N_A only or both N_A and the deformation potential E_l. The latter should actually not be a fitting parameter since the deformation potential is a material constant, but it can be used, in some sense, to account for deficiencies in the model.

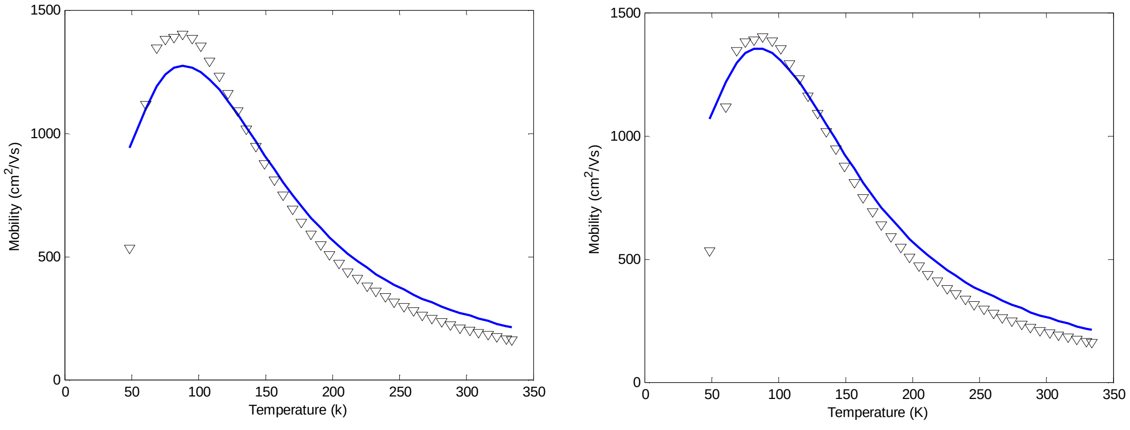

a) b)

Figure 6.2 Comparison of two types of least squares mobility fits on a typical data set. Part a) shows a simple least squares fit which resulted in N_A= 8.3×10^{15} cm^{-3}, E_l = 10.8 eV and an error of 9.2. Part b) shows a modified least squares fit with F = 10, N_A = 7.1×10^{15} cm^{-3}, E_l = 10.4 eV and an error of 11.9.

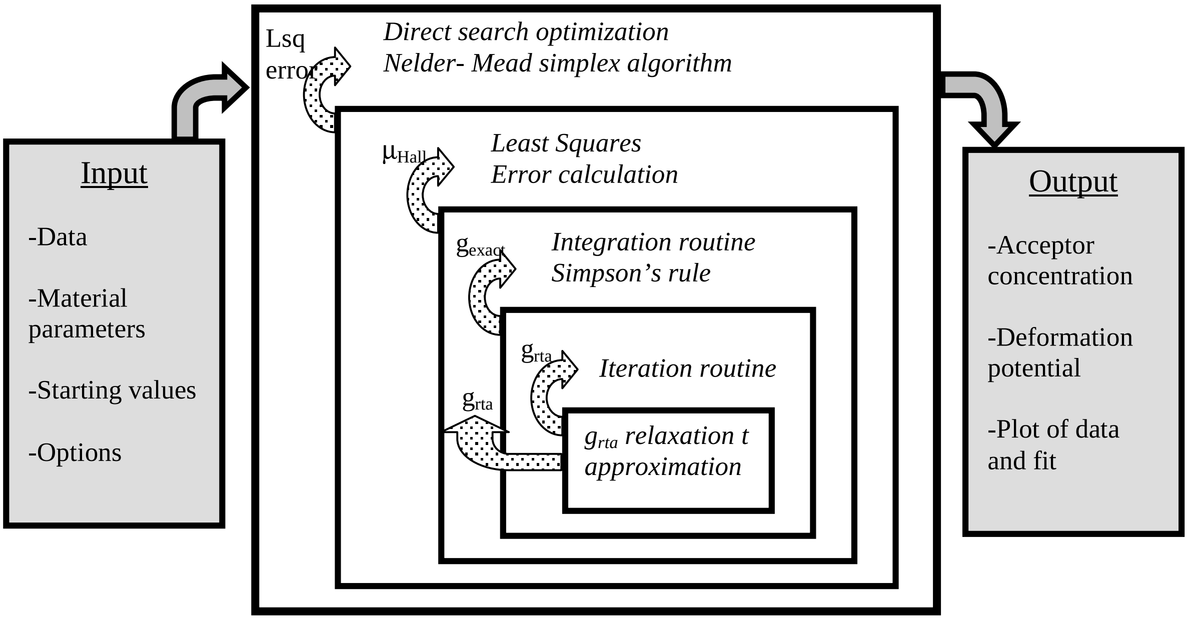

Figure 6.3 Summary of the Hall mobility regression program.

6.2.2.3 Details of carrier concentration data regression

Carrier concentration data regression is computationally somewhat less expensive than its mobility counterpart since the evaluation carrier concentration requires only a numerical solution of the charge balance equation (CBE), see equation 3.18. It is, on the other hand, more important to get a really good fit here since a much larger number of parameters are extracted from the carrier concentration data than from the mobility data. The *fzero* function in MATLAB was used for evaluating the carrier concentration using equation 3.18, and the least squares difference of data and fit had to be calculated in a point-by-point fashion since vectorization is not possible here. Before fitting, the Hall carrier concentration data was corrected through multiplication by the Temperature dependent Hall scattering factor $r_H(T)$. Since $r_H(T)$ also depends on the true carrier concentration $n(T) = n_H(T)r_H(T)$, an iterative approach can be employed to find a more accurate value for $r_H(T)$. As a first approximation, $n_H(T)$ is used to find $r_H(T)$ so that a first approximate correction can be made. Substitution of the corrected carrier concentration data into the scattering factor calculation algorithm yields a more accurate estimate for the scattering factor $r_H(T)$. More iterations can be done, but the added accuracy may not be worth the extra computation time needed.

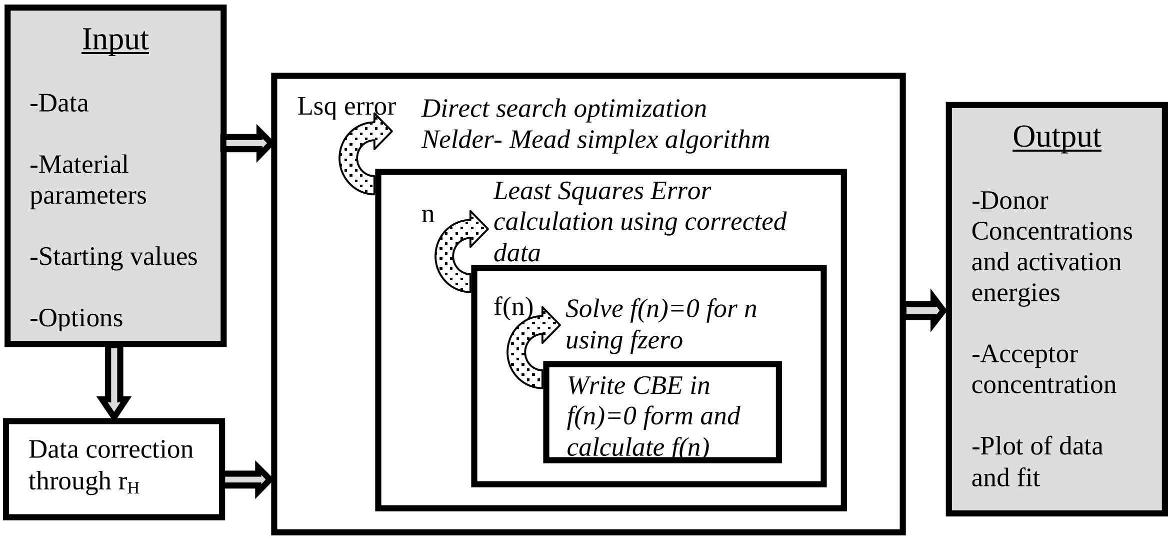

Figure 6.4 Summary of the carrier concentration regression program

Several types of charge balance equations were included as options in the current implementation. One, two or three donor levels can be assumed. Additional options with each of these choices are whether to fit or fix the acceptor concentration (e.g. if N_A is taken from the mobility fit) and whether or not to include the possibility of very shallow donor levels ($E_D = 0$) [3]. The latter only makes sense if N_A is known already since the inclusion of arbitrarily shallow donors in the model is mathematically equivalent to the presence of a negative acceptor concentration (see section 3.1.2). Figure 6.4 summarizes the carrier concentration regression process.

6.2.2.4 Procedure for a complete Hall data analysis

The aim of this section is to describe the process of extracting material parameters from TDH data employed during this study. Before any fitting was attempted, inspection of the data revealed whether or not a two-layer correction is necessary. Such a correction was done on both the carrier density and mobility data if required. The next step was to get a good mobility data fit so that the acceptor concentration N_A could be obtained. Since the variation of N_A alone could usually not produce a satisfactory fit, the deformation potential E_l was usually used as a fitting parameter as well [4]. Care was taken that the low temperature fit be as good as possible since this is the region that is most affected by the parameter N_A. The procedure for the mobility data fit was as described in section 3.2.2.3.

Once a satisfactory fit was obtained for the mobility data the carrier concentration data was considered. First, a decision had to be made as to what type of model was to be used (e.g. whether to use a two-donor or a single donor model). Usually the acceptor concentration was not used as a fitting parameter in the carrier concentration data regression but was taken directly from the mobility data fit [1, 2]. The Hall scattering factor used to correct the carrier density data was calculated using N_A and E_l values obtained from the mobility fit. After suitable starting values for the regression parameters were entered, the program could be started. Several different carrier concentration models were used for some sets of data and were compared according to how good the respective fits obtained were.

References

[1] Look, D.C., *Electrical Characterisation of GaAs Materials And Devices*, John Wiley & Sons, New York, 1989

[2] D.C. Look, *Methods in Materials Research* 5a.2.1- 5a.2.8 (Wiley, New York, 2000), 15 May 1998

[3] Look D. C., Jones R. L., Sizelove J. R., Garces N. Y., Giles N. C., *The path to ZnO devices: donor and acceptor dynamics*, phys. stat. sol. (a), 195, 171 (2003)

[4] Look D.C., Reynolds D.C., Sizelove J.R., Jones R.L., Litton C.W., Cantwell G., Harsch W.C., *Electrical properties of bulk ZnO*, Solid State Communications, 105, 399 (1998)

CHAPTER 7

RESULTS AND DISCUSSION

This section contains a selection of results obtained from measuring as-grown, annealed as well as implanted ZnO samples. The results are categorized according to sample growth method (or treatment method in the case of implanted samples). Although definite differences between samples grown by different methods and annealed at different temperatures can be observed, it turns out that it is often difficult to unambiguously determine all parameters of interest for a given sample. In particular, it is often not possible to find the activation energy and concentration of a minor donor species (a donor with a relatively low concentration) in the presence of a dominant donor with any degree of confidence. Additional techniques such as photoluminescence (PL) or electron paramagnetic resonance (EPR) can be of great value here, but these techniques were not utilized in the present study, the focus being Hall measurements alone [1, 2]. Results of Hall effect studies on material grown by all three commercial methods (see chapter 4) have appeared in the literature, and the present results will be compared to these [1, 2, 3, 4].

All types of ZnO considered in this study showed changes under annealing to a greater or lesser degree. The results will be compared to published Hall effect studies of annealed ZnO [1, 5, 6]. An interesting aspect of the results both in this study and in the literature is the observed change in the surface conduction of certain types of bulk ZnO at annealing temperatures above 500 °C under inert atmospheres [5, 7]. A large part of the discussion will be devoted to this interesting phenomenon that occurred in hydrothermally grown and SCVT grown ZnO, but not in the melt-grown and implanted samples.

Hall effect studies of hydrogen implanted ZnO date back to the 1950’s, but the nature of hydrogen induced defects in ZnO remains controversial [8]. Recent proton-implantation experiments combined with electrical measurements have been published, but the focus has been on thermally stable implant isolation and n^+-layer formation rather than fundamental investigation of the H-related donor [9, 10, 11]. The results from the H-implanted layers considered in the present study are interesting especially when compared to results from the bulk material.

7.1 COMPARISON OF AS-GROWN BULK ZnO GROWN BY DIFFERENT METHODS

7.1.1 Comparison of the As-Measured Data

Samples produced by the three main growth methods in commercial use today, namely melt-growth (Cermet Inc.), seeded chemical vapor transport (SCVT) growth (Eagle-Picher) and hydrothermal growth, were measured in the temperature dependent Hall (TDH) setup. The mobility and carrier concentration results are plotted in figures 7.1. and 7.2 respectively.

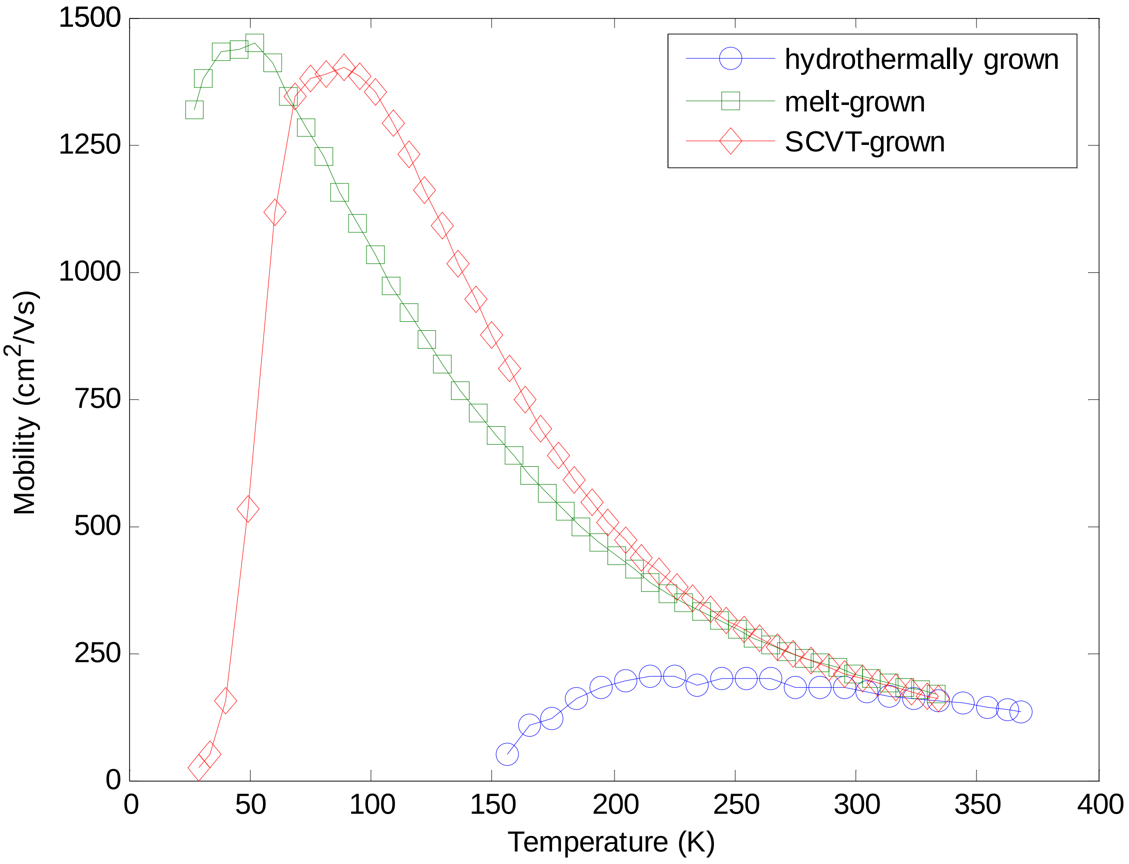

Figure 7.1 Hall mobility as a function of temperature for different types of bulk as-grown ZnO

It is seen that the peak mobilities and carrier concentrations of the melt-grown material and the SCVT-grown sample are quite similar. Differences do, however, exist in the position of the mobility peak and the slope of the carrier concentration graphs. The peak mobilities are lower than the highest reported in the literature, but the author is not aware of higher peak and room temperature mobilities published for melt-grown material [1, 2, 4]. A more detailed analysis of the data will reveal how these differences translate into differences of shallow defect parameters and the influence of surface conduction channels. The hydrothermal ZnO measured here is semi-insulating (SI), and therefore has quite different electrical properties than the other two samples. Similar TDH results are given in reference [3]. An analysis of the data will show that the reason for the low carrier density and mobility is caused by both a high acceptor concentration and a high apparent donor activation energy.

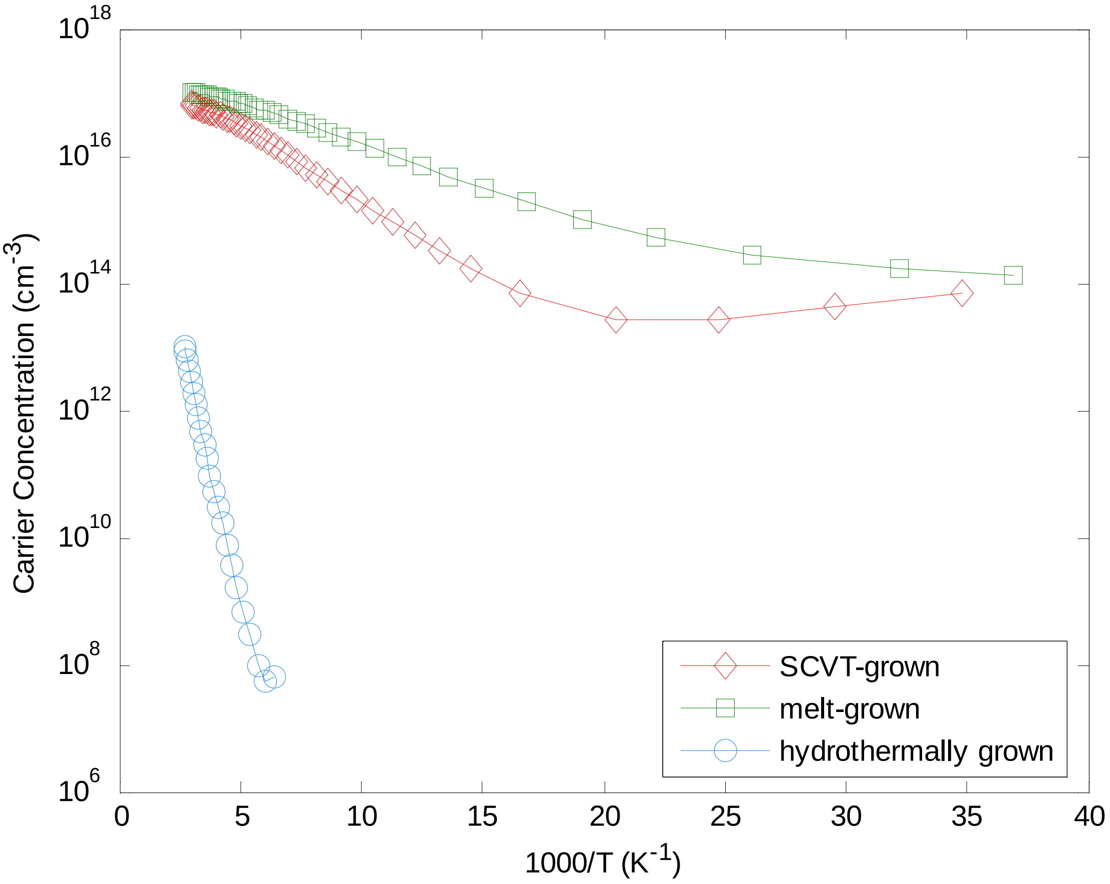

Figure 7.2 Carrier concentration as a function of reciprocal temperature for different types of bulk as-grown ZnO.

7.1.2 Analysis of the Melt-Grown Data

Inspection of the data reveals that there is probably no significant surface conduction present in this sample since the carrier concentration decreases monotonically with temperature throughout. The mobility data is also not observed to flatten out in the very low temperature regime. Therefore it does not make sense to attempt a two-layer correction in this case, and the data was fitted directly.

For the mobility fit it was decided to use the deformation potential E_l as a fitting parameter instead of using the value from literature since this resulted in a much better fit (see also reference [2]). To prevent the fit from underestimating the mobility, a “modified” least squares fit as described in detail in section 6.3.2.2 with a “penalty” factor $F = 10$ was used. For the carrier concentration data a three-donor model resulted in a good fit. The acceptor concentration from the mobility fit was used as a fixed parameter in the regression.

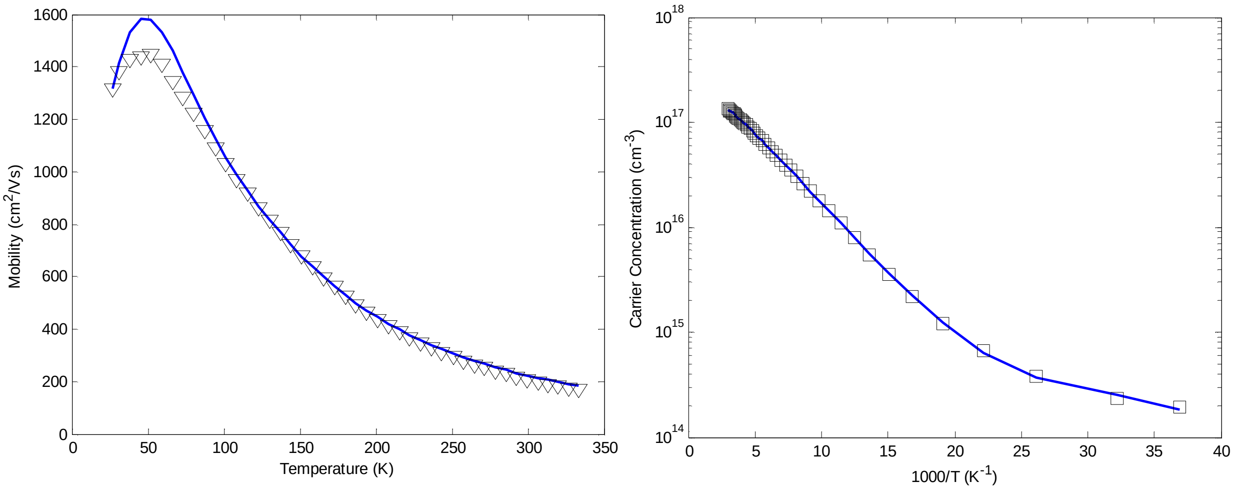

Figure 7.3 Mobility and Carrier concentration data (triangles and squares) with fits (solid lines) of unannealed melt-grown ZnO. Parameter values: $N_A = 3.34\times10^{15}$ cm^{-3}, E_l=15.5 eV, $N_{D1} = 5.32\times10^{16}$ cm^{-3}, E_{D1}=66.7 meV, $N_{D2} = 1.18\times10^{17}$ cm^{-3}, E_{D2}= 43.7 meV, $N_{D3} = 3.77\times10^{15}$ cm^{-3}, E_{D3}=7.2 meV.

Plots of the data regressions are given in figure 7.3 and the extracted parameters are given below the graphs. The concentration of the very shallow donor D3 with activation energy 7.2 meV is very close to the acceptor concentration N_A. There are two dominant donors D1 and D2 according to this analysis, with activation energies of about 67 meV and 44 meV respectively. A relatively large value of 15.5 eV was obtained for the deformation potential so that the high temperature data is also well fitted. The activation energy of D1 appears to be very sensitive with respect to the other parameters. A slight change in some other parameters for example yields an activation energy of 74 meV without the fit becoming worse. The value of 67 meV is favored here since it is closer to the expected hydrogenic value of 66 meV [2].

7.1.3 Analysis of the SCVT-Grown Sample

From the SCVT data in figure 7.2, it is seen that surface conduction plays a significant role in this sample. Correction of the data via the two-layer model is therefore necessary, but unfortunately neither the carrier concentration nor the mobility data is observed to flatten out in the low temperature regime. In Section 7.2.2 an attempt is made at correcting the data, but here the low temperature data will simply be ignored so that the surface channel conduction may be neglected. As is seen from the correction attempt in figure 7.10, the data for 1000/T values less than about 15 can be considered independent of surface channel conduction. The data for temperatures above 66 K was therefore fitted, and the results can be seen in figure 7.4. A two-donor model was chosen for the carrier concentration data fit since a three-donor model could not be successfully applied.

The mobility fit was once again performed using the “modified” least squares procedure with F =10 as described in section 6.3.2.2. One can see that the deformation potential E_l is somewhat lower than that obtained in the melt-grown mobility fit. A donor with activation energy in the 70 meV range seems to be common to both melt-grown and SCVT-grown samples although its activation energy is slightly higher (almost 80 meV) in the SCVT-grown sample. No donor in the 40 meV range was found in the SCVT-grown sample, but a relatively low concentration of a shallower donor with activation energy 26 meV seems to be present. It can be argued that the 80 meV donor corresponds to the hydrogenic donor also found by Look et al in SCVT-grown material [1, 2]. Interestingly enough, a 26 meV main donor was extracted by Reynolds et al for melt-grown material [4].

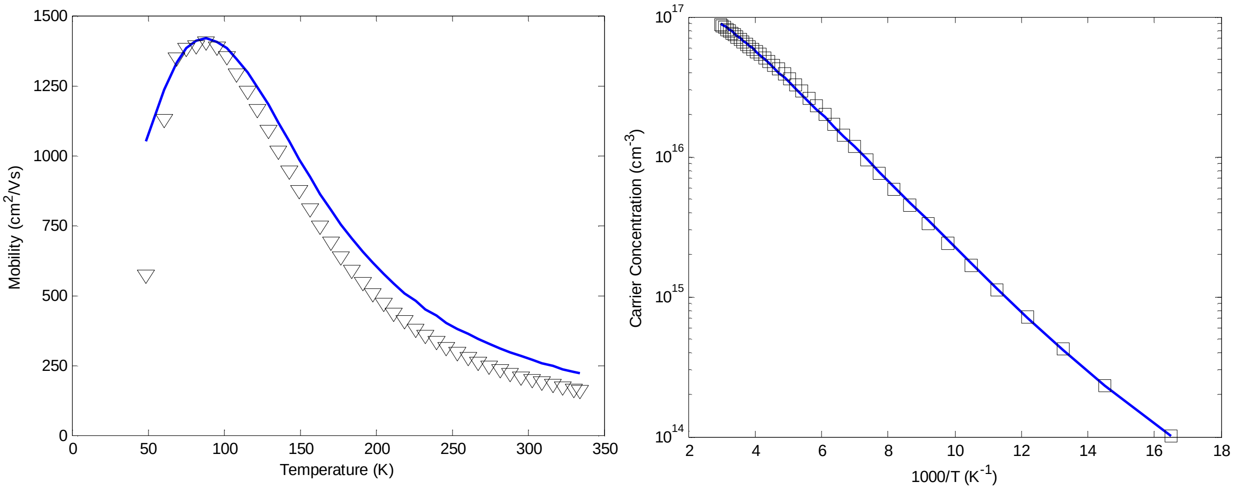

Figure 7.4 Mobility and Carrier concentration data and fit of unannealed SCVT-grown ZnO. Parameter values: N_A= 7.5×10^{15} cm^{-3}, E_I=9.32 eV, N_{D1}= 1.37×10^{17} cm^{-3}, E_{D1}=79.7 meV, N_{D2}= 8.1×10^{15} cm^{-3}, E_{D2}= 26.2 meV.

7.1.4 Analysis of Semi-Insulating Hydrothermal ZnO

Inspection of the hydrothermal ZnO data alone would suggest that this material has little in common with the other two types of ZnO considered. Surprisingly, a more detailed analysis reveals some similarities. The best fit of the mobility data turns out to occur with a deformation potential equal to the value of 3.8 eV as given in table 4.1. An acceptor concentration of 8.92×10^{16} cm^{-3} was also extracted from the mobility fit (see figure 7.5). Despite the very strong compensation in this semi-insulating sample, the model derived in section 3.1.2 is still valid and it can be shown that the carrier type should be strictly electrons (p = 0) up to compensation ratios very close to 100%.

A fit of the carrier concentration data using a single donor model yields an effective donor activation energy of 301 meV which is much larger than the values extracted for the other ZnO samples. Surprisingly, the extracted donor concentration is on the same order of magnitude as the main donor concentrations of the other two samples. This is a strong suggestion that whatever donor species is responsible for conduction in the melt-grown and SCVT-grown samples is also present in the hydrothermally grown sample, the difference in activation energy arising from the presence of deep levels. Although the extracted activation energy of 301 meV is comparable to the value of 340 meV obtained by Look et al **[3]** for hydrothermal ZnO, a much lower main donor and acceptor concentration was obtained in that work.

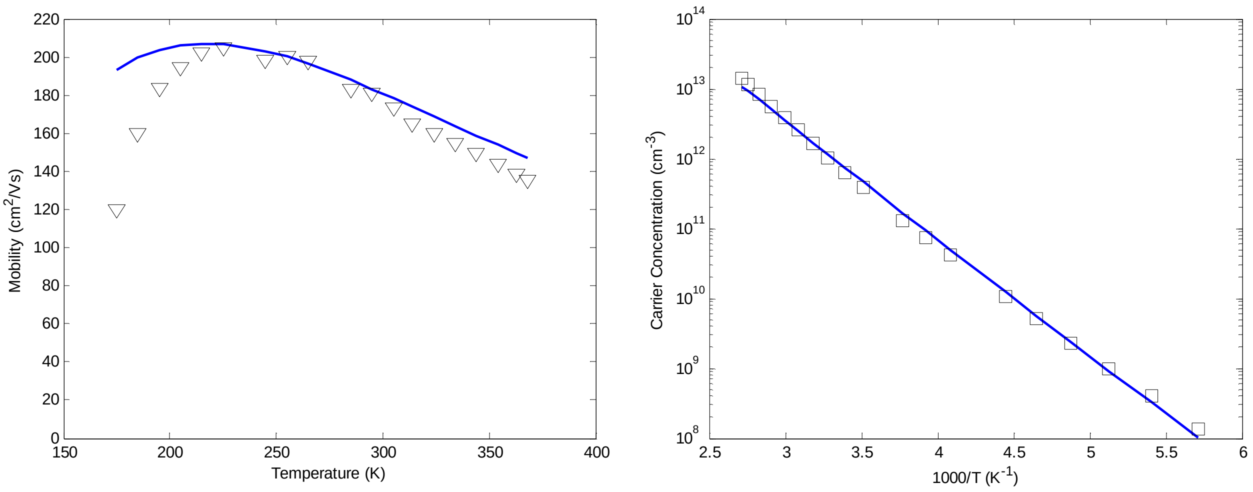

Figure 7.5 Mobility and carrier concentration fit of unannealed hydrothermally grown semi-insulating ZnO. Parameter values: N_A=8.92×10^{16} cm^{-3}, E_I=3.8 eV, N_D=9.33×10^{16} cm^{-3}, E_D=301 meV.

7.1.5 Summary and Discussion

The parameters of as-grown ZnO samples extracted in Sections 7.1.2 to 7.1.4 are summarized in table 7.1. Surprisingly enough, the main donor concentrations of all samples are found to be very similar. These main donors could be due to impurity atoms such as Ga, Al and H **[12]**, or even a lattice-related defect such as the Zn interstitial or the O vacancy (see chapter 4 for a discussion of shallow defects in ZnO). The donor activation energies differ significantly from each other, although the extreme case of 301 meV could be an apparent rather than actual activation energy. The D1 activation energies of 66.7 meV and 79.7 meV for melt-grown and SCVT-grown material respectively could very well correspond to the same (hydrogenic) donor, whatever its nature (impurity or lattice defect).

Table 7.1 Donor and acceptor concentrations and activation energies of different types of bulk as-grown ZnO. Concentration values are in 10^{16} cm^{-3} and activation energies are in meV.

Sample	N_{D1}	E_{D1}	N_{D2}	E_{D2}	N_{D3}	E_{D3}	N_A	E_I
melt-grown	5.32	66.7	11.8	43.7	0.377	7.2	0.334	15.5
SCVT-grown	13.7	79.7	-	-	0.810	26.2	0.750	9.32
hydrothermal	9.33	301.0	-	-	-	-	8.92	3.6

Assuming this, the main difference between these two samples is that the SCVT-grown material lacks a donor D2 with activation energy of about 44 meV, having a higher concentration of the hydrogenic donor D1 instead. The melt-grown sample has a third very shallow donor compensating the acceptor. Whether this donor actually exists or whether an apparent donor arises due to some other effect such as hopping conduction at low temperatures [2] is not known. In the present work it will simply be assumed that the donor exists, neglecting the possibility of low temperature anomalies. Similar assumptions were made in reference [1]. To the author's knowledge, no lattice defect or impurity has yet been associated with such a shallow donor. The very shallow donor D3 in the SCVT-grown sample is somewhat deeper than its counterpart in the melt-grown sample, but this value becomes much lower when the low temperature data is included (section 7.2.2). The acceptor concentration in the SCVT-grown sample is certainly somewhat higher than in the melt-grown sample.

7.2 COMPARISON OF DIFFERENT TYPES OF ZnO ANNEALED AT VARIOUS TEMPERATURES IN ARGON

7.2.1 Melt-grown ZnO Annealed in Argon

A square sample of melt-grown ZnO of thickness 450 μm and side lengths 5 mm was sequentially subjected to 30 minutes of annealing at 550 ºC, 740 ºC and 940 ºC in argon flow. The Hall results are shown in figures 7.4 and 7.5. It can be seen that the mobility peaks shift towards higher temperatures and decrease in height as the annealing temperature is increased. The mobility data regressions suggest that an increase in the acceptor concentration with annealing temperature is the cause for this change in the low-temperature mobility values. The trend of the carrier concentration data as a function of annealing temperature is more difficult to interpret by inspection of the data. A more detailed analysis through curve fitting does however show some trends. The results of fitting the mobility and carrier concentration data are shown in figure 7.6, and the extracted parameters are given in table 7.2. The results are certainly not unambiguous, but based on other results [1, 2] the following interpretation seems plausible:

There are essentially three donors D1, D2 and D3 present in this sample. D1 is the deepest in the 50 meV to 70 meV range, D2 has an intermediate activation energy of 38 meV to 44 meV and D3 is a very shallow donor below 10 meV. The unannealed sample has a high concentration of both D1 and D2. Sequential annealing up to 940 ºC steadily decreases the concentration of D2 by about an order of magnitude, i.e. it is effectively destroyed. At the same time the concentration of D1 steadily increases until it is about three times higher after annealing at 940 ºC. The activation energy E_{D1} of D1 does however fluctuate a lot, possibly reducing the credibility of the argument. Associating D2 with hydrogen does however give a sensible physical interpretation to the results: hydrogen that is initially present in the sample gives rise to a 44 meV donor level E_{D2}. At high annealing temperatures hydrogen diffuses out of the sample, leading to the destruction of this donor and its replacement by a deeper hydrogenic donor. A similar argument was presented in reference [1], albeit for the case of SCVT-grown annealed ZnO.

Table 7.2 Donor and acceptor concentrations and activation energies of melt-grown ZnO as a function of annealing temperature. Carrier concentration values are in 10^{16} cm^{-3} and activation energies in meV

Annealing Temp ºC)	N_{D1}	E_{D1}	N_{D2}	E_{D2}	N_{D3}	E_{D3}	N_A	E_l (eV)
N/A MN	5.32	66.7	11.8	43.7	0.352	7.2	0.334	15.5
550 M550	9.37	53.6	6.4	44.3	0.500	7.2	0.477	14.4
740 M740	13.3	61.3	5.0	38.0	0.527	3.2	0.518	14.4
940 M940	14.9	50.1	1.2	38.9	0.628	1.0	0.620	14.5

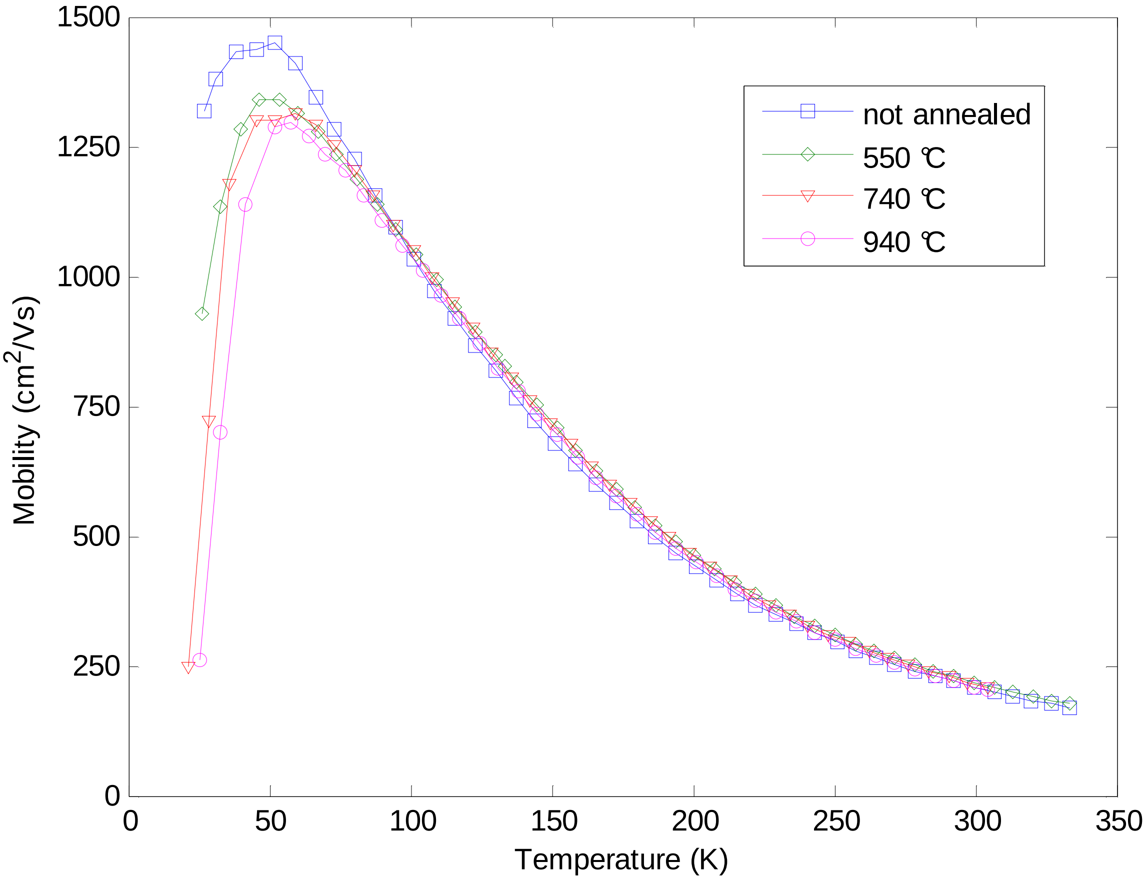

Figure 7.4 Hall mobility data of melt-grown ZnO annealed at different temperatures.

There are theoretical and experimental indications that hydrogen produces a donor in the 37 meV to 51 meV range [1, 2, 13, 14, 15]. In the present work, a main donor activation energy of 44 meV is extracted in the fit of the hydrogen implanted and annealed sample (see section 7.2.4). This is another indication that the 44 meV donor is most likely related to hydrogen. The remarkable similarity of the mobility and carrier concentration plots of the melt-grown sample and the hydrogen-implanted layer annealed at 200 °C would be explained if it is assumed that hydrogen is the dominant donor in both samples.

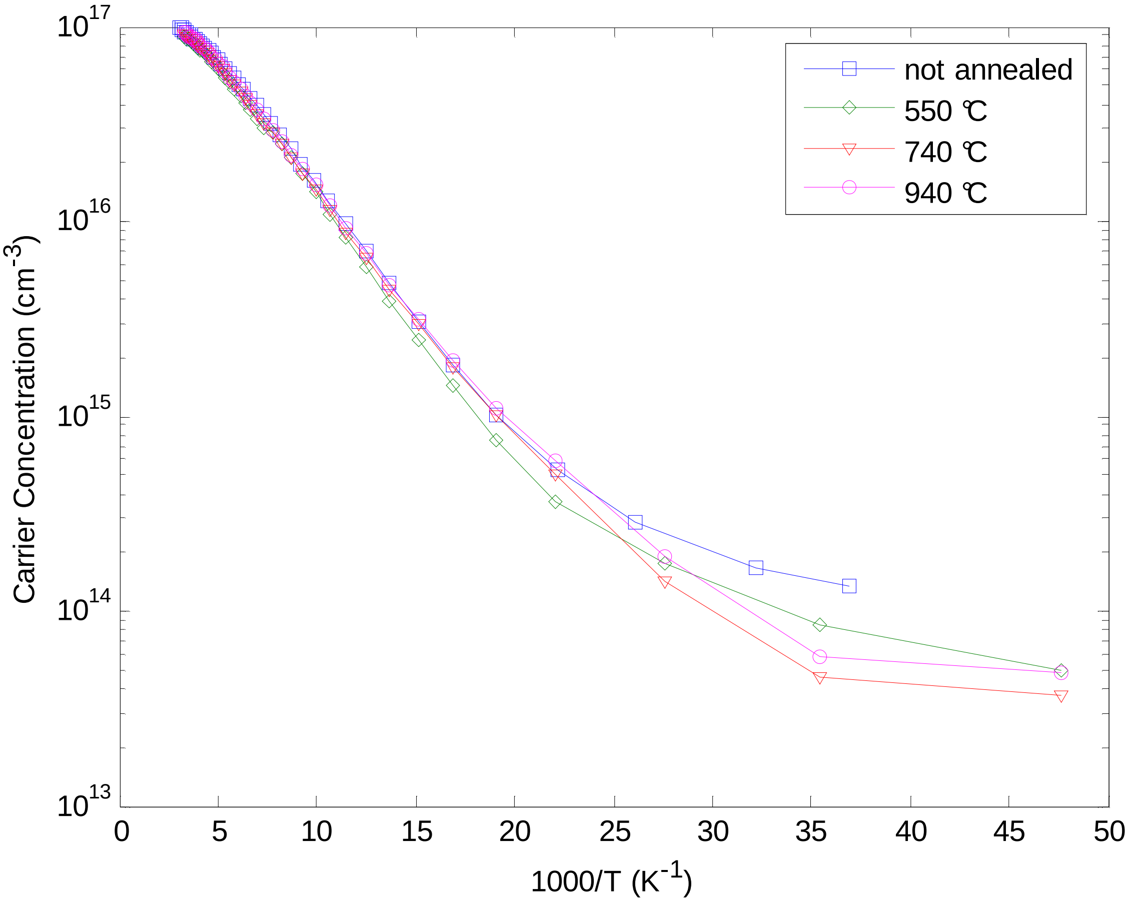

Figure 7.5 Hall carrier concentration of melt-grown ZnO annealed at different temperatures.

In reference [1] it was argued that nitrogen may be responsible for the increase in N_A at high annealing temperatures (In that study the samples were annealed in N_2 gas). The present results show that N_A also increases without the presence of nitrogen, probably due to the formation of lattice defects such as zinc vacancies. The very shallow donor concentration N_{D3} seems to “follow” N_A throughout, always being slightly higher than N_A. To the author’s knowledge no mechanism exists that would cause the concentration of a certain donor to increase in tandem with the acceptor concentration, and it is highly unlikely that the simultaneous increase is due to chance. The most likely explanation for this phenomenon is hopping conduction since it can be shown that the hopping carrier concentration in the range of temperature and compensation ratios considered in the present measurements is roughly proportional to N_A **[16]**. The inclusion of hopping conduction in the model is however beyond the scope of this study.

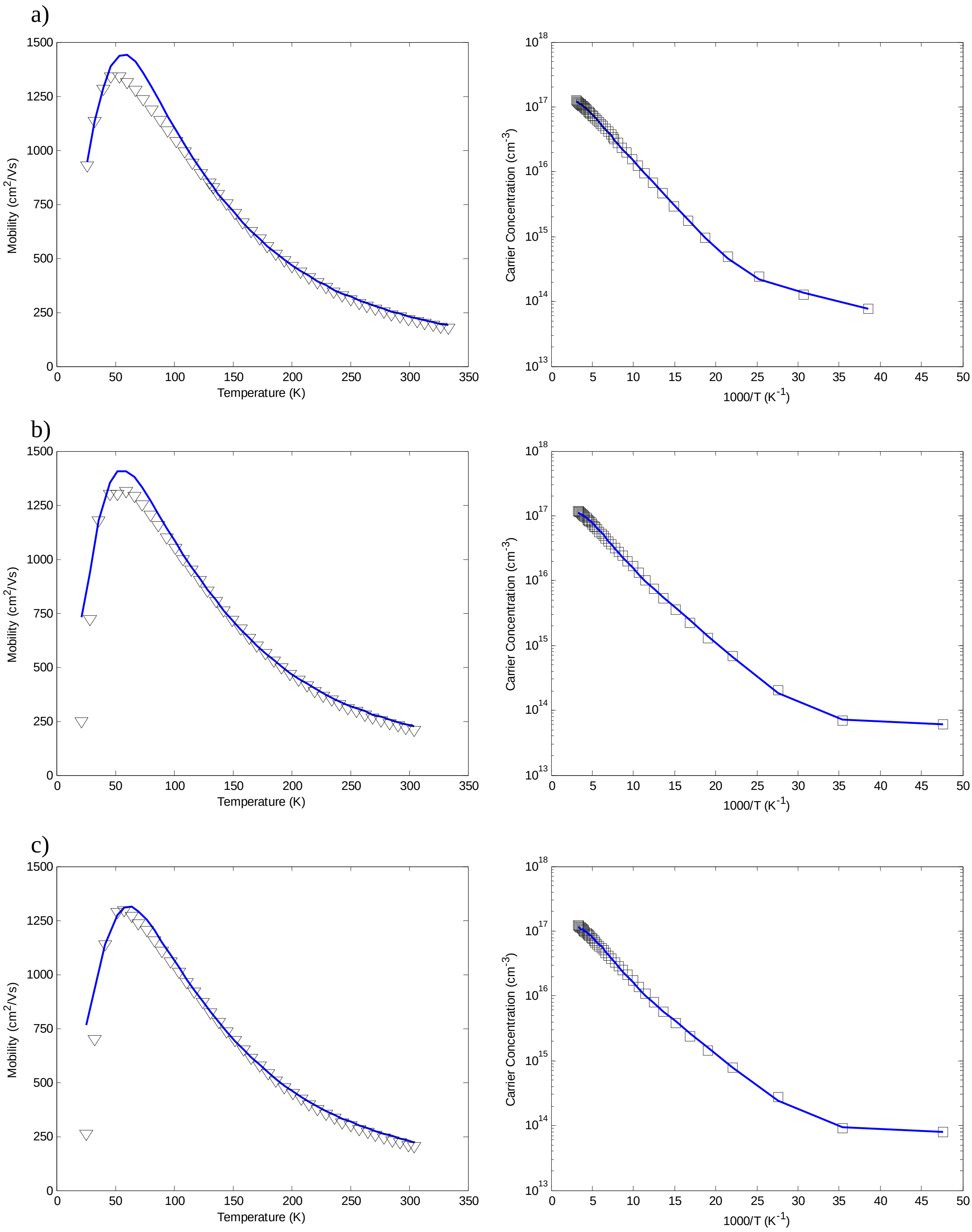

Figure 7.6 Hall data analysis of melt-grown ZnO sequentially annealed at different temperatures. a) annealed at 550 ºC; b) annealed at 740 ºC; c) annealed at 940 ºC.

7.2.2 SCVT-Grown ZnO Annealed in Argon

As was seen in the previous section, the melt-grown ZnO manufactured by Cermet Inc. did not appear to change appreciably with annealing by mere inspection of the data. By interpreting the changes as destruction of one donor species and creation of another, the transformation of the bulk material under annealing should however certainly be regarded as substantial. The annealing behavior of SCVT-grown material on the other hand seems quite significant from inspection of figures 7.7 and 7.8, especially in the low-temperature regime. A mathematical analysis however reveals that the changes are mainly related to an increase in the acceptor concentration on the one hand and the formation of a degenerate surface conduction channel on the other.

Inspection of figures 7.7 and 7.8 reveals that surface conduction plays a significant role in this sample, especially after annealing at 923 ºC in which case both carrier concentration and mobility profiles are observed to converge asymptotically to constant values at low temperatures. This data set is therefore a good candidate for performing a two-layer correction. The data gathered from the sample when it was only annealed up to 730 ºC or less also show a typical “two-layer” trend, but unfortunately it is not clear towards what value the carrier concentrations and mobilities converge since sufficiently low temperature data is not available.

Nonetheless, approximate two-layer corrections were attempted for all sets of data, even the data pertaining to the as-grown sample. The “corrected” mobility and carrier concentration data are shown in figures 7.9 and 7.10 respectively. The low temperature mobility convergence value for the data of the sample annealed at 930 ºC is 11.5 cm^2/Vs. This value was also used for all the other samples since it is difficult to estimate the convergence values from the available data in those cases. The low temperature (apparent) carrier concentration values were taken as $1.48\times10^{15}cm^{-3}$, 1.0×10^{15} cm^{-3}, 6.0×10^{14} cm^{-3} and 1.0×10^{14} cm^{-3} for the samples annealed at 920 ºC, 730 ºC, 550 ºC and not annealed respectively. The original data is included on the plots to facilitate comparison. Even though the corrections are probably quite inaccurate, the corrected data fits the charge balance equation much better in the low temperature regime. The two-layer correction will in any case only affect the low temperature data and can therefore not change the extracted deeper donor concentrations and activation energies appreciably.

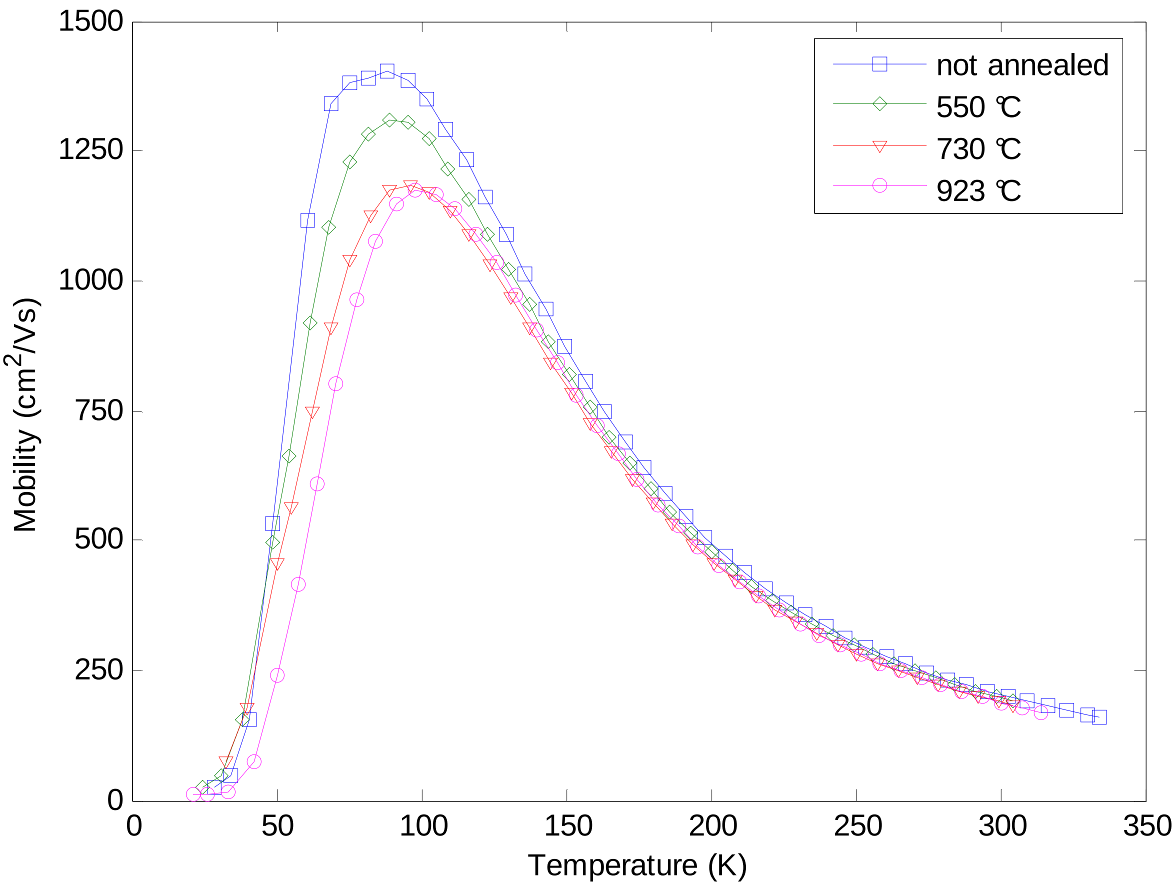

Figure 7.7 Hall mobility versus Temperature of SCVT-grown ZnO annealed in argon at the indicated temperatures

The mobility data fits are not as good as their counterparts in the melt-grown ZnO annealing study, as can be seen in figure 7.11. The deformation potential values for the best fit are somewhat lower, but also closer to the literature value of 3.8 eV (see table 4.1). In table 7.3 one can see that the acceptor concentration extracted from the mobility fits increases steadily with annealing temperature.

In fitting the carrier concentration data it was decided that a compromise be made between making use of the corrected low temperature data and avoiding artifacts due to inherent inaccuracies in the correction procedure. All carrier concentration data below 40 K (1000/T = 25) was ignored for fitting purposes. The data fits and results are given in figure 7.11 and table 7.3 respectively. Initially a three donor model was used to fit all the data, but in the case of the not annealed sample SN (refer to table 7.3 for the designations) and the sample annealed at 923 C S923 it was found that there really only appear to be two donor levels. Even in the case of S550 and S730 the existence of a third donor level can be questioned due to the small concentration obtained (refer to table 7.3 for the designations).

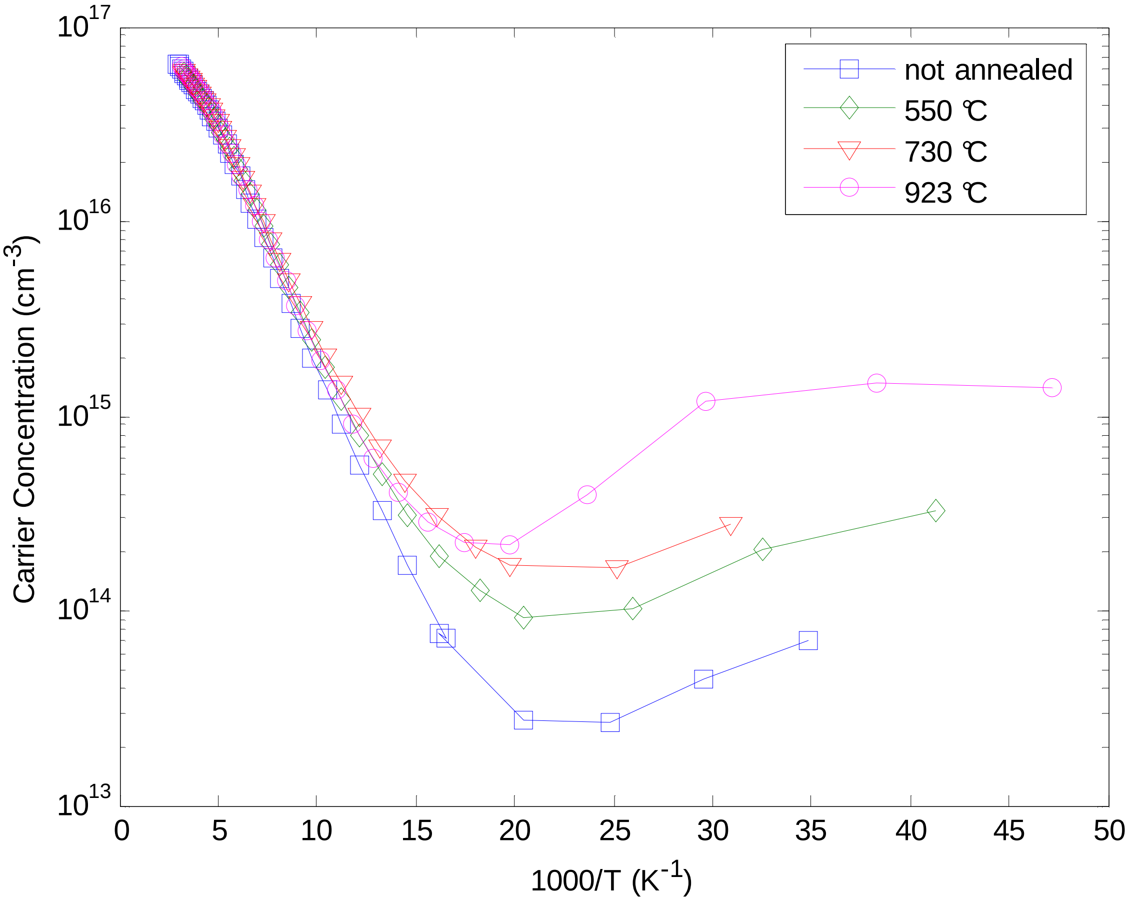

Figure 7.8 Hall carrier concentration of SCVT-grown ZnO annealed in Argon at different temperatures

In essence, then, there is only one main relatively deep donor D1 present in this sample. The designation D1 is no coincidence, since it will be argued here that D1 in the melt-grown and SCVT-grown sample respectively corresponds to the same (hydrogenic) donor even though the activation energy extracted in these samples differs significantly. Whether or not D1 actually corresponds to the same donor in both samples, it is clear from table 7.3 that D1 is quite stable under annealing in this sample, with neither its concentration nor its activation energy changing appreciably. A small concentration of a 40 meV to 55 meV donor appears to be present in S550 and S730 (refer to table 7.3 for the designations). Interestingly enough, a similar relationship between D1 and D2 as discussed in the melt-grown sample is observed here in that creation of D2 leads to partial destruction of D1 and vice versa. Assuming that this is not merely a mathematical artifact, it can be argued that D2 corresponds to a small concentration of a hydrogen donor that is activated at about 550 °C, decreases in concentration when subjected to a 730 °C anneal and is largely destroyed above 900 °C.

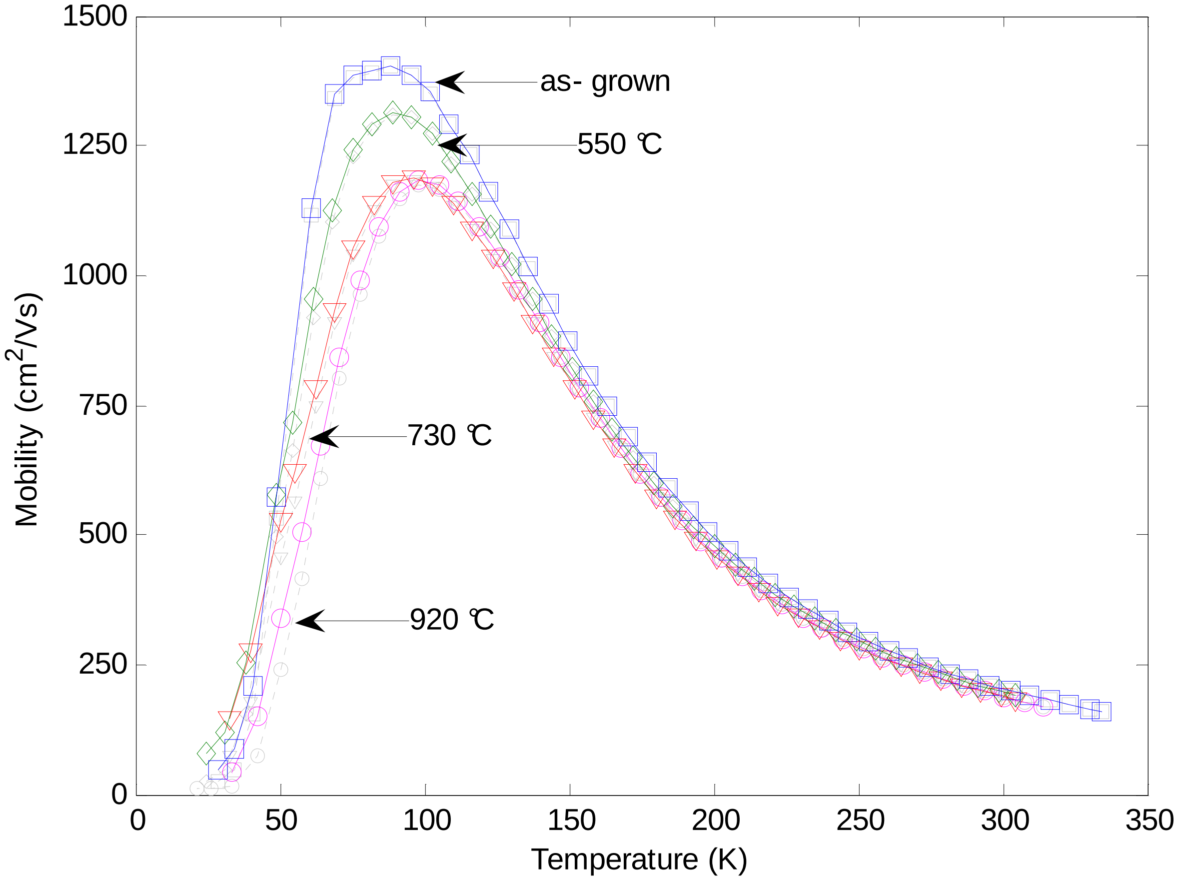

Figure 7.9 Two-layer corrected Hall mobility of SCVT-grown ZnO annealed at different Temperatures. The uncorrected data is also shown for comparison.

The acceptor concentration increases steadily with annealing temperature similar to the melt-grown sample. Initially N_A is however somewhat higher, and in the literature a similar annealing experiment with SCVT-grown material is described in reference [5]. The donor activation energies extracted there are somewhat different with a main donor of 67 meV and two other donors with activation energy 30 meV and 150 meV. The surface conduction in reference [5] is explained by hydrogen accumulation at the sample surface, and X-ray photo spectroscopy (XPS) results are given to support that statement. It is also mentioned that the surface conduction decreases at an annealing temperature of 800 °C. The fact that hydrogen is expected to out-diffuse above 800 °C is cited as additional support for the claim that hydrogen (in the form of OH groups) is responsible for surface conduction. Hydrogen-induced surface conduction channels have been investigated in much earlier work, where it was found that these channels are stable with respect to oxygen exposure [17]. It has long been known that ambient sensitive ZnO surface conduction channels can be produced by a variety of methods including ultra-violet (UV) and electron beam irradiation [17]. More recently, ambient sensitive surface conduction channels that actually form at elevated temperature (in contrast to hydrogen channels that are destroyed upon annealing) have been observed on Li and Cu-doped semi-insulating ZnO [7].

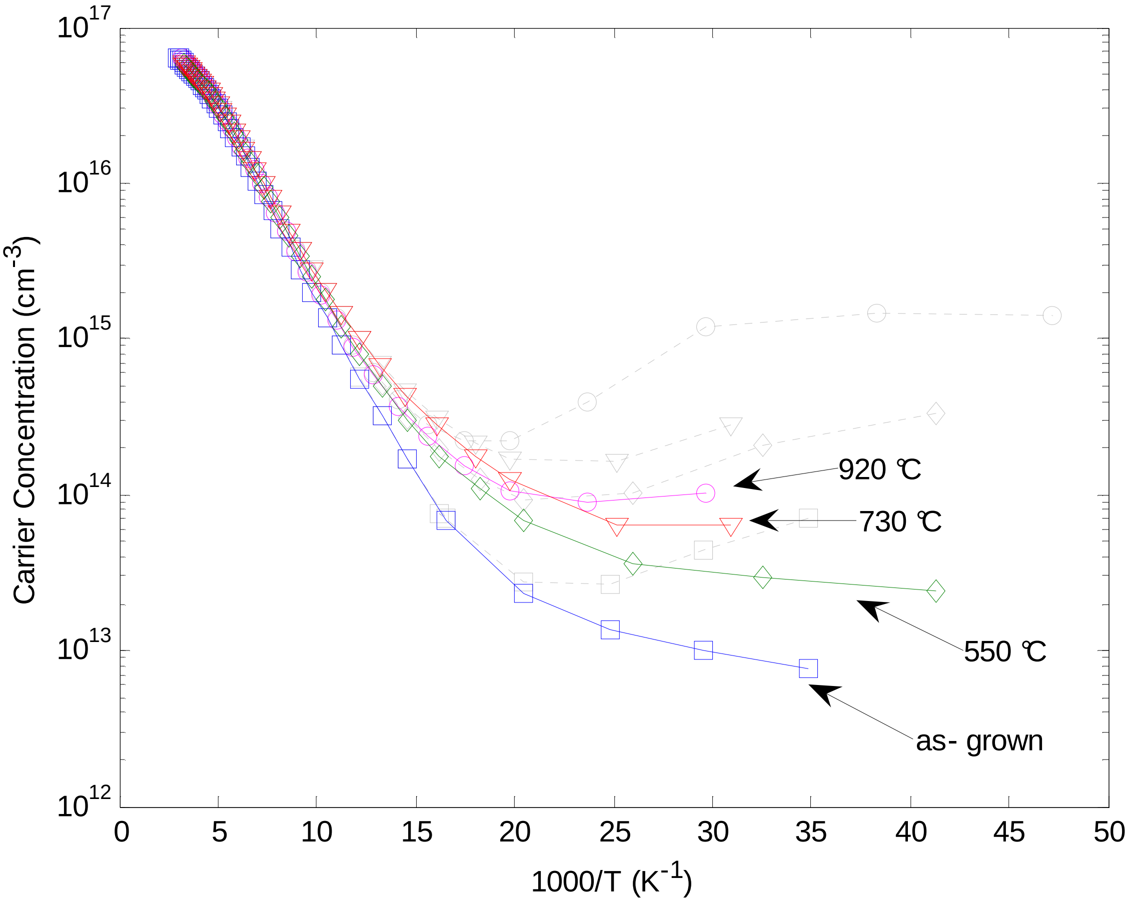

Figure 7.10 Two-layer corrected Hall carrier concentration of SCVT-grown ZnO annealed at different Temperatures. The uncorrected data is also shown for comparison.

a)

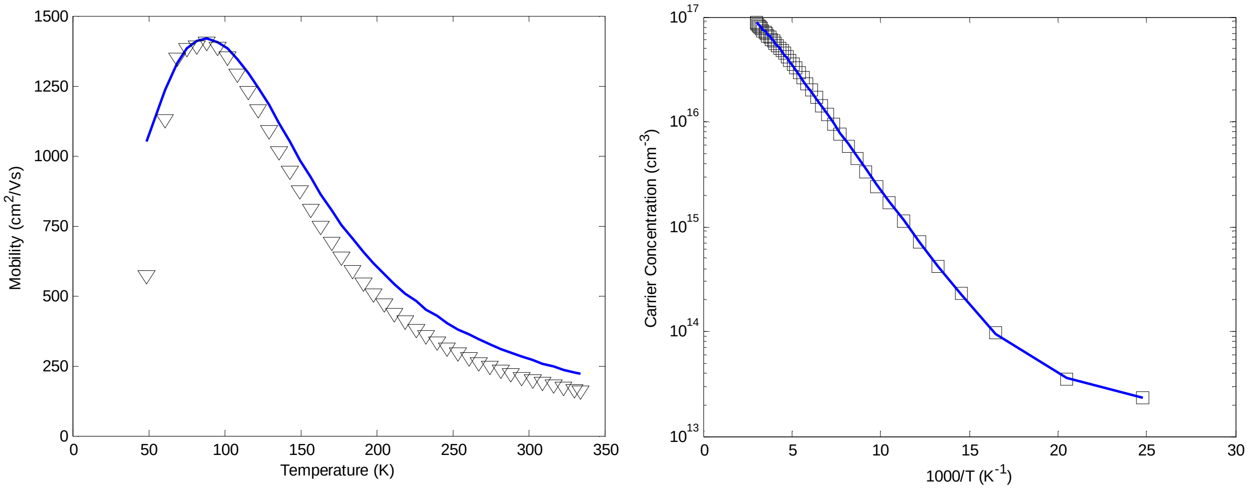
Mobility (cm^2/Vs)
1500
1250
1000
750
500
250
0
0
50
100
150
200
250
300
350
Temperature (K)
Carrier Concentration (cm^{-3})
10^{17}
10^{16}
10^{15}
10^{14}
10^{13}
0
5
10
15
20
25
30
1000/T (K^{-1})

b)

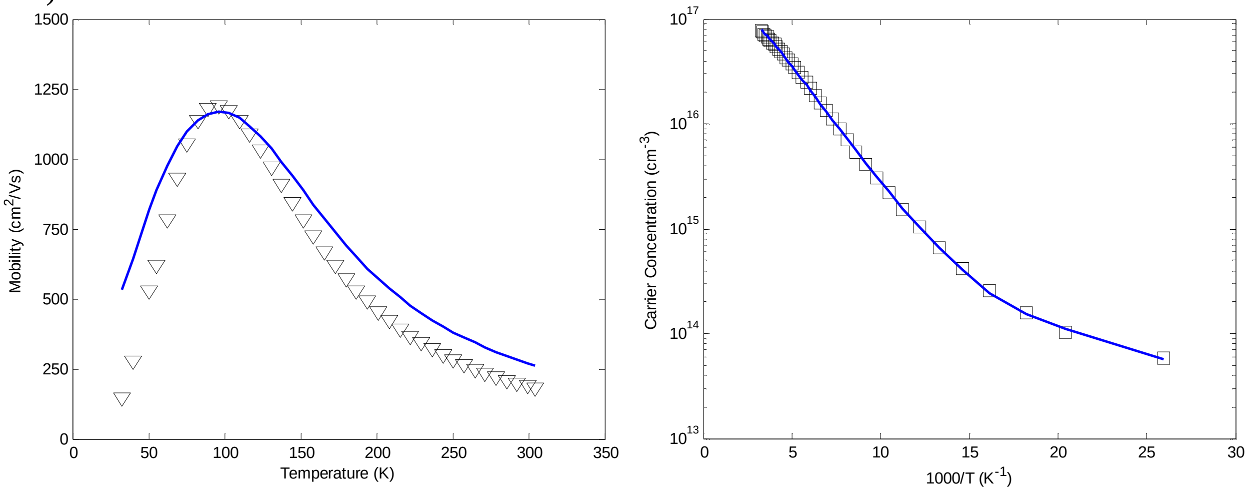
Mobility (cm^2/Vs)
1500
1250
1000
750
500
250
0
0
50
100
150
200
250
300
350
Temperature (K)
Carrier Concentration (cm^{-3})
10^{17}
10^{16}
10^{15}
10^{14}
10^{13}
0
5
10
15
20
25
30
1000/T (K^{-1})

c)

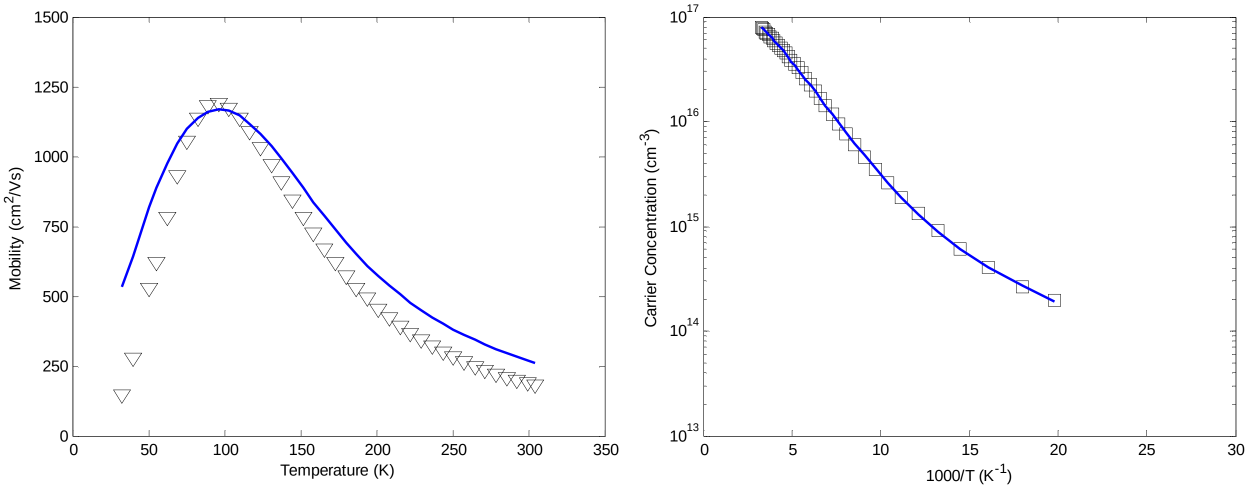
Mobility (cm^2/Vs)
1500
1250
1000
750
500
250
0
0
50
100
150
200
250
300
350
Temperature (K)
Carrier Concentration (cm^{-3})
10^{17}
10^{16}
10^{15}
10^{14}
10^{13}
0
5
10
15
20
25
30
1000/T (K^{-1})

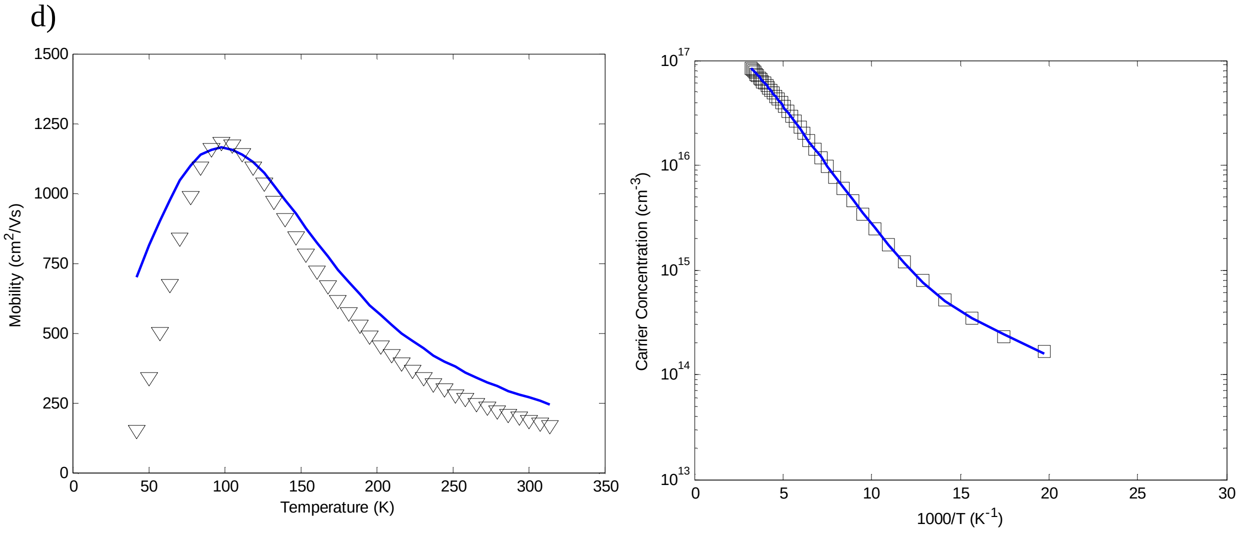

Figure 7.11 Hall data analysis of SCVT-grown ZnO sequentially annealed at different temperatures. a) not annealed; b) annealed at 550 ºC; c) annealed at 730 ºC; d) annealed at 923 ºC.

Since the conduction channel in the present results has been shown not only to be stable up to 923 ºC but to actually only fully develop at this temperature, it seems unlikely that hydrogen alone should be responsible for its formation since hydrogen is expected to effuse from the sample already at lower temperatures. On the other hand, if this conduction channel is not hydrogen-related, it would be expected to show sensitivity to oxygen ambient **[7, 17]**. Although the SCVT-grown sample was not explicitly tested for its ambient response, such a test was indeed performed on the hydrothermally grown ZnO at room temperature, and no such sensitivity was observed. These results indicate that the origin of surface conduction on ZnO has yet to be satisfactorily explained.

Table 7.3 Donor and acceptor concentrations and activation energies of SCVT-grown ZnO as a function of annealing temperature. Concentrations are in 10^{16} cm^{-3} and activation energies in meV

Annealing Temp (ºC)		N_{D1}	E_{D1}	N_{D2}	E_{D2}	N_{D3}	E_{D3}	N_A	E_l
0	SN	13.8	80.0	-	-	0.756	10.5	0.750	9.23
550	S550	12.9	78.6	0.342	54.8	1.02	10.6	1.00	9.23
730	S730	12.9	76.3	0.125	40.0	1.37	8.6	1.35	9.23
923	S923	13.7	77.6	-	-	1.41	15.3	1.34	9.23

7.2.3 Hydrothermally Grown ZnO Annealed in Argon

Annealing of semi-insulating hydrothermal ZnO in argon at temperatures above 500 ºC resulted in a marked change in the electrical properties of the sample throughout the entire measurement temperature range considered. Annealing at 550 ºC resulted in roughly constant mobility and carrier concentration profiles above room temperature, but the data becomes increasingly noisy below room temperature and finally the sample was not measurable any longer at about 200 K, as shown in figure 7.12.

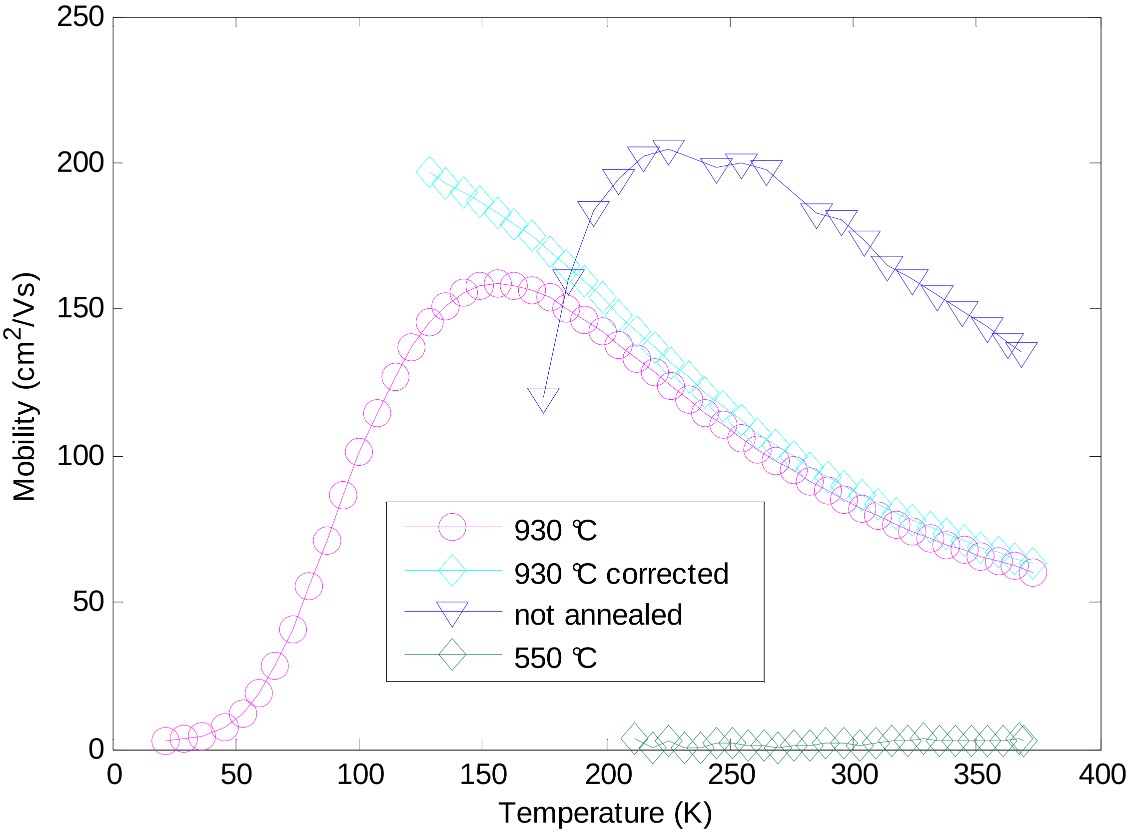

Figure 7.12 Mobility plot of hydrothermal as-grown and annealed ZnO. The two-layer corrected data of the sample annealed at 930 ºC is also shown. The low temperature correction values were taken as 2.98 cm^2/Vs and 1.42×10^{14} cm^{-3} for mobility and carrier concentration respectively, and the corresponding sheet carrier concentration is 3.02×10^{15} cm^{-2}. The mobility of the sample annealed at 550 ºC is roughly constant and ranges from about 2 to 3cm^2/Vs.

The conduction is characterized by a relatively high carrier concentration and very low mobility. Assuming that the bulk remains semi-insulating at these temperatures, it follows that a surface conduction channel with mobility of about 2-3 cm^2/Vs and sheet carrier concentration of about 2-4×10^{15} cm^{-2} has formed. The data of the sample annealed at 930 ºC suggests that a degenerate surface layer formed on this sample at high annealing temperatures. It is therefore plausible to argue that this degenerate layer already forms at (or below) 550 ºC. The fact that the high-temperature data of the 550 ºC sample is very similar to the low-temperature data of the 930 ºC sample (see figure 7.13) further supports this idea and suggests that the degenerate layer formed at 550 ºC remains stable and essentially unaltered up to an annealing temperature of 930 ºC .

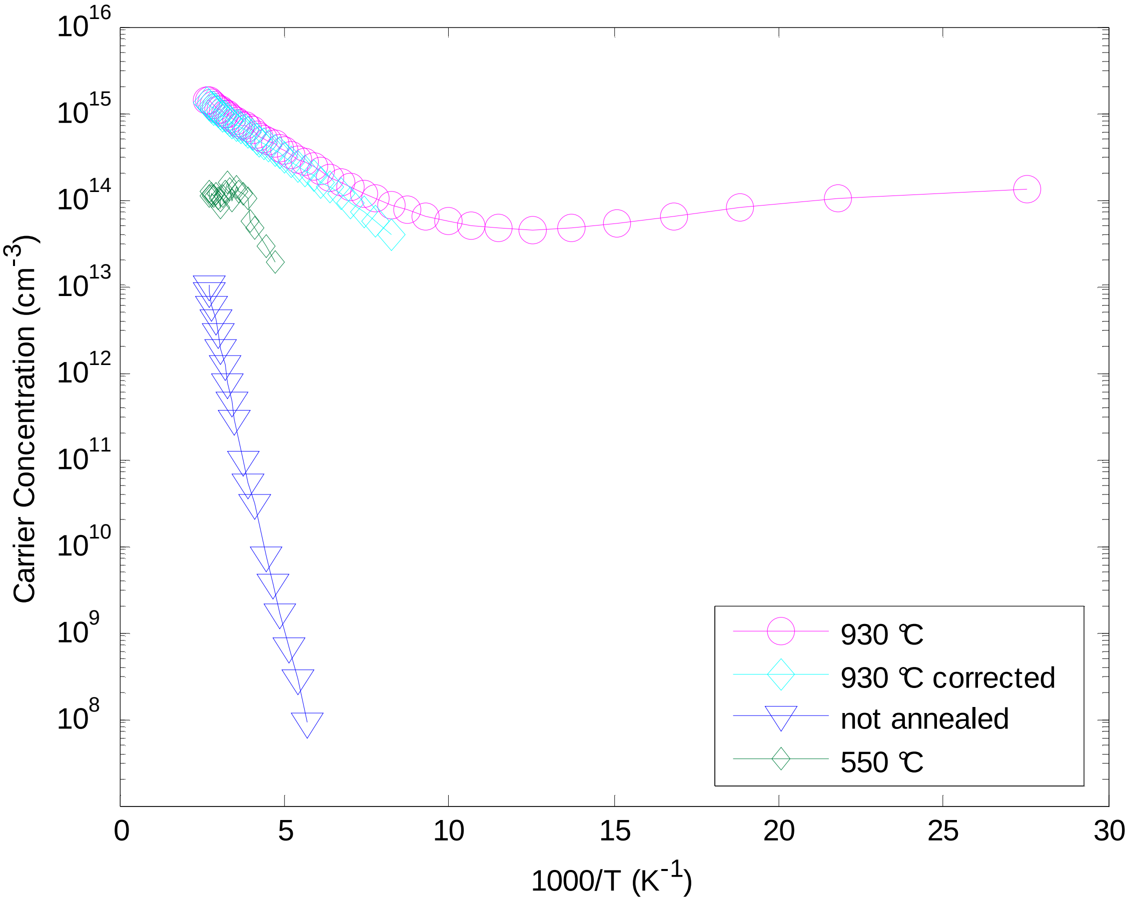

Figure 7.13 Carrier concentration plot of hydrothermal ZnO as-grown and annealed at 930 ºC. The annealed corrected data is also shown. The low temperature correction values were taken as 2.98 cm^2/Vs and 1.42×10^{14} cm^{-3} for mobility and carrier concentration respectively.

The bulk carrier concentration of the conducting surface channel is of course not known since its thickness was not determined. Although the 930 ºC annealed data looks like a promising candidate for a two-layer correction, it turns out that the two-layer model does not describe the data very well. Only in the high temperature region above 150 K seems to yield credible results. The corrected data did not fit the carrier concentration and mobility models well, and no regression results will be presented. From inspection of the data it does however appear that both bulk and surface changes occur through annealing and that some form of degenerate layer must be present.

As to the question of the origin of the layer, it has to be said that further studies are necessary. The surface conduction found here does not appear to conform to the properties of such layers studied and published previously in the literature. In particular, the ambient-stable layers reported usually involve hydrogen or are at least thought to involve hydrogen **[5]**, and such layers are shown to be destroyed at annealing temperatures well below temperatures employed in this study **[17]**. The conduction of the samples in the present study showed no ambient-dependence; oxygen has been shown to destroy surface channels not related to hydrogen **[7]**, but the conduction channel of samples in this study remained intact at ambient pressure in air.

7.2.4 Hydrogen-Implanted ZnO Annealed in Argon

Layers of hydrogen-implanted semi-insulating ZnO also showed dramatic changes under annealing. The as-manufactured material is characterized by a near-constant low mobility of about 40 cm^2/Vs above room temperature. The carrier concentration is in the 10^{15} cm^{-3} range, freezing out rapidly below room temperature (figures 7.14 and 7.15).

Surprisingly enough, this highly defective layer becomes almost perfect device quality ZnO very similar to the melt-grown bulk ZnO analyzed in this study (section 7.2.1). The main difference between this sample and the unannealed melt-grown sample is that it only has one main donor D2 with activation energy of about 44 meV and lacks the “hydrogenic” donor D1 with activation energy of 50-70 meV (see figures 7.14 through 7.16 and table 7.4). In section 7.2.1, D2 has already been associated with hydrogen, and the results here support the claim that hydrogen does indeed give rise to a donor with activation energy of about 44 meV. In the literature, activation energies of 35 meV to 51 meV have been attributed to hydrogen, and the present results are well within this range (see table 7.4) **[1, 2, 8, 13]**. D2 is shown to remain stable up to 300 ºC, the extracted activation energy changing only marginally although the concentration increases noticeably. The reason for the increase in concentration is not clear; possible explanations are that more hydrogen-related defects are activated at this temperature. Alternatively this increase could be only an apparent one due to a change in the doping profile of the layer caused by hydrogen diffusion. After annealing at 400 ºC the room temperature carrier concentration drops to about 10% of the value obtained after the 200 ºC and 300 ºC anneals. The mobility also decreases substantially, and neither the carrier concentration nor the mobility profiles fitted the usual models satisfactorily. The reason for this may be a large degree of inhomogeneity of the doping and irradiation damage profiles. The acceptor concentration extracted from the mobility fits is much larger in the sample annealed at 300 ºC (H300) than in the sample annealed at 200 ºC (H200) as given in table 7.4.

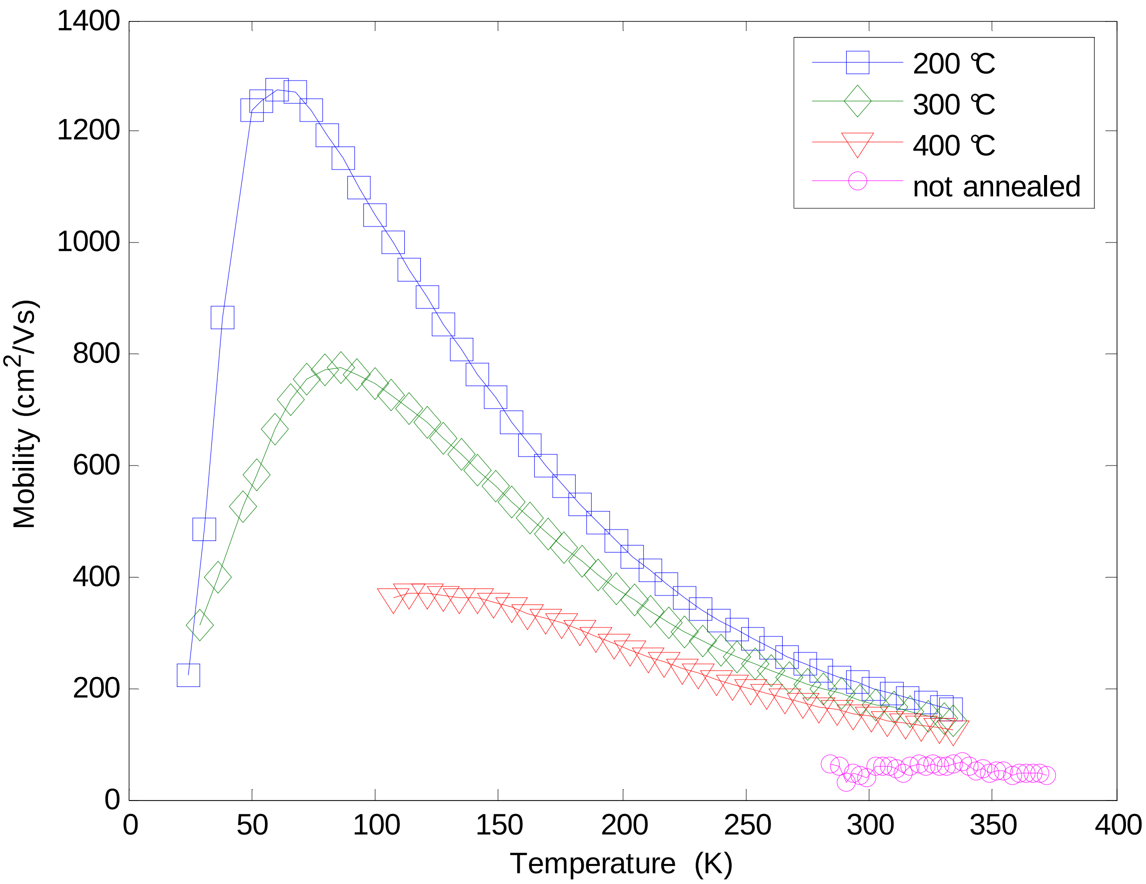

Figure 7.14 Mobility versus temperature data of proton-implanted hydrothermal ZnO layers annealed for 90 minutes at different temperatures.

The much higher acceptor concentration in H300 may be due to activation of radiation-induced acceptor defects. Since hydrogen has been shown to passivate acceptors, the effusion of hydrogen can also be responsible for the higher N_A value. It should be noted that the lower carrier concentration of the sample annealed at 400 °C does not per se imply a substantial decrease in the donor concentration N_{D2}. The reduction in carrier concentration may be as a result of a further increase in N_A only. It is however likely that hydrogen effuses substantially at these temperatures giving rise to a decrease in N_{D2}.

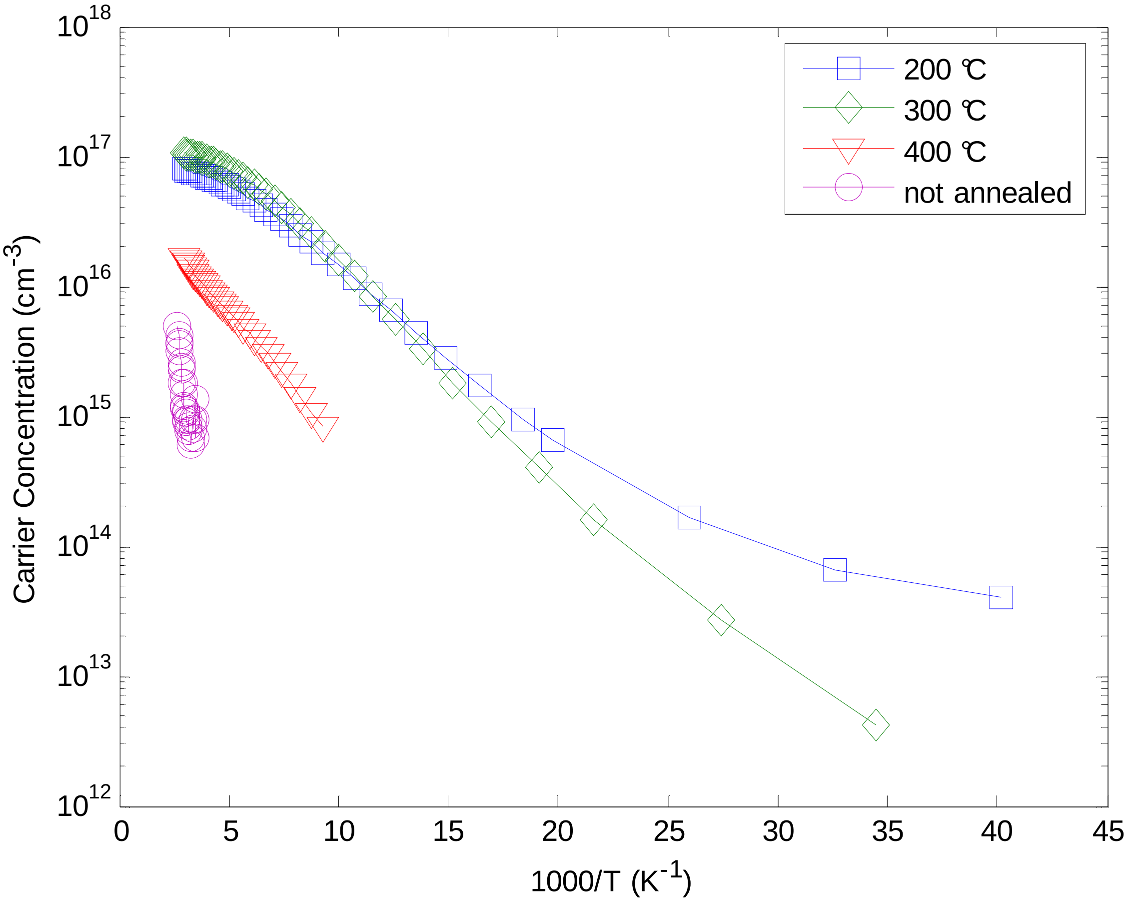

Figure 7.15 Carrier Density versus reciprocal temperature data of proton-implanted hydrothermal ZnO layers annealed for 90 minutes at different temperatures.

Highly conductive hydrogen-implanted n^+-layers have recently been shown to be stable up to annealing at 600 °C, especially when the implantation concentration was very high [11]. Such stability could however be due to defects caused by irreversible lattice damage due to the high implantation concentration rather than the hydrogen remaining in place, and secondary ion mass spectroscopy (SIMS) results in that study indeed confirm a substantial effusion of hydrogen [11].

The shallow donor D3 is seen to have both a higher concentration and activation energy in H300 compared to H200. Once again a type of self-compensating effect is evident here since the concentration of D3 once again tends to always be just slightly higher than N_A. Donors of similar activation energy were found in the melt-grown and SCVT-grown samples, but the physical origin of this donor will not be speculated on here.

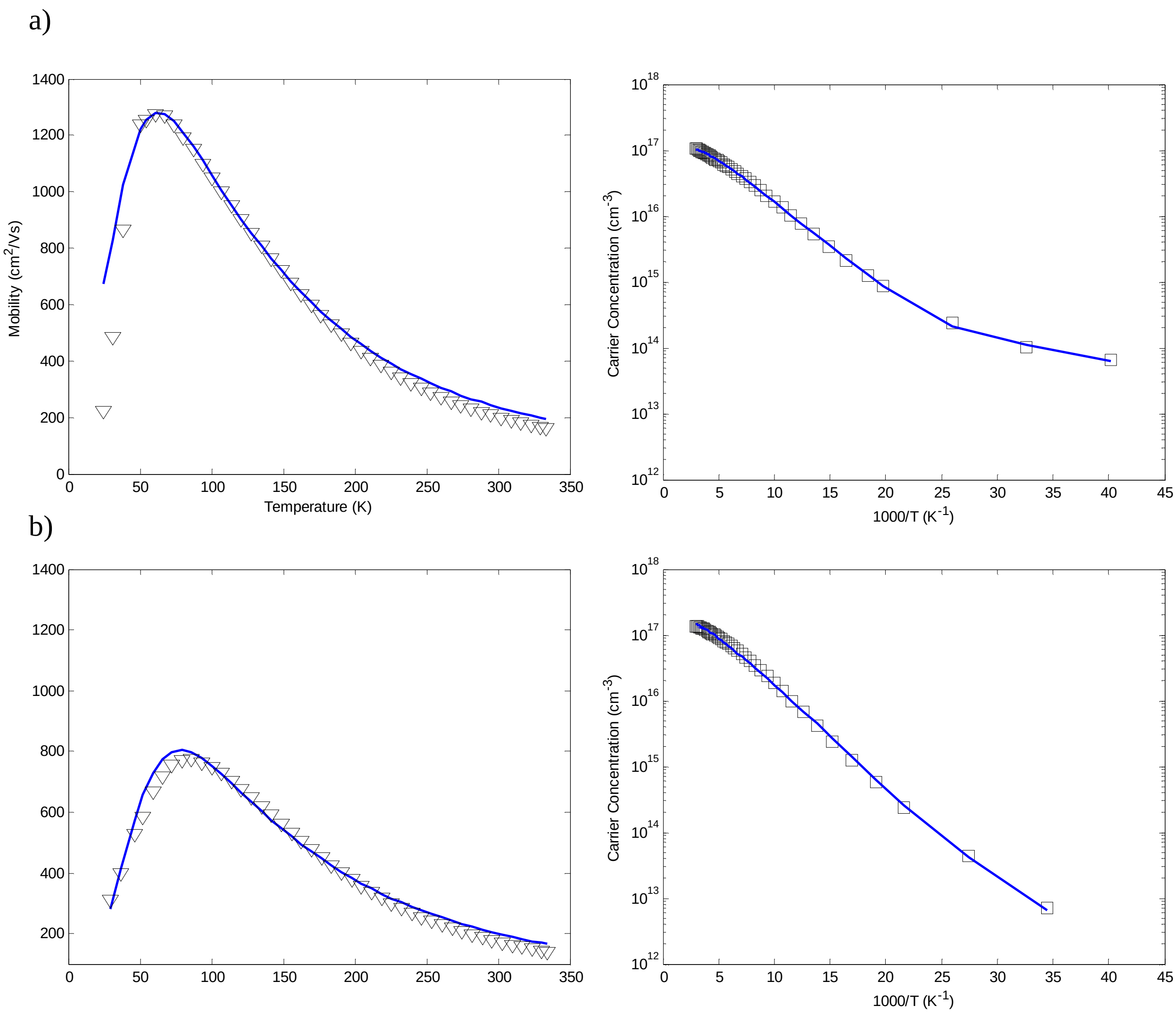

Figure 7.16 Hall data analysis of hydrogen-implanted SI ZnO annealed for 90 minutes at different temperatures. a) annealed at 200 ºC; b) annealed at 300 ºC. Fit parameters are shown in table 7.4.

Table 7.4 Donor and acceptor concentrations and activation energies of hydrogen-implanted SI ZnO as a function of annealing temperature. Concentrations are given in 10^{16} cm^{-3} and activation energies in meV

Annealing Temp (°C)	N_{D2}	E_{D2}	N_{D3}	E_{D3}	N_A	E_l (eV)
200 H200	12.2	44.3	0.72	6.3	0.70	14.1
300 H300	18.4	45.7	2.04	17.5	1.85	17.7

References

[1] Look D.C., Jones R.L., Sizelove J.R., Garces N.Y., Giles N.C., *The path to ZnO devices: donor and acceptor dynamics*, phys. stat. sol. (a) 195, 171 (2003)

[2] Look D.C., Reynolds D.C., Sizelove J.R., Jones R.L., Litton C.W., Cantwell G., Harsch W.C., *Electrical properties of bulk ZnO*, Solid State Communications 105, 399 (1998)

[3] Look D.C., *Recent advances in ZnO materials and devices*, Materials Science and Engineering B80, 383 (2001)

[4] Reynolds D.C., Litton C.W., Look D.C., Hoelscher C.E., Claflin B., Collins T.C., Nause J., Nemeth B., *High quality melt- grown ZnO single crystals*, Journal of Applied Physics 95, 4802 (2003)

[5] Look D.C., Mosbacker H.L., Strzhemechny Y.M., Brillson L.J., *Effects of surface conduction on Hall effect measurements in ZnO*, Superlattices and Microstructures 38, 406 (2005)

[6] Shaldin Y.V. and Varchulska J., *Effect of Heat Treatment on the Magnetic Properties of Hydrothermally Grown ZnO Crystals*, Inorganic Materials 39, 1052 (2003)

[7] Schmidt O., Geis A., Kiesel P., Van de Walle G., Johnson N.M., Bakin A., Waag A., Döhler G.H., *Analysis of a conducting channel at the native Zinc Oxide surface*, Superlattices and Microstructures 39, 8 (2006)

[8] Hutson A.R., *Hall effect studies of doped Zinc Oxide single crystals*, Physical Review 108, 222 (1957)

[9] Kucheyev S.O., Deenapanray P.N.K., Jagadish C., Williams J.S., Mitsuaki Yano, Kazuto Koike, Shigehiko Sasa, and Masataka Inoue, Ken-ichi Ogata, *Electrical isolation of ZnO by ion bombardment*, Applied Physics Letters 81, 3350 (2002)

[10] Seung Yeop Myong, Koeng Su Lim, *Highly stable and textured hydrogenated ZnO thin films*, Applied Physics Letters 82, 3026 (2003)

[11] Monakhov E.V., Christensen J.S., Maknys K., Svensson B.G., Kuznetsov A.Yu., *Hydrogen implantation into ZnO for* n^+*- layer formation*, Applied Physics Letters 87, 191910 (2005)

[12] Look D.C., Claflin B., Alivov Ya.I., Park S.J., *The future of ZnO light emitters*, phys. stat. sol. (a) 201, 2203 (2004)

[13] Thomas D.G., Lander J.J., *Hydrogen as a donor in ZnO*, Journal of Chemical Physics 25, 1136 (1956)

[14] Van de Walle C.G., *Hydrogen as a cause of doping in Zinc Oxide*, Physical Review Letters 85, 1012 (2000)

[15] Look D.C., Mosbacker H.L., Strzhemechny Y.M., Brillson L.J., *Effects of surface conduction on Hall effect measurements in ZnO*, Superlattices and Microstructures 38, 406 (2005)

[16] Mott N.F., Twose W.D., *The theory of impurity conduction*, Advances in Physics 10, 107 (1961)

[17] Yaron G., Many A., Goldstein Y., *Quantized electron accumulation layers on ZnO surfaces produced by low-energy hydrogen ion implantation*, Journal of Applied Physics 58, 3508 (1985)

CHAPTER 8

CONCLUSIONS

The temperature dependent Hall measurement and analysis system developed and implemented in this study has been shown to be an extremely useful tool in the investigation of bulk ZnO samples with a wide spectrum of electrical properties. Examples ranging from purely non-degenerate specimens to samples with a highly conductive degenerate surface channel have been successfully analyzed with regard to their shallow donors and compensating acceptors. One, two and three donor models were implemented and excellent fits to most data were obtained. The mobility data fitted the model reasonably well, notwithstanding the fact that rather unrealistic deformation potential values were used. Realistic acceptor concentrations were however obtained.

ZnO samples grown by different methods were found to have vastly different electrical properties. Melt-grown ZnO was found to have two main donors, one hydrogenic donor D1 of about 67 meV and a donor D2 with activation energy 44 meV that was attributed to hydrogen. The sample grown by the seeded chemical vapour transport method was found to have only one main donor D1 of about 80 meV attributed also to a hydrogenic donor, and traces of D2. A donor with activation energy of 301 meV was extracted for the hydrothermally grown sample but this result may not be correct due to the near-unity compensation ratio of this sample.

Annealing of the samples in a non-reacting argon atmosphere up to above 900 ºC resulted in significant changes in all samples. In the melt-grown material partial destruction of D2 seemed to occur with annealing, and this is interpreted as effusion of hydrogen. The SCVT-grown sample and the hydrothermally grown sample both developed a degenerate surface layer at high annealing temperatures. The bulk of the SCVT- grown sample changed relatively little, and it is concluded that the hydrogenic donor D1 is stable up to annealing above 900 ºC. The acceptor concentration increased to about twice the as-grown value with annealing above 900 ºC in both SCVT-grown and melt-grown samples. The bulk of the hydrothermally grown sample became more conductive at high annealing temperatures, but no good analysis of the data could be achieved.

Hydrogen implanted layers on bulk ZnO were found to have only one donor D2 (44 meV) when annealed at 200 ºC and 300 ºC. This is another indication that D2 is indeed due to hydrogen. Despite the remarkable similarity of the implanted layers and the melt-grown bulk material, the annealing properties were shown to be completely different. At 300 ºC annealing and above the acceptor concentration increased rapidly, indicating the presence of deep level traps that are possibly passivated by hydrogen at lower annealing temperatures. No parameters could be extracted after annealing at 400 ºC possibly due to large inhomogeneities developing at these temperatures.

Much further work can be done as far as annealing experiments of bulk and implanted ZnO is concerned. Surface conduction can be verified by surface removal experiments such as argon ion sputtering or chemical etching. This would also allow a better analysis of the impact of annealing on the bulk of the material. Techniques for surface studies such as X-ray photo spectroscopy (XPS) can be used to correlate the presence of surface conduction to the presence of certain chemical species such as OH-ions. The surface conduction may also be due to structural anomalies at the surface, and Rutherford backscattering (RBS) and X-ray diffraction (XRD) may provide new insight here. The electrical properties of the surface and near-surface bulk can of course also be studied by current-voltage and capacitance-voltage measurements on suitable Schottky contacts. Deep level transient spectroscopy (DLTS) on such contacts can yield more information on deep level impurities in the samples. More modern techniques such as second harmonic generation (SHG) from femtosecond laser pulses may be used to study impurities and electric field build-up at the surface. The bulk properties can be studied by complementary techniques such as electron paramagnetic resonance (EPR), Raman spectroscopy and photoluminescence (PL).